Protective coatings based on 2D-materials

Stoot, Adam Carsten; Bøggild, Peter; Camilli, Luca

Publication date:
2016

Document Version
Publisher's PDF, also known as Version of record

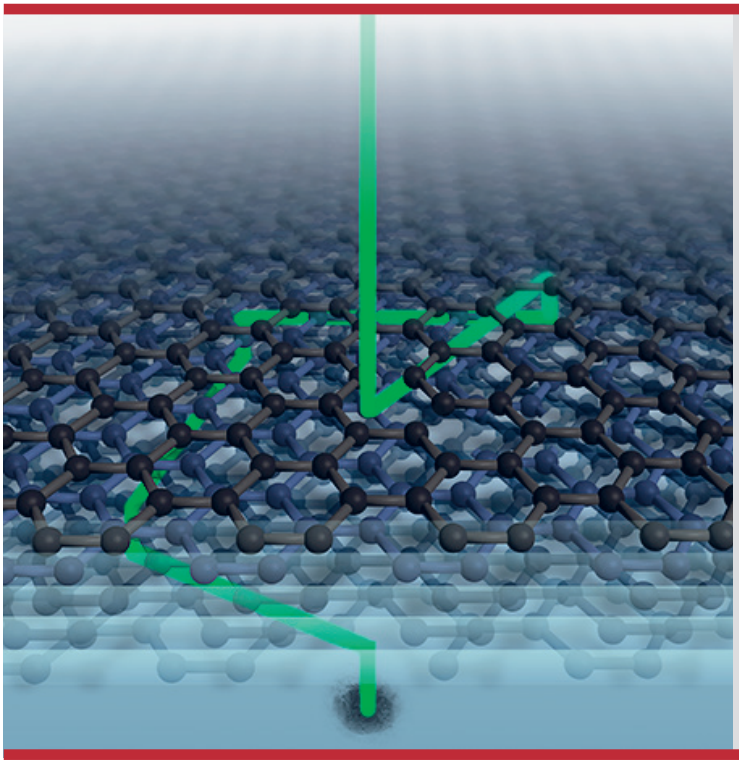

Protective coatings based on 2D-materials

Adam C. Stoot
PhD Thesis October 2016

DTU Nanotech
Department of Micro- and Nanotechnology

DTU Nanotech
Department of Micro- and Nanotechnology

Protective coatings based on 2D-materials

PHD THESIS

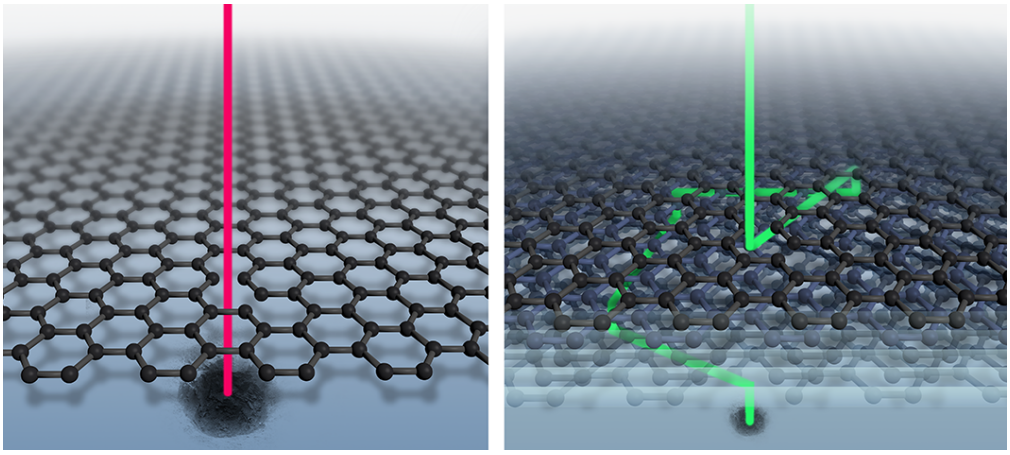

ADAM C. STOOT

DTU NANOTECH
OCTOBER 10th 2016

Summary

Corrosion has a major impact on the world economy. Barrier coatings is one of the most widely applied strategies to reduce the degradation of materials, however, every coating technology has its drawbacks. Graphene has the potential of creating the ideal coating, being atomically thin and, when in perfect condition, impermeable to most molecules. However, it has recently been demonstrated that graphene can promote galvanic corrosion and may actually increase the corrosion rate in the long term.

The aim of this thesis is to individuate, develop and demonstrate solutions based on 2D-materials, that can deliver viable coatings technologies circumventing the drawback demonstrated for graphene coatings. The focus is twofold, with a solution that focuses on multi-layer coatings, wherein the drawback of graphene is circumvented by diffusion limitations. Here it will be shown that such solutions are viable in pH neutral environments, however, a new issue with graphene coatings is encountered in strong acidic environments.

Another focus is on "white graphene", another 2D-material that shares many of its properties with graphene, but without some of the fundamental limitations.

Through the development and investigations of 2D-coatings technologies, testing methods and synthesis four patents applications have been submitted, making a substantial platform for further development of 2D-based barrier coatings.

Dansk resumé

Omkostningerne til korrosionbeskyttelse, og genopbygningen efter samme, har stor indflydelse på verdensøkonomien. Barriere-basserede coatings er en af de mest brugte metoder til at reducere nedbrydningen af materiale, men denne teknologi har også sine ulemper. Grafén har potentialet til at være den perfekte coating ved at være atomart tynd og, når den er i perfekt stand, uigennemtrængeligt. Det er dog fornyligt blevet vist at grafén kan fremme galvanisk korrosion og kan øge korrosionsrate i det lange løb.

Målet med denne afhandling er at udvælge, udvikle og demonstrere coating-teknologier baseret på 2D-materialer, der giver anvendelige løsninger, der kan omgå det netop beskrevne problem. Fokus for afhandlingen er todelt; først behandles multilags-coatings, hvori problemet med grafén kan omgås. Her vil det blive vist at sådanne løsninger er gangbare i pH-neutrale miljøer. Til gengæld opstår der et helt nyt problem i meget sure miljøer.

Fokus vil også blive lagt på "hvid grafén", et andet 2D-material, der har mange af de samme egenskaber som grafén, men ikke de samme begrænsninger.

Gennem udviklingen og undersøgelsen af 2D-coating teknologier, testmetoder og fremstillingsprocessor er der indsendt 4 patentansøgninger, hvilke kan give en stærk base for videreudviklingen af 2D-materiale baserede coatings.

Preface

This PhD-thesis was conducted at DTU Nanotech at the Technical University of Denmark in the NanoCarbon group under the supervision of Dr. Luca Camilli and Professor Peter Bøggild in the period from 2013 to 2016. Besides the laboratories at DTU Nanotech, experiments were conducted at DTU Danchip, DTU CEN, AU iNano and AU institute for physics and astronomy.

Kongens Lyngby, October 10^{th} 2016

_____

Adam Carsten Stoot

Acknowledgments

I would like to acknowledge my supervisors Professor Peter Bøggild and Dr. Luca Camilli as well as the rest of the NanoCarbon group at DTU Nanotech. I would like to thank Dr. David Mackenzie for his help with Raman data treatment and helpful discussions, Miriam Galbiati for her contributions to the oxidation experiments, Associate Professor Tim J. Booth for nice discussions, Patrick R. Whelan for his help with transfer processes, Feng Yu for our close collaboration on electrochemical experiments and long discussions, PhD-student Lene Gammelgaard for her help especially with the AFM, PhD-student Jakob Jørgensen, Dr. Andrew Cassidy, Dr. Richard Balog, PhD-student Line Kyhl and Professor Liv Hornekær for their contributions and lending us equipment for heterostructure experiments and for making me feel welcome in Aarhus. Moreover, I would like to thank Dr. Line Koefoed, PhD-student Emil Bjerglund and Associate Professor Steen Uttrup and Professor Kim Daasbjerg for chemical discussion and making me feel even more welcome in Aarhus. I would like to thank Professor Bo W. Laursen, Associate Professor Kasper Nørgaard, PhD-student Marc Overgaard and PhD-Student Martin Kühnel from the University of Copenhagen for nice discussions. I would also like to thank Susie-Ann Spiegelhauer and Jens Hinke from Accoat A/S for all their help testing all kind of coatings. I would also like to thank Allan Holm from Grundfos A/S and Line Bergmann from Welltec A/S for their help with testing samples. A special thank you to Dr. Ross Birney for our collaboration and the development of electrochemical equipment.

I would like to thank Professor Alda Simões and the rest of her group for letting me visit their facilities and nice discussions in Lisbon, Portugal. I will also thank Sara W. Anker and Christina F. Schouw for keeping the labs safe and pleasant to be in and for helping with the administrative part of building a lab from scratch. I would also like to thank the personnel from DTU CEN for their training and guidance in electron microscopy, and the personnel from DTU Danchip for their help with clean-room equipment. I would also like to say thank you to Nanna Bild for her help with some of the illustrations.

And lastly I would like to especially thank Dr. Luca Camilli for fantastic sparring and guidance through the PhD-jungle both with the experiments and putting the science down on paper.

Contents

List of Publications

1. Article: **A. Stoot**, L. Camilli, S. Spiegelhauer, F. Yu and P. Bøggild. Multilayer Graphene for Long Term Protection of Stainless Steel Bipolar Plates for Polymer Electrolyte Membrane Fuel Cell. *Journal of Power Sources* 846-891, **293**, 2015

2. Article: F. Yu, **A. Stoot**, P. Bøggild and L. Camilli. Failure of Multi-Layer Graphene Coatings in Acidic Media. *RSC Advances* 21497-21502, **6**, 2016

3. Manuscript: L. Camilli, J. Jørgensen, J. Tersoff, **A. Stoot**, R. Balog, A. Cassidy, J. Sadowski, P. Bøggild and L. Hornekær. Self-Assembly of Graphene Quantum Dots in a Two-Dimensional Boron-Carbon-Nitrogen Alloy. *Under consideration, Nature Communications* , 2016

4. Manuscript: M. Galbiati, **A. Stoot**, D. Mackenzie, P. Bøggild, L. Camilli. Observing Oxide Evolution of Copper Protected by Graphene and Boron Nitride Coatings. *Accepted for publication, Scientific Reports*, 2016

5. Manuscript: P. Whelan, B. Jessen, R. Wang, B. Luo, **A. Stoot**, D. Mackenzie, P. Braeuninger-Weimar, A. Jouvray, L. Prager, L. Camilli, S. Hofmann, P. Bøggild and T. Booth. Raman Spectral Indicators of Catalyst Decoupling for Transfer of CVD Grown 2D Materials *Submitted* to Carbon, 2016

6. Patent application: **A. Stoot**, R. Birney and T. Booth. Working Electrode Holder and Electrochemical Cell. *EP15763837* (WO/2016/016214), 2014

7. Patent application: **A. Stoot** and L. Camilli. Chemical Vapour Deposition from a Radiation-Sensitive Precursor. *EP16159305*, 2016

8. Patent application: F. Yu, L. Camilli, P. Bøggild, P. Whelan, T. Booth and **A. Stoot**. Graphene Polymer Hybrid Coatings with a Layered Structure. *EP16176135*, 2016

9. Patent application: **A. Stoot**. Method and Toy Element for Generating a Computer-Readable Representation of a Construction made of Toy Building Elements. *EP16190718*, 2016

Chapter 1

Introduction

This introductory chapter will first give a general but brief introduction to the fields of corrosion science and graphene research, as well as the state of the art of these fields combined. The motivation will here highlight the prospects of evolving these fields further. Lastly an outline will be given, completing this chapters function of outlining the thesis.

1.1 Motivation

In a world with a limited supply of resources, and where corrosion and its mitigation account for 3-4% of the GDP of industrialized countries[1, 2], and 4.2 % or 180 billion dollars in the USA alone[3], any reduction of these processes will have a significant impact on both the environment and the world economy. The term corrosion, stemming from the Latin, corrosio - eating away, is a general term for the process of degradation of a material by chemical processes. In its common use, corrosion covers both oxidation of metals, microbial corrosion, galvanic corrosion, metal dusting and pure chemical degradation.

Today different strategies for protecting surfaces are being utilized, including alloying with metals less susceptible for corrosion, sacrificial anodes as well as coatings. While alloying will change the mechanical properties of the substrate, and sacrificial anodes requires a large bulk of disposable metal (that needs to be replenished), surface coatings can be applied without significantly changing the mechanical properties of the coated material. However, classical surface coatings does add to the thickness of the substrate, potentially ruining the tolerances of the item coated. Moreover, the interface between the coating and the substrate needs a strong adhesion, as there is otherwise a risk of delamination[4].

Ultimately, three core strategies exist, each with their own advantages and disadvantages

1. Alloying, forming a stronger and more corrosion resistant material or a self-passivating material. Here mechanical properties will change, but corrosion can be slowed in certain environments.

2. Anodic protection, creating a galvanic system, in which the substrate is the noble part, and will act as a cathode and therefore not corrode. However, it will accelerate the corrosion of the sacrificial metal anode, which will require space and have to be replaced periodically.

3. Protective surface coating. Here the mechanical properties are maintained, however, a surface layer may not only affect physical dimensions, it would also change properties such as heat conductivity. Also, a weakness exist in the interface, where strong adhesion can be hard to achieve, and a risk of delamination exist. Wear and tear may also break down or penetrate a surface coating.

In this thesis, the third strategy will be explored. We will start by imagining the perfect coating: A material so thin that it does not change the geometry of the coated object, thus not compromising any mechanical tolerances. A material that acts as a perfect barrier, allowing no species to come in contact with the object to be protected. A material that is flexible and can conform to the substrate. A material that adheres well. A material that is chemically stable, and does not dissolve, oxidise or otherwise change in strong acidic or alkaline media. The material should also be stable in saline environments, as this is one of the major sources of corrosion both in the maritime industry and in general[5]. A material that does not contain heavy metals and generally is environmentally friendly. And lastly, a durable coating that can withstand abrasion from sand, rocks, metal splinters etc.. In most applications it should be inexpensive as well.

To the knowledge of the author no coating existing today comes close to fulfilling al of the requirements listed above, and an universal "perfect coating" does not exist. One can only choose a coating that fulfil some of these properties most central to the application at hand.

Starting with the first property listed; a super thin coating, one possible candidate has been proposed in graphene[6–9]. The recently discovered, atomically thin material consisting of sp^2-hybridised carbon[10, 11]. Moreover, Scott Bunch et al. demonstrated that even a single atomic layer of perfect graphene is impermeable to all molecules, even hydrogen[12] potentially fulfilling the second property listed. Graphene may be flexible as well[13] and thermally, graphene is stable up to 500 °C in air on a silicon dioxide substrate[14]. Consisting

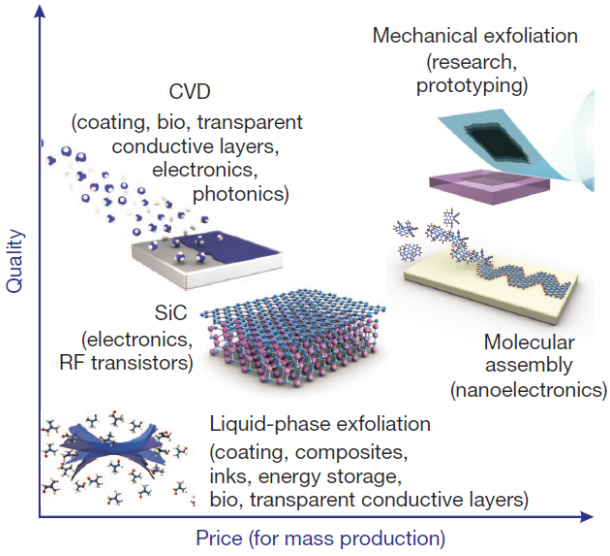

(a)

Figure 1.1: (a) Graphene synthesis methods. The cost/price axis can be translated to a viability scale for corrosion protection barrier coatings. *Reprint from [19]*

only of carbon, graphene is inherently free of heavy metals.

However, graphene coatings are still in an early phase of development, and it has only been tested in stringent laboratory-based tests. Moreover, Schriver and co-workers[15] found that graphene, being derived from the very noble carbon/graphite, can actually enhance corrosion by forming an galvanic cell as the cathode. Hsieh et al. showed that it was possible to selectively block defects in single or few-layer graphene coating using atomic layer deposition (ALD), hugely decreasing the corrosion rate[16]. This method only demonstrates the potential of a perfect graphene coating, however, the coating produced is not stronger than the blocking material deposited and this increases the coating thickness. It is therefore not deemed a viable route as an industrial coating.

An obvious first question is: Can this galvanic corrosion enhancing phenomenon be circumvented in a practical way? Secondly, how does graphene fare in tests more applicable to the industry, both in saline and other even harsher environments? Does an alternative to graphene exist which does not have this inherent weakness?

Graphene can be produced in several ways, as illustrated in figure 1.1. Cost can be translated into a viability scale, and thus mechanical exfoliation is easily ruled out. In this work, chemical vapour deposition is chosen as the main fabrication method, as this synthesis method produces high quality graphene [17], that can be fabricated in meter scale [18].

1.2 Outline

This thesis will, after this introduction to corrosion, corrosion prevention strategies and graphene go through the theoretical background, going in depth with the properties that potentially makes graphene - and other 2D materials - uniquely suited to fill a gap in the coating and corrosion prevention sector. Here basic electronic properties of graphene that are necessary to understand its mechanical behaviour will be treated. Properties such as impermeability, stability and mechanical bond strength will be described.

In chapter 3 the primary or repeatedly used methods from this thesis will be described. The chapter can be used as a list giving a basic explanation of equipment for synthesis, characterisation and testing equipment. Here equipment used in a standard way will be shortly described, generally in the context of corrosion or graphene, while some instruments used in non-standard way for analysis of 2D-materials will be described in more detail. Some details will also be given on the Quick Working electrode, a piece of electrochemical equipment invented in this project.

In chapter 4 the synthesis of coatings will be described such as single layer graphene, multi layers graphene and hexagonal boron nitride. This chapter will include recipes that can be used as a basis for replicating the coatings described in this work.

In chapter 5 single layers coatings will be described. Here single layers graphene and single layer hexagonal boron nitride are compared as oxidation barriers for protecting copper surfaces. The evolution of oxygen was monitored in real time during the experiments at elevated temperature in air. The fundamental differences between these 2D materials have a great impact on their performance.

In chapter 6 multi-layer coatings will be treated. Here nickel is used as a seed layer for synthesis of graphene for protecting stainless steel in simulated seawater. Electrochemical tests are made, highlighting the influence of the seed layer, and long term test of the coating in heated seawater completed the picture of how multiple graphene layers can overcome one of the fundamental problems that can arise from graphene-based coatings. Another set of experiments were conducted in strong acids. Here the impact of the seed-layer or catalyst is once again emphasized, as aqueous protons can interact with this and compromise the otherwise effective barrier coating.

In chapter 7 an overview of the problems highlighted and solved throughout this work will be given. The properties of graphene and hexagonal boron nitride will be discussed and their potential impact accentuated.

Chapter 2

Theoretical background

This chapter will highlight the fundamental properties of primarily graphene, but also discus some properties of hexagonal boron nitride, as an alternative to graphene for coating purposes. First carbon allotropes will be treated, and fundamental properties of graphene mentioned as a consequence of the hybridisation. Hereafter advantages and disadvantages inherent in using a two dimensional material as a corrosion or oxidation barrier will be treated. Reading this chapter will give the reader the conceptual framework used throughout the thesis.

2.1 Carbon and Hybridisation

In the ground state, carbon has two electrons in the 2s-orbitals, and two valence electrons occupying two of the three 2p-orbitals. The energy states for s- and p-electron orbitals in carbon are very close to each other, making hybridisation possible. If all three p-orbitals are hybridised, the sp^3 orbitals will give rise to four chemical bonds and create an insulation material such as diamond. However, in the case of sp^2-hybridisation, three chemical bonds with a 120 degree angle between them will be preferred. This planar structure, in addition to the electrons used in the chemical bonds, has an extra p-electron available. This gives rise to weaker π-bond, where the electron both contribute to the covalent bonds, but are still free to move making the material conducting. Graphene and graphite is sp^2-hybridised. Lastly, an sp-hybridisation is possible, where only one p-orbital is hybridized with an s-orbital. This is seen in the hydrocarbon class of alkynes such as acetylene.

Graphene, being sp^2-hybridised, has 3 strong σ-bond from the hybridised orbitals forming a honeycomb lattice. The last 2p-orbital electron is much looser bond, making it mobile and

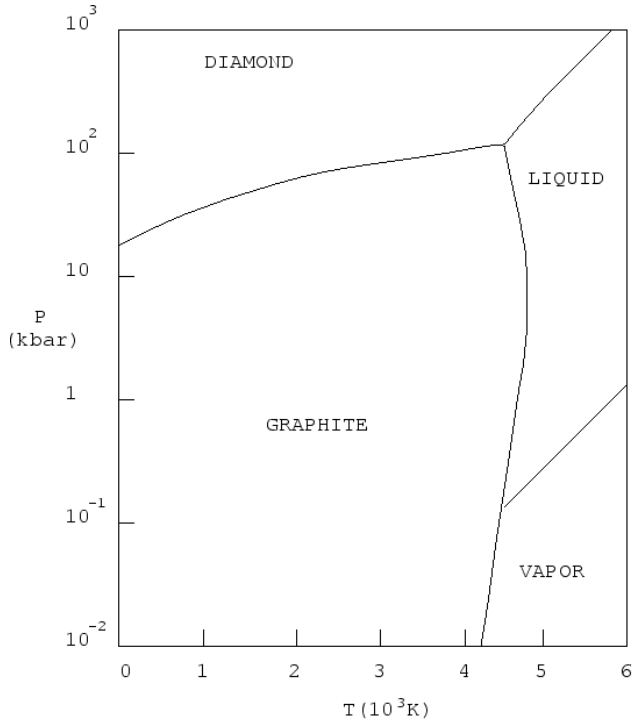

(a)

Figure 2.1: (a) Carbon phase diagram. Graphite, with its sp^2-hybridised carbon, can be seen to be the most stable allotrope of carbon up to high pressure (> 10 kbar) and high temperature (4000 °C). *Simplified version originally from [22]*

gives sp^2-hybridised carbon electronic properties in contrast to the insulating sp^3 carbon allotrope.

Observing the phase-diagram for carbon, it becomes clear that the sp^2-hybridised graphite is the most stable form of carbon, not only at ambient pressure and room-temperature, but in the full range of temperatures and pressures found in most application from deep-sea (down to more than 10000 m) and at temperatures up to approxiamtely 4000 °C as seen on figure 2.1a. Theoretical calculation even suggest that graphene is more stable than graphite, and can withstand temperatures up to 4237 °C[20]. However, in ambient atmosphere, the carbon can react with constituents form the air, and single layer graphene have been reported to oxidise at temperatures down to 250 °C[21].

Graphene chemistry can be compared to that of graphite, with high chemical stability, but with the ability to adsorb and desorb various atoms and molecules such as NO_2, NH_3, K and OH, which can act as electron donors or acceptors and affect its electronic properties[23]. However, in contrast to graphite, graphene is all surface and no bulk, so even moderate surface modifications may in some cases affect its properties. Moreover, where graphite is

flat, graphene can exhibit nanoscale curving in turn giving local strain and compression, again influencing local reactivity.

Even though graphene is very stable, it can be made to react with e.g. hydrogen. Elias et al. [24] used plasma to hydrogenate graphene, creating graphane. By change the carbon to a sp^3-hybridised structure, no carbon bonds are broken and the graphene structure is maintained. Graphane is electronically very different from graphene being an insulator.

Graphene can also react with oxygen creating graphene oxide (GO). As the purely chemical oxidation of graphene to GO is not easily done, graphene oxide is classically produced in a mixture of sulphuric acid, sodium nitrate and potassium permanganate[25]. This is, like graphane, no longer a true 2D-material, however, imagining a coating undergoing this transformation it would, in itself, not be destroyed, with the maintained hexagonal structure. However, further oxidation can take place, where carbon atoms are substituted with oxygen atoms. From DFT-calculations it has been seen, that such groups can align and form epoxy groups. These can then in turn be transformed to carbonyl pairs resulting in a hole in the graphene film[26].

2.2 Hexagonal Boron Nitride

With the same honeycomb structure, consisting alternately of boron and nitrogen atoms, such that only nitrogen-boron bonds exist, with almost the same bond length ($a_{cc} = 1.42$ Å, a_{bn}~1.45 Å[27]), hexagonal boron nitride (hBN) is an insulating counterpart to graphene. The similar bond length and structure opens up the possibility of in-plane hetero structure with only limited strain in the crystal lattice. With a band gap of $\sim$ 6 eV, hBN is also referred to as "white graphene". Li et al. investigated the stability of hBN in air, and found it much less reactive with oxygen than graphene. Like graphene, the reactivity depended on the number of atomic layers, with a single layer being most reactive. According to their study, single layer hBN starts to oxidise at 700°C, and can sustain up to 850°C, while multi-layer structures can tolerate slightly higher temperatures[28]. Thermogravimetric studies have suggested that thick hBN nano platelets are stable up to 1000°C in air[29]. In acidic media, hBN is very stable, however, a strong alkaline solution may exfoliate the layers[30]. Another important aspect is, that, like graphene, hBN has a negative thermal expansion coefficient, and will therefore act in a contrary way to metals.

2.3 Impermeable Honeycomb Lattice

The permeability of the honeycomb lattice was tested by Scott Bunch et al. in a range of experiments[12]. In one of these, flakes of single layer graphene were placed on cavities etched into a silicon wafer. By changing the surrounding pressure, the graphene membranes acted as balloons due to the pressure difference. By observing the deflation of these balloons it was concluded that the only leak of the nitrogen gas inside the balloons were through the underlying silicon dioxide substrate. On figure 2.2a the gas escape rates of three different gases are shown. No difference could be seen between using a single atomic layer of graphene and the maximum tested, 75 atomic layers. These results can be supplemented by density functional theorem (DFT) that predicts a potential barrier of 35 eV for O_2 to pass through the hexagonal ring in graphene[31]. For passing through hexagonal boron nitride in the same manner the number is slightly lower at 30 eV. A single missing atom defect lowers the potentials substantially. Also, in the case of hBN, the potential barrier for oxygen depends on the atom missing, due to the different electronic configurations of the elements; a missing B-atom results in a barrier of 11 eV, while a missing N-atom only results in a barrier of 3 eV. This should be put into perspective, as the thermal energy at room temperature is approximately 26 meV. Shen and coworkers did also do a simulation of an 8-atom defect. Here the barrier is lowered to 0.1 eV, which can no longer be considered a effective barrier, and will still give a rate constant of approximately 2% according to the Arrhenius equation $k = Ae^{-Ea/(RT)}$[31].

2.4 Mechanical Properties and Adhesion

The Morse potential can be used to approximate the carbon-carbon bonds (of length $a_{cc} = 1.42$ Å) as springs, and, along with geometry considerations, as a mean to estimate the Young Modulus of graphene. The Morse potential is given by

$$U_M(r) = D_e \left(\left[1 - e^{-\beta(r-r_e)} \right]^2 - 1 \right)$$

Belytscko et al. made atomistic simulations of carbon in carbon nanotubes, which is a close aproximation of graphene. They found the constants $D_e = 6.03105 \cdot 10^{-19}$ Nm and $\beta = 2.625 \cdot 10^{10}$ m^{-1}[32]. The Morse potential is plotted on figure 2.2b for $r_e = a_{cc}$.

Taking the Morse potential around the minimum energy, the potential can be considered parabolic and can be described as $U(r) = \frac{k(r-r_e)^2}{2}$ for $r \approx r_e$. The spring constant can be

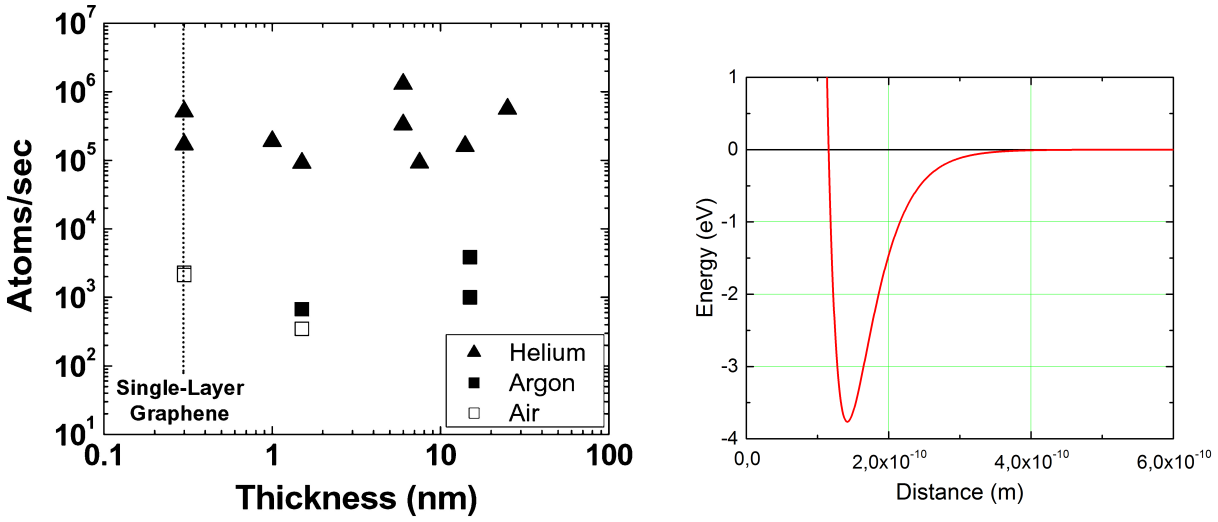

(a) (b)

Figure 2.2: (a) Graph of gas escape velocity as a function of graphene film thickness. It is apparant that no significant difference is seen between one atomic layer of graphene and 75 layers. *From [12].* (b) Morse potential approximating the carbon-carbon bond.

found by taking the second derivative

$$k = \left(\frac{d^2U(r)}{dr^2}\right)_{r=r_e}$$

which described the spring constant of a single bond. However, due to the honeycomb lattice, with the 120° angle between the σ bonds, the effective spring constant is

$$k_{eff} = \left(\frac{1}{k} + \frac{1}{2k\sin 30°}\right)^{-1} = \frac{1}{2}k$$

Young modulus can then be written as

$$E \equiv \frac{\sigma}{\epsilon} = \frac{F/A_0}{\Delta r/r_0} = \frac{nk_{eff}\Delta r}{A_0(\Delta r/r_e)} = \frac{nkr_e}{2A_0} \tag{2.1}$$

where n is the number of bonds per cross-sectional area A_0. A true 2D object does not have a cross-sectional area, but as the electron cloud spreads out perpendicular to the graphene-plane, graphene can in this case be considered quasi-3D. This distance can be set to the spacing between two layers of graphite $d = 3.35$ Å[33]. The bond length should, however, be taken as two opposite sides of the hexagon to account for the effective spring constant $\sqrt{3a_{cc}} = 2.46$ Å. Inserting these values in equation 2.1 results in a Young's modulus

of $E = 1.44$ TPa. However, it should be noted that uniaxial strain of graphene will result in a contraction in the perpendicular direction. Think of pulling a chicken fence - even though the metal does not bulge, it can still be elongated, but will be contracted in the perpendicular direction. This is also the case for graphene, and a real Young's modulus is therefore expected to be smaller than the calculated approximation.

In comparison Lee et al.[34] measured young modulus of a suspended single layer graphene over a round hole with an AFM-tip to be 1.0 ± 0.1 TPa. However, due to the very thin nature of single layer graphene, this exceptionally high Young's modulus, will still result in a flexible film. The failure strain is large for graphene as well, reported to be around 12%[34].

Graphene might have very strong bonds in-plane, however, out of plane only van-der-Waals (vdW) forces remains to attach a perfect graphene film to a surface. Due to the flexibility of graphene it can conform to surfaces, resulting in a much larger contact area for the vdW forces to work on. Even soft macroscopic surfaces has a relative small contact area on the macroscopic scale, let alone even smaller on the micro- or nanoscopic scale[35]. Graphene, on the other hand, has a much larger contact area, that, combined with the low weight of a single atomic layer, results in an unusually strong adhesion from vdW-forces.

2.5 Corrosion, Oxidation and Steel

Corrosion is categorised into a number of different mechanisms. In this section, mechanisms central to the experiments and for graphene related systems in general will be described.

Firstly, uniform corrosion is a homogeneous attack and degradation of a surface affected by a corrosive media or driven by the part having attained the role of anode in an electrochemical system. Uniform corrosion may lead to degradation of large metal part, but it is easily detectable, so it seldomly lead to catastrophic failures.

A very common form of corrosion, and especially important for graphene or graphite related systems, is galvanic corrosion. When dissimilar metals are electrically connected, most of a corrosion cell is established, as the most noble will attain the role of cathode, while the less noble will be the anode. If the two electrically connected metals are also in contact with an electrolyte, a complete corrosion cell is made, where electrons can be supplied from the anode to the cathode, where they can combine with anions from the electrolyte, which are then precipitated and deposited. Similarly, the lack of electrons will make the anode dissolve. The galvanic series can be seen on figure 2.3a. Here it is clear that graphite, and therefore graphene, has a higher potential than almost any metal in the series, and therefore

will form a galvanic cell being put in contact with any of these metals.

A corrosion cell can also arise locally, even on a single element, for instance initiated by geometry. In crevice corrosion a local diffusion controlled depletion of oxygen results in a locally more acidic environment which in turn induces a corrosion process. As metals are conducting the cell now exist between the crevice and bulk surface, where the crevice acts as anode and the bulk surface as cathode. Metal ions released from the anodic reaction can hydrolyse, further decreasing the pH and sustain the extra corrosive micro-environment in the crevice. An illustration of the process in seawater can be seen on figure 2.3b. In this case an iron-alloy, such as steel, is oxidised in the crevice $Fe \longrightarrow Fe^{2+} + 2\,e^-$, which according to the Pourbaix-diagram initiates already at a pH below 7[36]. The electrons are used for splitting water outside the pit $O_2 + 2\,H_2O + 4\,e^- \longrightarrow 4\,OH^-$. The pit is now positively charged drawing in negative ions such as chloride, which in turn can react with the iron and give rise to the reactions, $FeCl_2 + 2\,H_2O \longrightarrow Fe(OH)_2 + 2\,HCl$ and $FeCl_2 + 3\,H_2O \longrightarrow Fe(OH)_3 + 3\,HCl$[37], building up rust concealing and isolating the pit while at the same time increasing the acidity of the pit further, accelerating the corrosion.

While some metals, like copper, have a porous oxide layer, others have much denser oxides. By forming these denser oxides, some metals can protect themselves. The metal oxide may both have a different chemical potential, making corrosion or further oxidation harder, and may block passage to the un-oxidised metal surface underneath. Observing the corrosion rate of a metal that forms a protective oxide, an initial higher rate will be followed by a reduction when the passivating oxide is formed. However, if the environment is sufficiently harsh, or a potential is applied, the oxide will eventually break down, and the sample will corrode quickly. Further information will be given in section 3.7.2.

Another important aspect is not to damage the substrate while applying a coating. Paints and coatings that can be sprayed, spin-coated or painted onto a surface are often applied at room temperature, however, many of the coatings that will be described in this thesis are synthesised directly on the substrate surface at high temperatures. When e.g. stainless steel is prepared for a product, it undergoes a certain heat treatment and subsequent controlled cooling rate, making sure that e.g. the carbon contents is according to specifications. Heating a substrate above, and especially keeping it above a certain temperature, can start sensitization. In this process e.g. chromium migrates towards the grain boundaries, de-alloying stinaless steel. So, besides the changes to the mechanical properties, the de-alloying will result in local cathodes/anodes of different compositions[39]. The areas around the grain boundaries will experience accelerated corrosion in electrical and ionic contact to the more cathodic migrated species. This is especially the case as these areas have a lower chromium-

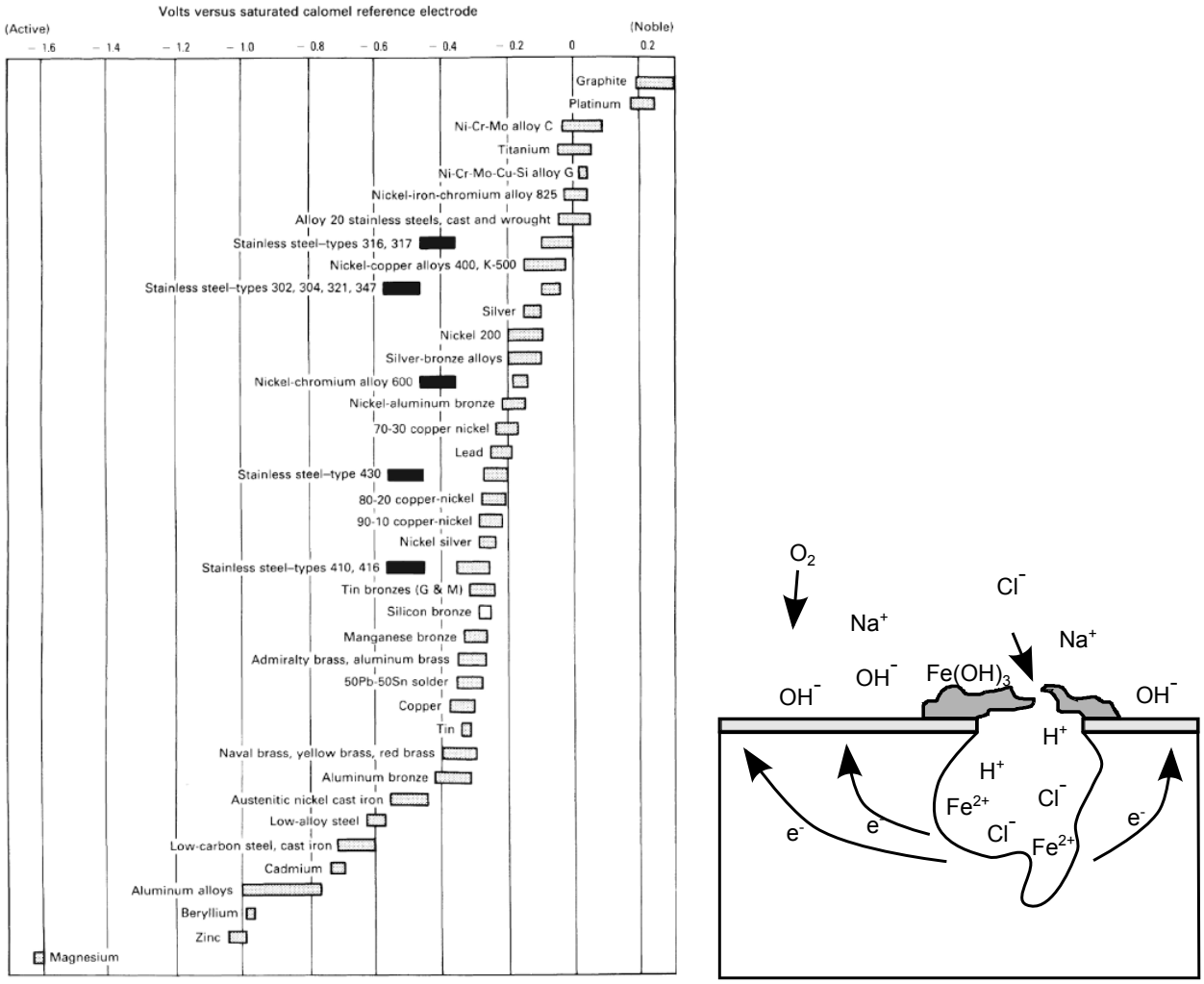

(a) (b)

Figure 2.3: (a) Galvanic series in seawater. Graphite can be seen to be the most noble entity, and will therefore act as the cathode in contact with any other element on the list. The stainless steels have two areas - the filled, which are their natural potentials, and the grey areas which are their potential with their native passivating oxides formed. *From* [38]. (b) Illustration of crevice or pitting corrosion of steel. The inside of the pit will act as an anode reducing iron. The electron are transported through the metal to the surface the acts a cathode, reacting with water and oxygen creating hydroxide-ions. The pit will now be positively charged which will draw in negative ions such as chloride. These can react with the iron-ions forming a salt further isolating the pit and as a by-product produce hydrochloric acid, further enhancing the corrosion in the pit.

contents, thus are less prone to forming a passivating oxide as is clear from figure 2.3a. This phenomenon is called inter-granular corrosion.

Chapter 3

Methods

In this chapter I will describe the equipment used for synthesis and characterisation of 2D materials, both single and multi-layered. Although a range of fabrication methods are possible for producing graphene and other 2D-materials, this thesis limits itself to synthesis using chemical vapour deposition (CVD). This chapter will also briefly describe the testing methods used to characterise the synthesised graphene and hBN coatings. It will describe the techniques such as scanning electron microscopy (SEM), transmission electron microscopy (TEM), Raman sectroscopy, X-ray photoemission spectroscopy (XPS) and a range of electrochemical characterisation techniques that have been used during this project. *All synthesis and characterization methods have been adjusted and used by me. I performed the ultra-high-vacuum synthesis together with Dr. Camilli from DTU Nanotech and Jakob Jørgensen et al. from the Surface Dynamics Group at the University of Aarhus.*

3.1 Synthesis Equipment

Throughout the project several fabrication systems were used; a home-built CVD-system, a commercial rapid-thermal CVD-system (RT-CVD), a commercial system with the possibility of plasma enhance CVD (PE-CVD) and a customised commercial tube-furnace. Moreover ultra high vacuum equipment was used for heterostructure growth. Here they will be shortly described with their most pronounced properties.

3.1.1 Home-built CVD-system

Early tests for multilayer-graphene synthesis were conducted in a system based on halogen bulbs heating a graphite block inside a low-vacuum environment. The system was able to

supply hydrogen, nitrogen and acetylene to the sample during processes and could maintain temperatures around 850°C. A LabJack controller was used with LabView to control the four mass-flow controllers. The pulse width modulated output from an Arduino microcontroller was used in connection with a high-power MOSFET for controlling the power to the two halogen light bulbs with feed-back from a thermocouple inserted directly into the graphite block. A variable valve was installed between the chamber and the rough oil pump. The chamber lid consisted of a 1 cm thick glass disc, making it possible to observe the sample during synthesis processes.

3.1.2 AS-ONE - Commercial CVD-system

Throughout most of the project a system produced by AnnealSys (Montpellier, France) was used for graphene synthesis. The AS-ONE is a Rapid Thermal CVD (RT-CVD) system capable of reaching 1500°C at ramp rates up to $200\frac{^{\circ}C}{s}$ by using high-power infra-red light passing through a quartz-window to radiate the sample, and thus minimizing the thermal inertia compared with a resistively heated system. We have constructed a gas system able to supply hydrogen, argon, acetylene, methane, bubbled borazine and nitrogen to the CVD-system. The reaction chamber is a cold-wall type and has a volume of approximately 1L, only leaving space for small samples such as films, foils and wafers. The chamber can be seen on figure 3.1a. A susceptor able to accommodate a 4 inch wafer was bought with the system, but using a computerised numerical control (CNC) tool, I milled out a slightly larger box made of graphite able to hold samples up to Ø80 mm and a height of 7 mm.

Three exhaust options can be used on the system: Either ambient pressure automatically open a valve directly connected to the ventilation system, a turbo-molecular pump can be used to obtain a high vacuum (10^{-6} mbar range - however, no process gasses can be used while the turbo-molecular pump is utilized) or a capacitive pressure gauge can control a variable valve to the rotary pump. Here the pressure can be controlled in a range from approximately 10^{-3} mbar up to 133 mbar limited by the gas flow rates and the range of the pressure gauge. The pumping system can be seen on figure 3.1b.

Due to the high temperatures used, copper occasionally evaporated and is subsequently deposited on the cold walls and the quartz window in the system. I designed a kit for cleaning the system using 10% nitric acid, effectively removing deposited copper from the stainless steel and quartz, however, parts of the chamber are not as easily accessible and possible cross-contaminating is therefore an important factor to assess before using the system.

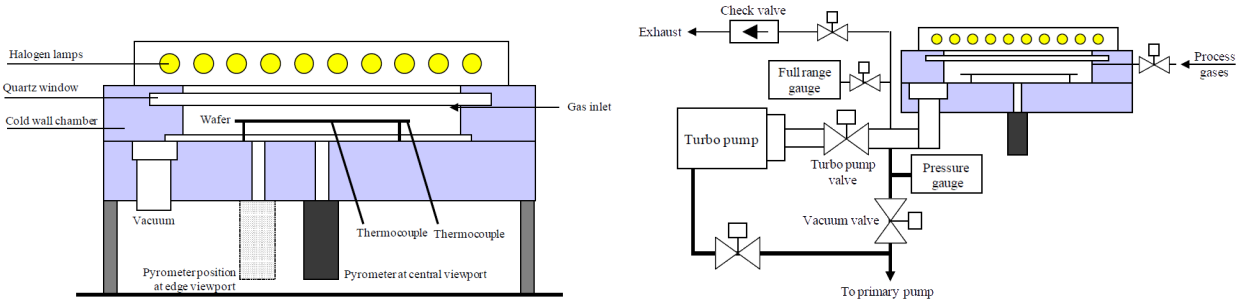

(a) (b)

Figure 3.1: (a) Schematic illustration of the synthesis chamber, halogen lamp placements and temperature readouts of the commercial Annealsys AS-ONE system. The very limited space of the round 1 L chamber can be seen. The backplate and sidewall are directly water-cooled as is the sides of the quartz window. A sample or sample susceptor cannot get to close to the quartz window, as this would cause a heatup, and possibly break the quartz windows due to too large temperature gradients. (b) Overview of the pressure control system of the AS-ONE RT-CVD system. Process gasses can be used either at ambient pressure using the check valve or using the rotary pump. The pressure in the chamber can be controlled using a variable valve in the range from 10^{-3}mbar to 133 mbar. The maximum limit is determined by the range of the pressure gauge giving direct feedback to the valve controller. The turbo pump can only be used for vacuum annealing. *Courtesy of Annealsys*

3.1.3 Tube Furnace

To have a more versatile system, a commercial tube furnace was bought (produced by MTI corporation, Richmond, USA), with interchangeable tubes for each kind of process, thus reducing considerably possible cross-contamination issues. The tube furnace ramps the temperature with a maximum rate of 10°C/min and the gas-injection system consists of a 0254 Brooks Mass Flow Controllers (MFC) control box controlling 3 Brooks MFC's for methane/acetylene, bubbled borazine and hydrogen. The 4th channel is based on a card-edge MFC controlled via a custom made cable and power supply, and supplies high flow of argon.

A quartz boat, for holding the samples, is inserted between two ceramic blocks in the quartz tube. Resistive heating coils installed in insulating ceramic material heats up the central part of the 45 cm long tube. Gas flows from one end of the tube to the other through the chink between the quartz and the ceramic blocks. In one end of the tube a pressure gauge is installed along with the inlet from the gas systems, while the other has a variable valve to the oil pump. Moreover, a pressure safety valve is installed, which opens directly to the exhaust system if the pressure inside the tube exceeds atmospheric pressure.

3.1.4 UHV-synthesis

Some synthesis, in particular the graphene/hBN hetero-structures, were conducted in ultra-high-vacuum systems located at the University of Aarhus. Here the synthesis gases were dosed using leak-valves into the 10^{-8}mbar environment, and the sample was heated using a hot-filament and had a thermocouple or pyrometer readout. This was used both in a Scanning Tunnel Microscope (STM) chamber and in the MATLINE-beamline on the ASTRID2 synchrotron facility.

3.2 Optical Microscopy

Simple optical microscopy can be used to assess the damage to a surface after a corrosion test or to locate graphene flakes on a surface. However, single layer graphene absorbs 2.3% of white light, making it difficult to detect. This can be remedied by using the calculations done by Blake et al.[40] and thus use a suitable thickness of silicon dioxide underneath the graphene layer, that will improve the contrast of single layer graphene to 10-15%. The contrast enhancement can be seen on figure 3.2a.

The large angle light used in darkfield microscopy will also enhance edge contrasts, as only these will reflect light into the optics of the microscope, as demonstrated by Kong et al.[41].

3.3 Raman Spectroscopy

In Raman spectroscopy monochromatic light is used to excite molecules into vibrational or rotational energy states. The energy of a photon is $E_{photon} = hc\frac{1}{\lambda}$, where h is Planck's constant, c is the speed of light and λ is the wavelength. An absorbed or emitted quantum of light, a photon, has the energy $\Delta E_m = E_{photon} = hc\frac{1}{\lambda}$ which can be rewritten into $\tilde{v} = \frac{\Delta E_m}{hc}$, where $\tilde{v} = \frac{1}{\lambda}$ and is the wavenumber. Monochromatic light interacts with the molecules, is absorbed and excites these to virtual energy states. As these virtual states are not stable, they will rapidly decay and re-emit a photon, which is either directly re-emitted (Rayleigh-scattering) returning to the original energy state, down-shifted in energy (Stokes Raman scattering), thus returning to an allowed energy state higher that the original energy state of the molecule, and re-emitting a photon shifted in energy the difference between the original energy state and the new higher energy state. Lastly, the re-emitted photon can also be up-shifted in energy (Anti-Stokes Raman Scattering), where the original energy state is not

the lowest possible, and the newer state has a lower energy as seen illustrated on figure 3.2b. By filtering out the wavelength of the monochromatic light source, only the energy up- and/or down-shifted photon remain. The shift in energy compared with the incident phonon provides a signature of the chemical bonds of the molecules as close to the samples surface as the monochromatic light can penetrate. The virtual energy states can decay into energy states that are vibrations or rotations of the molecules (phonon modes). Therefore, bond lengths and strength, nucleus masses and geometry are all ingredients that allows Raman spectroscopy to provide a fingerprint of the molecules involved. Moreover, molecules subjected to stress, strain or doping, changes some of the parameter previously mentions, which will result in peaks shifting, providing another lever of information from the obtained Raman spectra. However, interpretation of Raman spectra may be difficult, as the amount of factors that can affect the spectra is so large.

A Raman microscope integrates the laser sources in an optical microscope, making it possible to use the optical viewfinder to locate and expose a sub micro-meter sized spot on the sample. Moreover, using the technique with a motorized stage, it is possible to scan the sample surface and thus map local variations in a sample. More specifically, a DXR Thermo Scientific con-focal Raman microscope with a 455 nm laser was used throughout this project.

Raman spectroscopy is one of the most useful tools for detecting graphene, as the different vibrational modes of the sp^2-hybridized carbon not only reveal its presence, but also indicates, among other things, stress and density of defects[42]. Three characteristic resonances are present when studying graphene: The carbon G-peak at 1582 cm^{-1}, which is also present in other allotropes of carbon[43] and excites the E_{2g}-phonon mode which is narrow in graphene; the D-peak at 1350 cm^{-1}, which represents the defect density of the graphene lattice that can initiate a breathing mode of the lattice[44]; and lastly the 2D-peak at 2700 cm^{-1} indicating the long range order of an unperturbed graphene lattice [45, 46]. A Raman spectrum of multi-layer graphene obtained directly on a nickel surface can be seen on figure 3.3a.

The signal strength is related to the absorbance in the material irradiated by the laser source. As single layer graphene is highly transparent in the visual range, the amount of photon interacting will be similarly low and likewise the signal. Placing a graphene sample on silicon dioxide with a suitable thickness compared to the colour of the laser used enhanced the contrast of a single layer graphene greatly as seen on figure 3.2a.

Another important aspect when investigating graphene directly on a metal substrate is the contributions from the substrate itself. Here the choice of laser colour is also important. On copper, higher photon wavelengths results in photoluminescence from the copper background, while lower wavelength avoids this problem[47]. For this reason a 455 nm laser was chosen

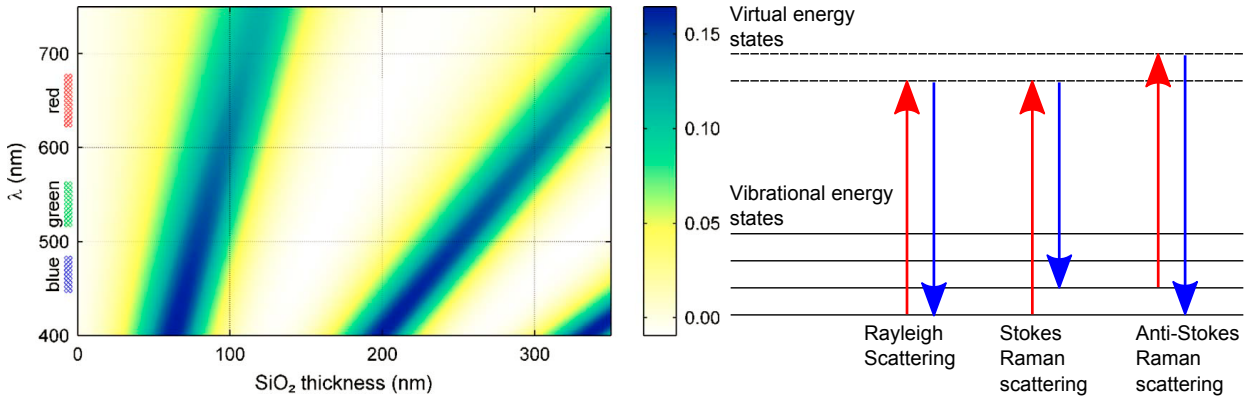

(a) (b)

Figure 3.2: a) Calculation of single layer graphene absorption as a function of wavelength. *Reprint from [40].* b) Energy levels and scattering mechanisms in Raman spectroscopy.

for all Raman experiments instead of the more common 532 nm or 633 nm lasers. It should be noted that the use of a higher laser excitation energy blue-shifts the 2D-peak of graphene compared with the more common green laser[46].

Due to a strong electronic coupling, graphene on a metal such as copper, has a very limited Raman contrast. A de-coupling can be made by oxidizing the copper, creating a cupric oxide layer in the interface, enhancing the contrast by more than an order of magnitude[48]. Multi-layered graphene structures does not have this problem, as consecutive layers will be less affected by the metal substrate. However, with the chosen laser wavelength, contributions from the substrate surface must be expected from samples much thicker single layer graphene. The penetration depth of a 514 nm argon laser in graphite was estimated to be approximately 100 nm, and must be expected to be slightly shorter for the 455 nm excitation laser[49].

Inserting the refractive index found for graphene by Wang et al.[50], the penetration depth can be estimated by $\delta_p = \frac{\lambda_0}{2\pi\Im(\underline{n}_1(\lambda))\sqrt{\sin^2\theta - \Im(\underline{n}_{12}^2(\lambda))}}$[51]; where λ_0 is the incident wavelength, θ is the incident angle of photons and $\underline{n}_1$ is the refractive index of media 1 (air), $\underline{n}_2$ is the refractive index of media 2 (graphite) and $\underline{n}_{12} = \frac{\underline{n}_2}{\underline{n}_1}$. From a normal angle of incident this reduces to $\delta_p = \frac{\lambda_0}{2\pi\Im(\underline{n}(\lambda))}$. In this case a penetration depth of approximately 27 nm for an attenuation of $1/e$ for the exponentially decaying signal is predicted.

Irradiating boron nitride only only gives rise to a single Raman peak at 1366 cm^{-1} (using a 514.5 nm laser), similar to the mode that gives rise to the G-peak for graphene[52]. Besides having only a single peak signature, its intensity is also approximately 50 times lower than that seen for graphene on silicon dioxide. The peaks intensity is proportional to the number of layers for the first several layers[52], however, as the Raman signal intensity is highly

dependent on e.g. focus, laser power and the surface it is detected on, the signal intensity can in best case be used compare flakes next to each other on the same substrate. Often, both due to the weak signal, due to the limited amount of information that can be obtained from the single peak and as it cannot be distinguished from the graphene/graphite D-peak (should both materials be present) other techniques such as X-ray Photoemission spectroscopy (which is discussed later) are utilized instead for hBN samples.

In this work, Raman spectra have been obtained mostly directly on metal surfaces where the optical contrast of graphene is much lower . Moreover, in oxidation experiments, oxidation of a metal surface decouples the graphene vibration modes as well as increases the optical contrast, both contributing to a stronger Raman signal[48].

3.4 Scanning Electron Microscopy

Using electromagnetic lenses to control and focus a beam of electrons in an high vacuum environment and scanning the focused beam over a sample surface makes it possible to visualize much smaller structures than possible with optical systems, that is limited by the wavelength of the photons in the visible range. When the electrons interact with the sample, they can either back-scatter or knock electrons off from sample atoms (secondary electrons). The interaction depth and volume is dependent on the energy of the incoming electrons as well as the density of the sample, thus the atomic number of the sample atoms (Z)[53]. The back-scattered or secondary electrons are detected (and attracted using an electric field) commonly to an in-lens ring-shaped detector or to an Everhart-Thornley detector for secondary electrons. The off-axis position of the latter will give a shadow-like effect of the images obtained. As the back-scattered electron possess a much higher energy, and the travel distance is strongly dependent on the energy, back-scattered electron gives information from much deeper into the sample, but gives Z-contrast. Contrary, secondary electrons do not travel so far, and gives more topographical information[54].

As graphene consists of carbon, which is a quite light element ($Z = 6$), and secondly is very thin, secondary electrons are primarily used to image the coatings in this work. However, even though secondary electrons gives more local information, as secondary electrons generated deeper within the substrate do not escape, visualizing the topmost atomic layer is no trivial task.

A number of electron microscopes were used, but most of the experiments were performed in a FEI Quanta FEG 200 and a FEI Helios dual beam microscope.

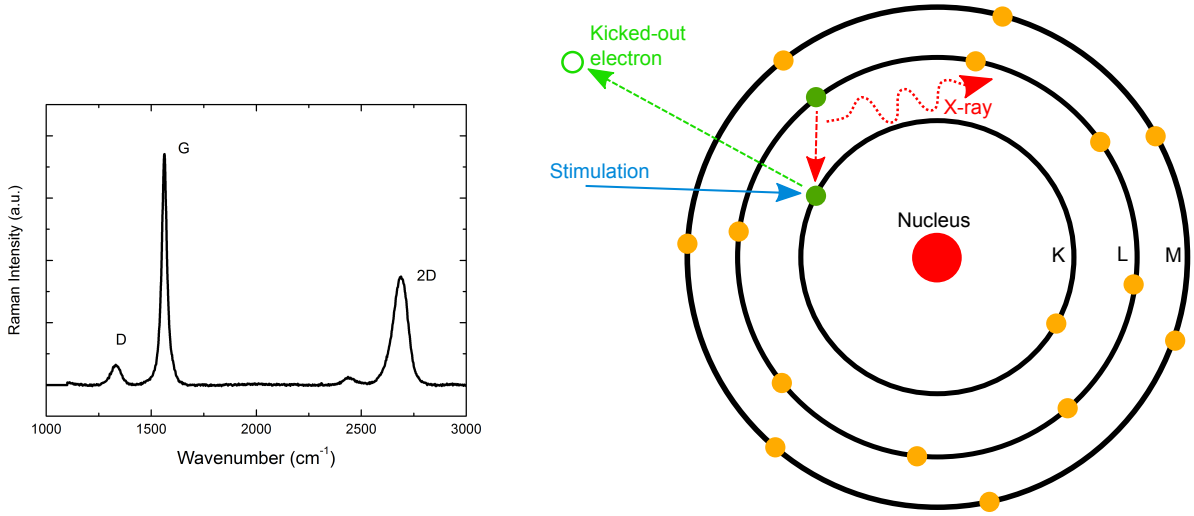

(a) (b)

Figure 3.3: (a) Raman spectrum of multi-layer graphene on nickel. The most distinct peaks are the G-peak, 2D-peak, indicating long range order, and the D-peak, indicating defects and disorder in the graphene lattice. The low I(2D)/I(G) ratio indicate multiple graphene layers. (b) Schematics of EDX of a chlorine atom, where the hole from a knocked out electron is filled by an electron from a higher energy shell and the excess energy is released as an X-ray photon that can be detected.

3.4.1 Energy-dispersive X-ray Spectroscopy

When the electron beam knocks out electron from low-energy shells, such as the K-shell, and at least one electron is present in a higher energy shell, this will eventually decay into the lower energy state. The excess energy released from this mechanism can take the form of an x-ray photon as can be seen on figure 3.3b. In Energy-Dispersive X-ray spectroscopy (EDX) the radiation from the samples is monitored, and by resolving the photon energies, unique pattern can be seen of the element detected. EDX makes it possible to locally (spot size depends on the interaction volume) analyse sample composition. In contrast to XPS (described below) EDX obtains much more local information laterally, however, the signal will get information from much further into the bulk. EDX was useful for detecting oxygen under multi-layer graphene films.

3.4.2 Focused Ion Beam Milling

Some scanning electron microscopes are dual beam systems. That is, besides the electron column for imaging, an extra column for accelerating heavy ions towards the surface is built

into the system. Typically, gallium is liquefied on a tungsten tip and accelerated towards the sample. Depending on its energy, the ion beam can mill away atoms hit by the beam. Ions can be used for imaging, even though they will rapidly change the surface of the sample, but condensing the beam creates a useful tool for cutting, milling and polishing.

To study cross-sections of samples in e.g. a transmission electron microscope, a lamella must be cut out, as the microscope is not able to image samples thicker than a few hundred nanometres (depending on the elements, optimal thickness to stability is typically around 100 nm)[55]. A lamella is prepared after finding a suitable spot on the sample surface. Using a gas injection system with a needle that can be approached to within a few micrometer of the sample, platinum is deposited with the help of the electron beam, and subsequently, when an initial layer is formed, with the ion beam, further protecting the sample surface. Utilizing the ion beam, trenches are milled on each side of the sample, which is then thinned down to $1 - 2$ µm and with a length of $20 - 40$ µm. Afterwards one end is cut of and the sample tilted such that the bottom part can be cut of. A micro manipulator is inserted and welded onto the free end on the lamella again using platinum vapour. The ion beam is used to cut loose the final part of the lamella, which is now only attached to the micro manipulator. The unpolished lamella is transferred to a TEM sample grid, where it is welded onto one of the cantilevers and the micro manipulator cut off. Lastly the sample is rotated so it can be further polished with the ion beam, thinning it down to its final thickness. The procedure can be seen on figure 3.4.

As the lamellae used here typically consist of nickel/multi-layer graphene/platinum, extra careful polishing must be used. Should one side of the lamella be heated up to much, the multi-layer graphene will delaminate, and the sample be rendered useless.

3.5 Transmission Electron Microscopy

Transmission electron microscopy (TEM) uses a high vacuum as the scanning electron microscopy (preferably even lower pressure), however, instead of detecting back-scattered (or secondary electrons) a very thin sample is used, and transmitted electrons are detected. A higher acceleration voltage is used and a CCD array detects the position of the transmitted electrons instead of the scanning approach in the SEM (scanning transmission electron microscopy (STEM) exists, but will not be treated here).

TEM can routinely obtain sub nm-resolution, and state of the art microscope can even resolve sub Angstrom[56]. Contrast is mainly Z-dependent, as a denser structure will block

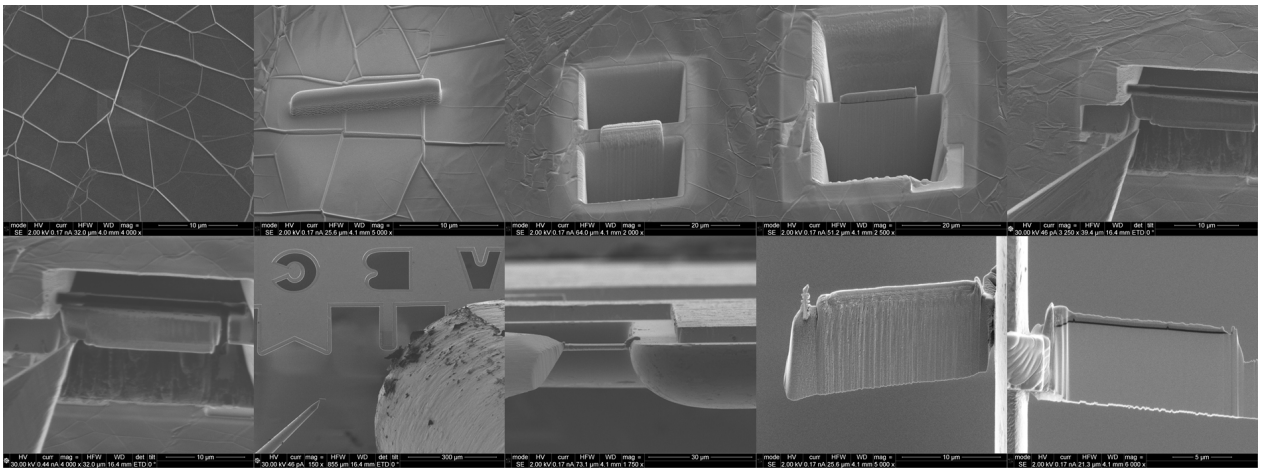

Figure 3.4: FIB lamella cut-out procedure. First the sample surface is protected by platinum, the lamella cut out and welded onto the micro-manipulator, and transferred to the TEM sample grid. Lastly, the final polishing takes place thinning down the sample to approximately 100 nm in width. The lamella shown is a APCVD synthesised MLG on nickel. This particular lamella is investigated on figure 4.4b

more electrons from passing through. Carbon, being only the sixth element in the periodic table, has a low contrast, and will appear lighter on images where e.g. nickel and platinum is also present. Moreover, the low contrast of carbon makes it very difficult to image individual atoms. Rows/layers of graphene is, however, easier to detect.

A TEM usually uses a much higher acceleration voltage than used in a SEM. In the FEI Technai T20 G2 microscope used for the experiments acceleration voltages up to 200 kV can be used, however, high acceleration voltages might damage the samples. The theoretical limit for knock-on damage of graphene sheets, where a carbon nucleus can be displaces by a direct hit from the electron beam is 86 keV of kinetic electron energy, however, in non-perfect graphene damage is also observed in the range of $60 - 80$ keV[57].

3.6 X-ray Photo-emission Spectroscopy

In an UHV environment a sample is bombarded with X-rays. In the Thermo-Scientific Al K-α XPS a spotsize of around 400 µm is typical. The X-ray photons interact with the electrons of the sample, knocking some loose. While the X-rays can penetrate deep into the sample, the photo-electrons can only escape from the top layers of the sample (few nm), without undergoing energy loss processes such as interactions with electron from the sample.[58] Such electrons will only contribute to the obtained spectrum background, while directly emitted

electrons contribute to the spectrum. As the energy of the incoming X-ray photons is known, the photo-electron kinetic energy can be described as

$$E_{binding} = E_{photon} - (E_{kinetic} + \phi)$$

where ϕ is the work function of the apparatus. The binding energies for the electrons gives unique fingerprints for the elements present in and just beneath the sample surface. While each element has its unique electron configuration and thus electron binding energies, hybridization and neighbouring atoms can affect these, making it possible, with a high-resolution system, to distinguish between sp^2 and sp^3 hybridized carbon, as these have binding energies of 284.3 ± 0.1 eV and 285.2 ± 0.1 eV respectively[59]. Even in a lab-source XPS system, such as the Thermo-Scientific Al K-α, some oxidation states are easily identified. For instance copper, where metallic copper and copper(I)oxide 2p electrons have binding energies very close to each other (932.6 eV and 932.5 eV), while copper(II)oxide (933.7 eV) and copper(II) hydroxide (935.1 eV) can be distinguished easily[60].

The different elements will have a different probability of interacting with an incoming X-ray photon, and two evenly strong peaks can thus not be translated directly to an equal amount of two elements. C.D. Wagner made a study of sensitivity factors used in XPS, where for instance a 1:1 ratio of nitrogen and boron (as expected to be found in hexagonal boron nitride) results in the nitrogen peak being between 3.1 and 3.7 times greater than the boron peak, for boron and nitrogen bulk and surfaces respectively [61].

3.6.1 X-ray induced Auger Electron Spectroscopy

As with electron spectroscopy, when a core shell electron is knocked out, an electron from a higher energy shell will decay into its place. The excess energy so released may escape as a photon or as ejecting another (a third) electron from a higher level shell. This electron's energy will highly dependent of the energy deference between the originally knocked out electron and the shell from which the electron that took its place came. This (third) electron is called an Auger electron, and can be detected to give further information from a sample, and is in some cases more sensitive than core level lines[62]. This process is called Auger Electron Spectroscopy, and more specifically when the energy supplied to knock out the original electron stems from an X-ray, the process is called X-ray induced Auger Electron Spectroscopy (XAES).

3.7 Electrochemical Characterisation

While the current state of a coating, with its composition and uptake of species, its performance can be evaluated by simply submerging the test sample in a relevant environment. This can reveal if the coating is effective in certain environments, but is very time-consuming for slow-corroding samples (or high-quality coating) and does not reveal how the coating works.

Electrochemical characterisation, on the other hand, can both be used to perform accelerated tests as well as give further information on the way the coating protects and at which conditions it breaks down. In the following sections the main electrochemical methods used throughout this work are described.

An electrochemical cell consists of a working electrode, which is the sample to be tested, a counter electrode that supplies or received the electrons transferred in the electrochemical process and lastly, and optionally, a reference electrode that does not draw a current and thus maintain a constant potential regardless of the solution used. 3-electrode setups were used for all experiments to get an accurate reference potential. Platinum counter electrodes and silver/silver chloride reference electrodes were used with a Gamry Reference 3000 potentiostat with or without an ECM8 multiplexer for parallel experiments.

3.7.1 Open Circuit Potential

Before any other test, the chemical stability of the system (sample and environment) should be tested. It may take a while before this new system has stabilised, which prerequisites e.g. equalising the temperature and chemical equilibrium. By measuring the potential of the working electrode (sample) against the reference electrode (with infinite resistance between the two, creating an open circuit), this stability can be assessed. When the sample reaches a steady state, the open circuit potential (OCP) will be a constant value. OCP is usually plotted as potential vs time. Here a straight line (even with a slight slope) will be considered stable, an unstable curve will include jumps (which in the case of stainless steel will be local breakdowns of the passivating oxides) and lastly the OCP can be categorized as erratic when the curve jumps several hundred mV in the scale of hours[63].

Firstly, this is important when other experiments are based on a small perturbation of the OCP-value. If the OCP is not stable the results will be very inaccurate. Moreover, any characteristics obtained subsequently using another test method, if the OCP is unstable, will be hard or impossible associate to the test or the unstable OCP.

3.7.2 Potentiodynamic Polarisation

Potentiodynamic polarisation is a technique where the potential of the sample is modified with a constant rate and the response recorded by noting the current through the electrolyte corresponding to the reaction rate of the sample surface. The potential is ramped from a more negative potential towards a positive potential where oxidation and damage to the surface can occur, e.g. $Cu(s) \longrightarrow Cu^{2+}(aq) + 2\,e^-$. At a low enough potential in an aqueous solution, hydrogen evolution will occur through water splitting in neutral and alkaline media $2\,H_2O(l) + 2\,e^- \longrightarrow H_2(g) + 2\,OH^-(aq)$. In acidic media hydronium ions will participate instead and the reaction could look like $H_2O(l) + H_3O^+(aq) + 2\,e^- \longrightarrow H_2(g) + H_2O(l) + OH^-(aq)$[64]. The current will decrease until the minimum current is met at the sample corrosion potential[65]. An increase will be seen at higher potentials, but may be decreased again in the case of self-passivation (seen especially in stainless steels), which will render the current constant even when increasing the potential. At some potential the passivation will be overcome, and the current will increase[66]. Potentiodynamic scans are destructive, and even though a careful and narrow potential interval may limit the damage done to the sample, this characterisation method should be done last as any consecutive results will be affected by the changes to the sample.

Potentiodynamic scans are usually plotted as the absolute value on a current log-scale. In this way, the current minimum is easily seen alongside all other major features on the curve. In the log-scale the two linear parts of the curve on either side of the corrosion potential can be said to be the reaction rates of the cathodic and anodic parts of the corrosion respectively, and the extrapolated intersection of these lines cross at the corrosion current, I_{corr}[8]. On figure 3.5 the concept is illustrated. The corrosion rate of the sample can thus be found with the knowledge of the sample material as

$$CR = \frac{I_{corr} \cdot K \cdot EW}{\rho \cdot A} \tag{3.1}$$

where $K = 3372$ mm/year is the corrosion rate constant, EW is the equivalent weight (29 g for nickel, 31.7 g for copper), ρ is the density (8.90 g/cm^3 for nickel, 8.94 g/cm^3 for copper) and A is the sample area[8]. I_{corr} is in some cases a current density, in which case A cancels out.

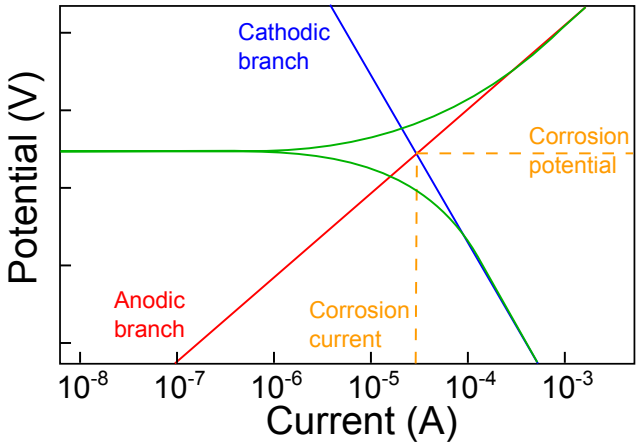

Figure 3.5: Generic polarisation scan with a log scale for the absolute current. The linear parts of the anodic and the cathodic branches are extrapolated, and their intersections noted. At this point the corrosion current, I_{corr}, and the corrosion potential, E_{corr}, can be found.

3.7.3 Electrochemical Impedance Spectroscopy

By using a small AC perturbation to the open circuit potential (few mV), and noting the current response, the samples interaction with the media can be probed. The part of the coatings being insulating or porous can be detected, as a insulating part will behave as a capacitor, and a porous part will act as a resistor. More advanced elements such as Warburg elements (describing diffusion) and Constant Phase Elements (leaky capacitor) are also used a descriptors. Thus, the impedance curve can be fitted with a properly designed equivalent electrical circuit model[67].

The data obtained form an EIS measurement can be plotted either as a Bode-plot, where phase and impedance is plotted as a function of frequency, or as a Nyquist-plot, where the imaginary part of the impedance is plotted as a function of the real part. A Bode-plot can be seen on figure 3.6, where two models have been made; one for graphene on silicon dioxide and one for graphene on copper. By setting up a model containing the electronic equivalents of the coating systems seen on 3.6b and 3.6c, functions can be fitted to the data to determine parameters of the system and confirm the mechanisms at play. However, one need to be careful only to apply models that have a strong physics interpretation, as infinitely complex models can be fitted to nearly any data.

3.7.4 Quick Working Electrode

In a normal corrosion cell, the sample is mounted first, sealed with an o-ring and then the electrolyte is added. For in-situ testing or in the case of a quickly stabilizing sample this is

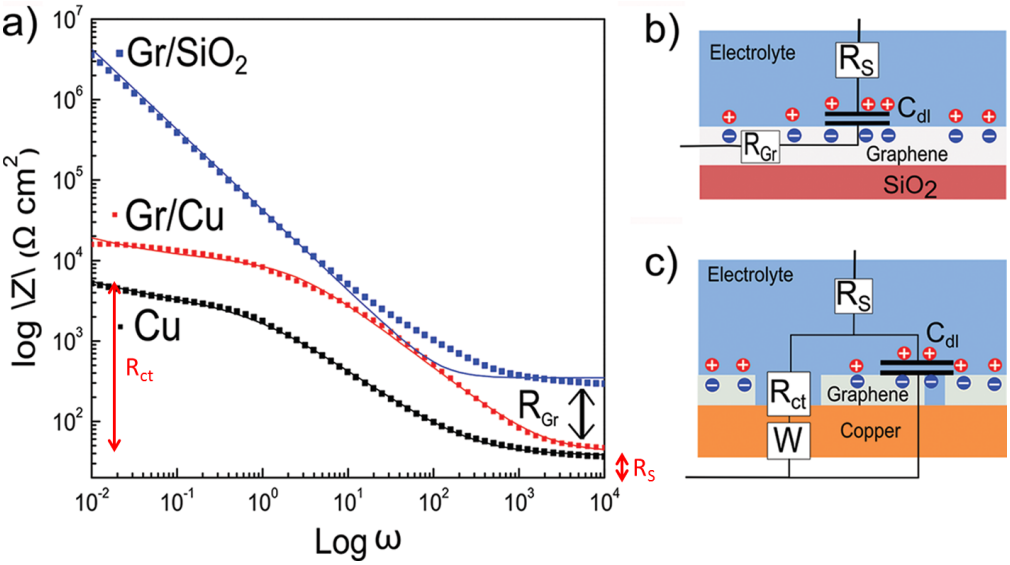

Figure 3.6: (a) Three EIS curves from three different samples. Two models are presented, one for graphene on silicon dioxide (b) and one for graphene on copper (c). The solution resistance, R_S, can be read of from the curve representing model (c) as the impedance at high frequency. Similarly the charge transfer resistance, R_{ct}, can be found from the lowest frequency (indicated by red arrows). *Free from [8]*

not practical, and thus the Quick Working Electrode (Quick WE) was invented[68]. Here the sample is mounted in a auto-contacting holder (that contacts either the front or the backside of the sample) and simply lowered into the electrolyte the sample is to be tested in. The cell design can be seen on figure 3.7a. The cell was fabricated from the polymers PEEK for the rod and PTFE for the main parts of the cell.

The drawings and design of the working electrode holder has been licensed to Gamry Instruments Inc., where it is now, in a slightly modified version, sold as "Flat Specimen Holder", and the commercial version can be seen on figure 3.7b. Gamry has changed the lid-design and also the material choice, so the complete cell is now made of PEEK. Moreover, they have extended the rod. The flyer for the Gamry-version of the invention can be seen in appendix D.

3.8 Atlas Cells

Atlas cells were located at Accoat A/S and were mainly mounted by Susie-Ann Spiegelhauer from Accoat A/S, however, experimental design and analysis of results were done in close collaboration.

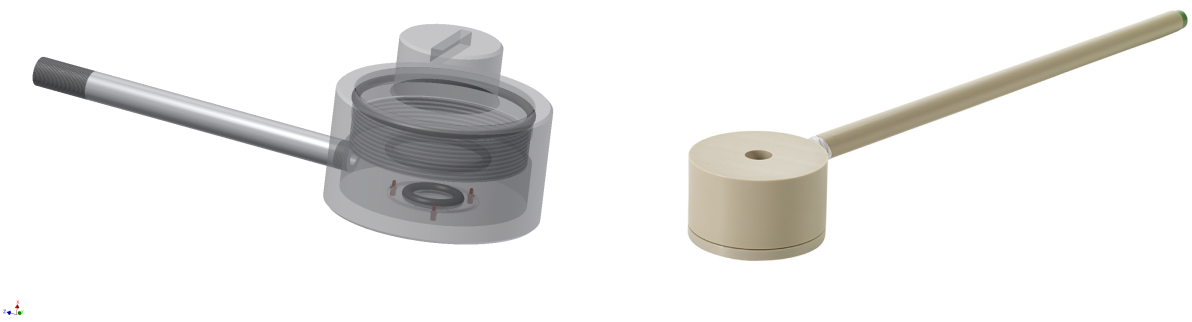

(a) (b)

Figure 3.7: Quick WE design rendering (a) . The end of the rod is kept out of the electrolyte and allows the contact wire to be protected from the possibly harsh environment. (b) shows the commercial version licensed to Gamry Instruments *Reprint from Gamry.*

For harsh or accelerated laboratory testing of coatings Atlas cells are widely used. Here a sample is mounted vertically on a cell half filled with the electrolyte, thus covering half of the sample. During testing the electrolyte is heated to its boiling point, exposing the lower half of the sample to liquid face testing while the top of the sample is exposed to electrolyte vapour. Moreover, the backside of the sample is exposed to ambient air, thus large temperature gradient is applied across the sample. This can, when the coating is not tightly bound to the surface of the sample, give rise to condensation and, thus in time, delamination of the coating[69]. An Atlas cell, both drawn schematically and an image of one of the actual cells used in the project, can be seen on figure 3.8.

Samples are evaluated by optical inspection and compared with a reference, uncoated sample. In the case of thicker coatings, bubbles and delamination can be observed for failed coatings, while in the case of thinner or mere transparent coatings, corrosion of the underlying metal will be observable.

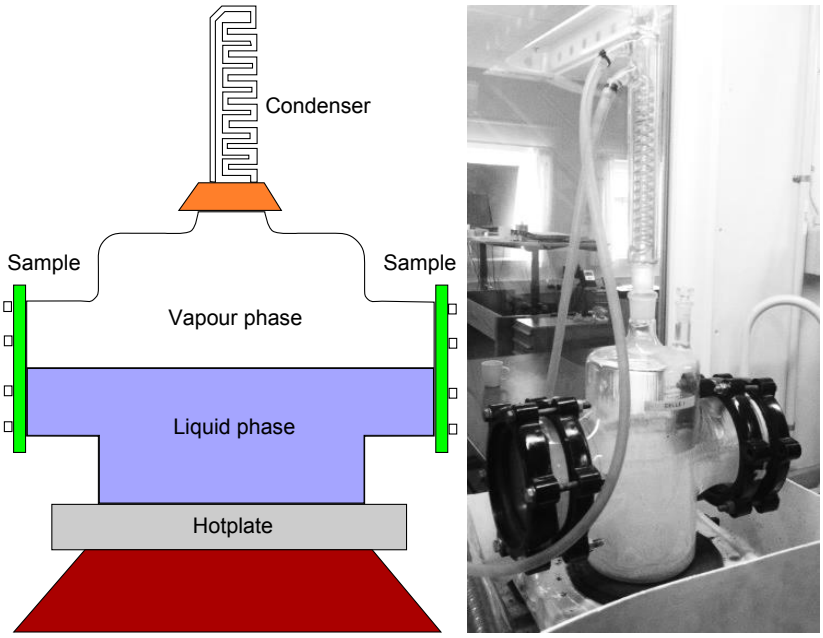

(a) (b)

Figure 3.8: Atlas cell for half-submerged test. (a) Schematic illustration of an Atlas cell with the samples mounted at each side and a liquid level covering half the sample surface. The liquid is held at its boiling point using the hotplate. The system is a closed loop with a condenser. (b) Image of one of the actual Atlas cells used.

Chapter 4

Synthesis

In this chapter the synthesis of two materials is covered. Firstly, synthesis by chemical vapour deposition (CVD) of multi- and single-layered graphene in various systems, and later CVD synthesis of hexagonal boron nitride using a tube furnace as well as a patent pending radiation based method will be described.

Moreover, to have a controllable and consistent surface for coating of steel samples, electroplating was used.

4.1 Synthesis of Multi-layered Graphene

Graphene synthesis using CVD depends highly on the catalytic properties of the substrate, as carbon dissociation and formation of graphite without a catalyst requires temperatures in the excess of 1500 °C[70]. Besides the catalytic properties of a substrate, the carbon solubility and diffusion rate is of great importance for the synthesis process. A high carbon solubility allows for carbon diffusion into the substrate itself at the elevated synthesis temperatures, and if the re-cooling of the substrate is sufficiently slow, the carbon will diffuse back towards the surface and segregate. As the formation of graphene happens in the substrate-gas interface, gaseous carbon diffusion from the gas phase to the catalyst surface will be reduced, as this can mainly occur through defects and grain boundaries once the first layer is formed[71]. Also, carbon atoms diffusing out of the bulk after formation of the first graphene layers will still reach the surface of the substrate and thus consecutive graphene layers can be formed. To form a multi-layered graphene (MLG) coating a catalytic active substrate with some carbon solubility is preferred.

On of the most used metals for MLG synthesis is nickel, and as nickel itself has good

chemical resistance to many corrosive agents [7, 8, 72] and can be electroplated onto another metal it was chosen as the main candidate for MLG synthesis. The thickness of a final coating can to some degree be controlled. The carbon solubility in nickel is a function of temperature[73], but since the quality of the synthesized graphene is also a function of the process temperature, one cannot be changed without also altering the other. The graphene quality can be seen on figure 4.1a, where we have used the same synthesis process, just varying the annealing and synthesis temperature. Simply lowering the temperature will result in a more amorphous carbon layer. One way of changing the thickness of the graphene layers is by changing, the amount of carbon in the reaction chamber. However, this not only requires a high-vacuum environment (it only takes 77 ng·cm^{-2} to make a complete graphene layer), but also a high control of the carbon distribution. Second-layer formation can start locally before the first layer is completed. A third option is to drastically reduce the nickel thickness to such a degree where the layer thickness limits the amount of carbon that can be segregated[74]. Alternatively, rapid cooling would hinder carbon to escape the nickel. As recently suggested by Cabrero-Vilatela and coworkers[75], a thick catalyst, where it is possible to balance the diffusion into the nickel with the carbon flow from the gas phase to the sample surface can be used for single layer (SL) synthesis. As the first layer is formed, the amount of carbon reaching the nickel surface from the gas phase will be limited by the first graphene layer, and the diffusion rate into the nickel can become dominant hindering the surface supersaturation required for graphene synthesis.

When the catalyst is not to be removed after synthesis, the amount of carbon in it can have significance, as this will change the mechanical properties of the catalyst layer. Here a reduced cooling rate can bring back some of the carbon from the bulk (and help distribute the rest).

In this work a nickel catalyst was used for multilayered graphene coatings. The multilayer graphene film itself might be thick compared to single layer coatings, but is still extremely thin compared to conventional coatings [76]. A schematic illustration of a growth process can be seen on figure 4.1b.

4.1.1 Plating of Samples

Several types of samples were used for synthesis of multi-layer graphene. In some experiments pure nickel foils were used, however, few real-world applications concern protecting pure nickel from corrosion/oxidation, and thus a strategy for protecting other metals was demonstrated.

Electroplating metal surfaces with nickel is a widely used process[78]. However, as the

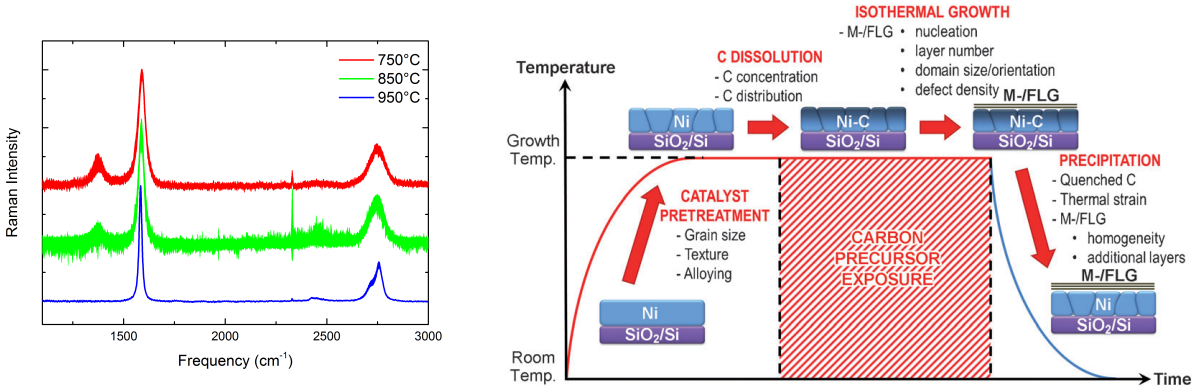

(a) (b)

Figure 4.1: (a) Average Raman spectra (with standard-deviation as the line thickness) of graphene synthesis on nickel using the same recipe, but varying the annealing and synthesis temperatures. The I(D)/I(G) can be seen to decrease with increasing temperatures. The variations also becomes smaller and the shape of the 2D peak resembles that of AB-stacked graphene for the synthesis at 950°C. (b) CVD-process schematics *from [77]*

subsequent high temperatures used for graphene synthesis can affect the structure of the substrate, it cannot be assumed that any thickness of electroplated nickel will be effective as a blocking layer and elements from the underlying metal can diffuse to the surface and affect graphene formation. Synthesis of graphene was attempted on $100-200$ nm nickel thin films on stainless steel, however, graphene formation was not observed. Moreover, thin nickel catalysts have been shown to result in inhomogenities in the thickness of the graphene film along with a higher number of defects as a result of smaller nickel grains[75].

To promote homogeneity, steel samples were glass blasted prior to electroplating. Pre-cleaning consisted of 20 minutes of sonication in Triton X, which is a non-ionic surfactant required due to clean-room regulations. Non-steel samples were first coated with a 10 nm layer of pure nickel using electron-beam evaporation in a Wordentec commercial deposition system, while steel samples were directly inserted in the electroplating setup.

A Technotrans microform 200 system with a 60 RPM rotating electrode setup was used for uniformity of the deposition. The aqueous solution of nickel sulfamate, boric and sulfamic acid was manually kept at a pH of approximately 3.8 and the temperature of the bath regulated to 52 °C. Each plating process was initiated at a low current (0.1 A), preventing huge locals current in case an oxide layer is blocking most of the surface. Likewise, in the case of nickel thin films, commencing at full current would lead to heating up of the thin nickel layer. After initial deposition the current could be ramped up to the maximum deposition

current of 7.5 A for the Ø2" samples.

While electroplating nickel is a well understood and efficient way of coating samples, electroless (EL) nickel plating has several advantages. EL plating results in better coverage of corners, kinks and edges. Moreover, the electroless technique can be used on insulating substrate, hugely increasing the range of materials that can be plated[79]. On figure 4.2a a Raman spectrum of a steel sample plated with approximately 10 µm EL nickel can be seen. The graphene was synthesised using a recipe that will be described later (APCVD-recipe in the AS-ONE system). The results seems similar to the synthesis observed for nickel foils, including the lack of a clear D-peak.

Besides providing a more flexible platform for graphene synthesis, EL nickel in itself also has some properties desirable for a coating system; EL nickel is known to have excellent abrasion protection along with a high resistance towards corrosion[72].

4.1.2 CVD-synthesis Recipes

The syntheses performed early in the project were perfomed in the home-built CVD-system, but later the used recipe was transferred to the AS-ONE system. Representative examples of synthesis from the two systems using the same recipe can be seen on figure 4.2b. The spectra are somewhat similar, however, the D-peak of the synthesis in the AS-ONE system is considerably smaller. This coheres well with the fact that a higher vacuum can be obtained. Moreover, a failure rate of around 25% was observed for the home-built system (where a very large D-peak could be seen). A "successful synthesis" can be seen in blue, where the D-peak is still clearly apparent (D/G-intensity ratio of 0.17 ± 0.02), while it is more than an order of magnitude lower in the AS-ONE synthesis (red) (D/G-intensity ratio 0.011 ± 0.005). Besides the D-peak, the 2D-peak of the home-built system has a single broad peak, while the AS-ONE has two peak-shapes (seen on the widening of the standard deviation on the left side of the 2D peak. The main peak is shifted towards a slightly higher Raman frequency. This indicates some turbostratic growth in the home-built system, while the 2D-peak of the AS-ONE synthesis indicates areas of AB-stacking, and areas with some turbostratic stacking[80]. However, some stacking must occur in all spots, as a purely turbostratic graphene spectrum resembles that of single layer, with a I(2D)/I(G) peak larger than unity[81].

The recipe used for most of the multi-layer graphene synthesis consists of the following steps:

Low Pressure CVD recipe "ACS-stdGonNi"

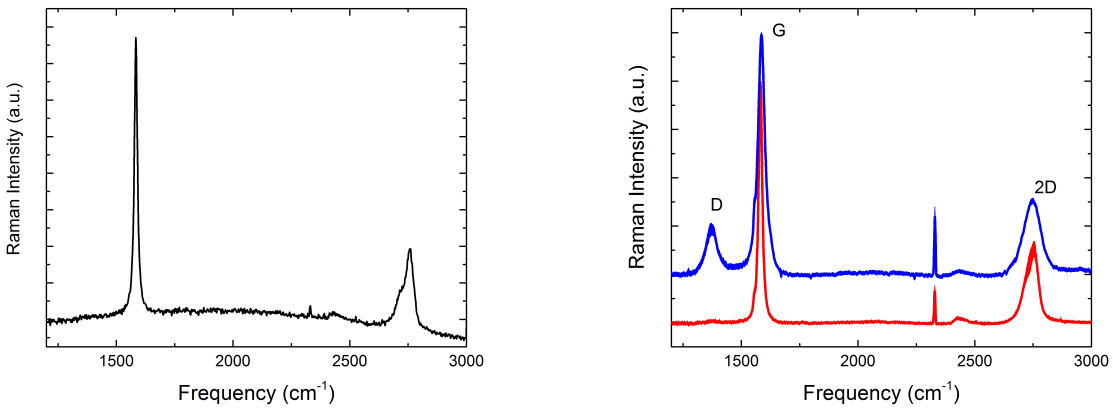

(a) (b)

Figure 4.2: (a) Raman spectrum of graphene gown on electroless nickel coating on steel. (b) Raman spectra of the most used recipe for multilayer growth "ACS_stdGonNi" performed in both the home-built system (blue) and in AS-ONE (red). The spectra have been normalized to the G-peak. The curve thickness represent the standard deviation.

1. Pre-cleaning of the substrate (using IPA and blow-drying in nitrogen).
2. Purging, emptying the reaction chamber by consecutive pumping and filling with pure nitrogen. Repeated 3 times.
3. Heating of the substrate to the annealing/synthesis temperature of 850 °C.
4. 10 minutes of annealing under 100 sccm hydrogen flow with the pressure held at 5 mbar.
5. 10 minutes with a flow of hydrogen (24 sccm) and acetylene (12 sccm) with the pressure held at 5 mbar.
6. Cooling at a controlled rate (0.5 °C/s).

The temperature, pressure and flow of hydrogen and acetylene can be seen on figure 4.3a in the home-built system and on figure 4.3b in the AS-ONE system. The recipe is generally identical (except for the integrated flushing procedure in the AS-ONE), however, a much more precise control of the parameters is apparent in the commercial system. Especially the pressure is better kept constant, and the base pressure is lower. This may account for the higher number of defects in the synthesized graphene from the home-built system as seen on figure 4.2b.

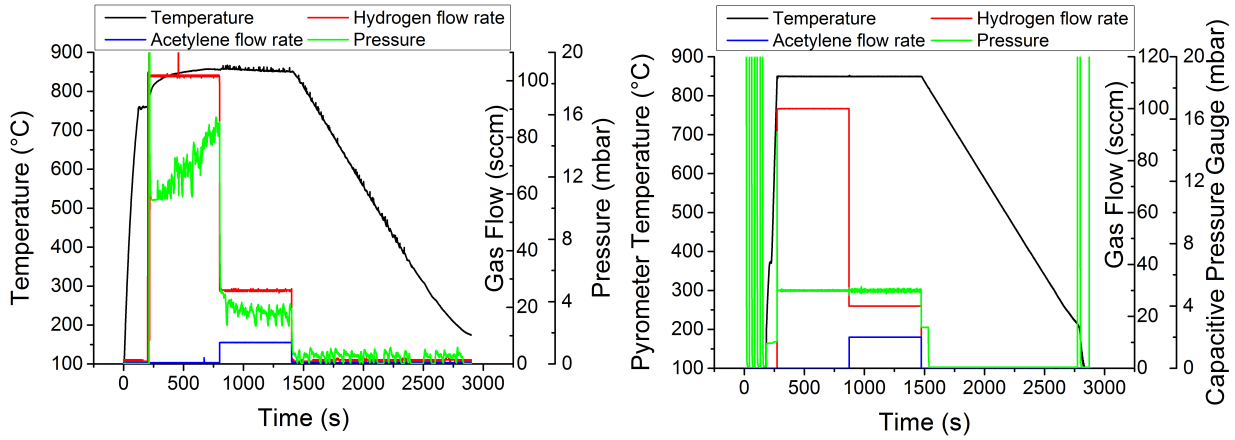

(a) (b)

Figure 4.3: Actual growth process using the "ACS-stdGonNi" recipe in the home-built system (a) and in the AS-ONE system (b). On (b) the flushing of the system before and after the synthesis is integrated in the recipe, and account for the extra variations in pressure before and after the synthesis itself. Generally a much more precise control of the parameters is apparent in the AS-ONE system - especially regarding the pressure, where both the stability and base pressure is much improved.

While low-pressure CVD to some degree limits the number of layers by limiting the partial pressure of carbon, atmospheric pressure CVD (AP-CVD) gives rise to an even thicker coating. Modifying the recipe developed by Reina and coworkers[82], the following recipe was developed

Atmospheric pressure CVD recipe "APCVD"

1. Pre-cleaning the substrate (using IPA and blow-drying in nitrogen).
2. Purging; emptying the reaction chamber by consecutive pumping and filling with argon. Repeated 3 times.
3. Start of high argon flow (2000 sccm).
4. At 1 atm pressure, change flow to 120 sccm argon and 100 sccm hydrogen.
5. Heating of the substrate to the annealing/synthesis temperature of 950 °C.
6. Keep the temperature and flow for 15 minutes annealing.
7. Change gas flow to 2 sccm acetylene and 100 sccm hydrogen during the synthesis (10 minutes - 30 minutes).

8. Pump down the system while cooling at a rate of 20 °C/s.

The gas exchange rate - the rate at which the volume of gas in the reaction chamber is replaced - may be a better descriptor than the flow rate through the MFC's to describe a recipe than just a flow rate that does not include the systems geometry. However, the flow ratios are important. As the volume of the reaction chamber in the AS-ONE system is only 1 litre, the flow rates were regulated to smaller values than in the original recipe. Moreover, in the original recipe, the acetylene to hydrogen ratio was kept at between 0.3%-1.7%. In this modified version the acetylene to hydrogen ratio was kept at 2% for up to 6 times longer. By increasing the fraction of acetylene, the synthesis rate increases, and the removal rate of less stable carbonaceous species by the hydrogen decreases[83], highly increasing the combined synthesis rate. Lastly, the recipe was modified using a controlled cool-down rate, as this results in control of the rate at which carbon leaves the nickel bulk, which had previously been found to affect the quality[84] as well as the thickness[85] of the graphene film synthesized,.

On figure 4.4a the synthesized graphene is visualized using SEM. The wrinkles are easily visible, stemming from the different thermal expansion coefficients of nickel (positive) and graphene (negative)[86]. Cooling down from the high growth temperature (950 °C), nickel will therefore contract and the graphene expand. To release the stress that builds up in this process, graphene will form wrinkles. The wrinkles do, however, indicate some level of graphene quality and flake size, as smaller non-coherent flakes might slide in under each other instead due to the extremely low friction of graphene films[87].

On figure 4.4b a TEM cross section of a synthesized film was made using a FIB technique. Here the individual layers can be seen, and the thickness of the film is estimated to be in the region of 100 nm or roughly 300 layers; a large increase from the original recipe from Reina and coworkers, that in average led to approximately 10 layers[82]. The individual layers can also be seen to be parallel to the nickel surface and they do not appear to cross each other, thus no clear vertical channels can be seen. On figure 4.4c, two representative Raman spectra can be seen, one from a region with more turbostratic graphene, and one from an AB-stacked region[80]. The I(2D)/I(G) ratio indicates the multi-layer nature of the film, and the small D-peak witnesses the high quality with a I(D)/I(G) ratio of 0.040 ± 0.010, even with the increased acetylene to hydrogen ratio in the synthesis process. The shape of the 2D-peak, with a shoulder at lower Raman shifts, indicate a high stacking ordering of the graphene layers as is present in HOPG[46].

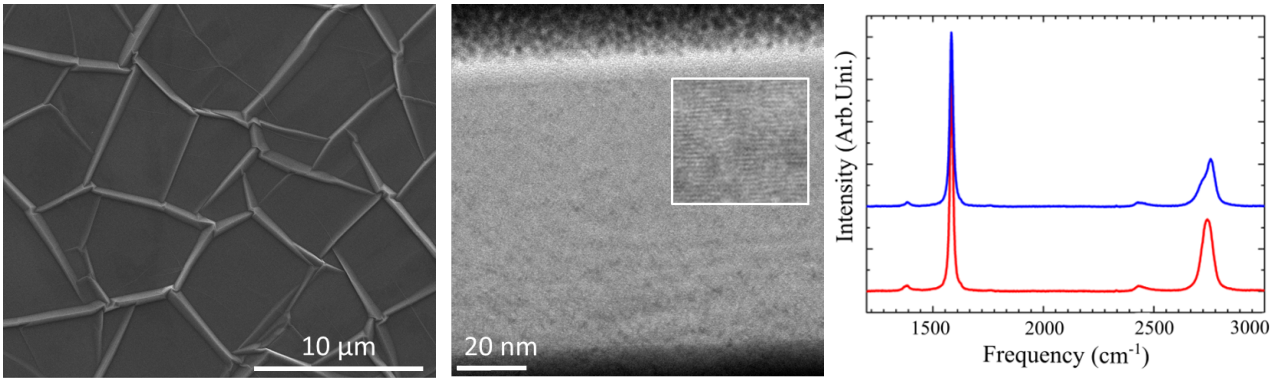

(a) (b) (c)

Figure 4.4: The result of the APCVD recipe for graphene syntheses. (a) is a SEM image of the surface of the coating where wrinkles can be seen stemming from the different thermal expansion coefficient of the underlying nickel and the graphene. (b) is a TEM image of the graphene film. Here the individual layers can be seen being parallel to the surface of the nickel. (c) is two representative Raman spectra, from a turbostratic region (red) and from and AB-stacked region (blue), both indicating a very low number of defects.

4.2 Synthesis of Single-layer Graphene

This recipe was developed in collaboration with M.Sc. student Miriam Galbiati.

Opposed to the method used for synthesizing MLG, single layer graphene (SLG) is easily formed on some catalytic substrates with low or no carbon solubility such as copper or platinum. In this work, synthesis have been mainly performed using copper as a catalyst and methane as the carbon precursor [17, 83, 88–90]. Using acetylene results in nucleation spots of local MLG, and a much larger defect density.

1. Pre-cleaning of samples and flushing 3 times with argon.
2. Copper heated to 1035 °C in atmospheric pressure of argon (1000 sccm flow).
3. Annealing at this temperature for 10 minutes.
4. 900 sccm argon along with 2 sccm of methane and 60 sccm of hydrogen for 15 minutes synthesis.
5. Rapid cooling (power off) under 900 sccm argon and 60 sccm hydrogen flow.

As with the multi-layer synthesis, the quality of the fabricated graphene depends on the temperature. Copper melts at approximately 1083 °C at atmospheric pressure[91], and close

to this temperature the vapour pressure will be high. Moreover, local temperatures may differ from those measured by the pyrometer, which can lead to unwanted melting and evaporation. To minimize these phenomena, an optimal balance was found at 1035 °C were the graphene quality was high and copper evaporation was limited. The 1:30 ratio between methane and hydrogen results in an aggressive removal of unwanted carbon allotropes[83].

Raman spectra obtained directly on the copper surface can be seen on figure 4.5a. The spectra have a high noise level, as the response is limited when the graphene is coupled to the un-oxidized copper. A small D-peak is just visible, which is described in further details in section 3.3. The intensity ratio between the 2D-peak and the G-peak would on silicon dioxide normally indicate multiple layers, but not directly on Cu[47]. The FWHM of the 2D-peak of approximately 40 cm^{-1} may indicate stretching or doping of the graphene[90].

4.3 Synthesis of Hexagonal Boron Nitride

Hexagonal boron nitride (hBN) can be synthesized in a similar way to graphene, but being a diatomic structure requires either two precursors or a more complex precursor containing both elements. In literature a common precursor is ammonia borane ($BH_3{-}NH_3$) [92, 93]. In this project, however, borazine molecules ($B_3H_6N_3$) were used as a precursor. Borazine, being a liquid at room temperature, was bubbled using argon. Moreover, prolonged storage of borazine at room temperature can result in polymerization. Therefore a setup was constructed, where the borazine bubbling canister was stored in a freezer with inlaid gas-lines inlet for argon and an outlet for bubbled borazine/argon.

Using the tube furnace, hBN was synthesised as described in the following recipe:

hBN tube furnace recipe

1. Pre-cleaning of samples and flushing of system 3 times with argon.
2. Copper samples were heated to 900 °C under vacuum.
3. 300 sccm of argon was let into the system and the variable pump valve was adjusted to ~ 60 torr.
4. 15 minutes of synthesis with 5 sccm argon-bubbled borazine and 15 sccm hydrogen.
5. Cooling under argon flow.

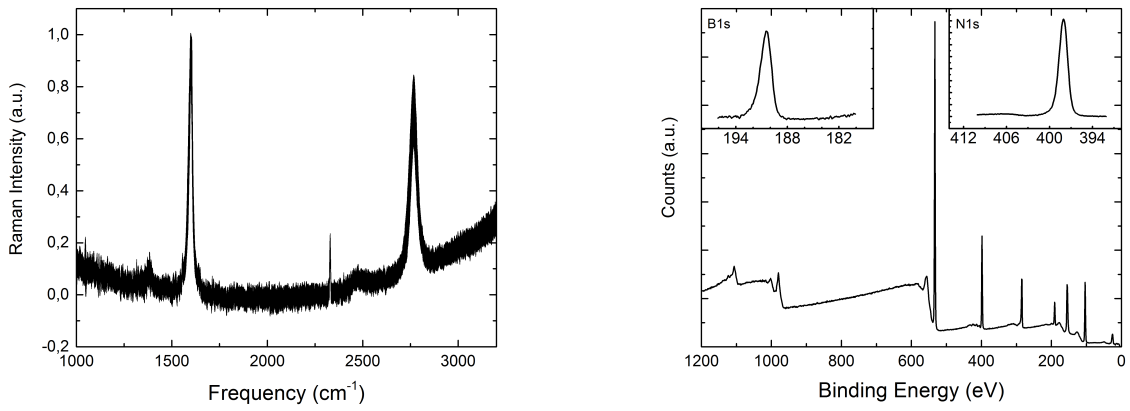

(a) (b)

Figure 4.5: (a) Averaged Raman spectra where the line thickness is the standard deviation obtained directly on the copper surface at 455 nm excitation wavelength (from 30 original spectra). The graphene is single layer. The low I(2D)/I(G) ratio is due to wavelength and substrate-dependence[47]. (b) XPS-spectra of synthesized hexagonal boron nitride on copper. Inserts of B1s and N1s spectra. Ratio between N1s and B1s signal is approximately 3.7:1. As the surface sensitivity of nitrogen 1s is 3.67 times higher than that of boron 1s, the B:N-ratio is 1:1[61]

The 1:3 ratio of argon-bubbled borazine and hydrogen resulted in a 1:1 ratio between boron and nitrogen, as revealed by XPS on figure 4.5b, while a continuous film could be observed in SEM for synthesis of approximately 15 minutes. Decreasing the synthesis duration to 5 minutes results in unconnected hBN flakes, while further increasing the duration beyond 15 minutes until 30 minutes did not result in detectable changes in the XPS signal nor from the images obtained using SEM.

4.3.1 Pulsed hBN Synthesis

As borazine is an infrared-active molecule, the use of this in the infrared-radiatively heated AS-ONE system results in immediate decomposition and subsequently deposition on all surfaces in the chamber, including the quartz-window. This in turn blackens, increasing its absorption of the infrared radiation and ultimately heats it up with the risk of breakage, due to large temperature gradient between its water-cooled sides and its actively heated centre. To circumvent this problem an alternative strategy was utilised, wherein the synthesis was divided into small steps consisting of vacuum-heating to a desired temperature, turning off the lamps and waiting 1 second before injecting borazine. After a short duration the gas flow

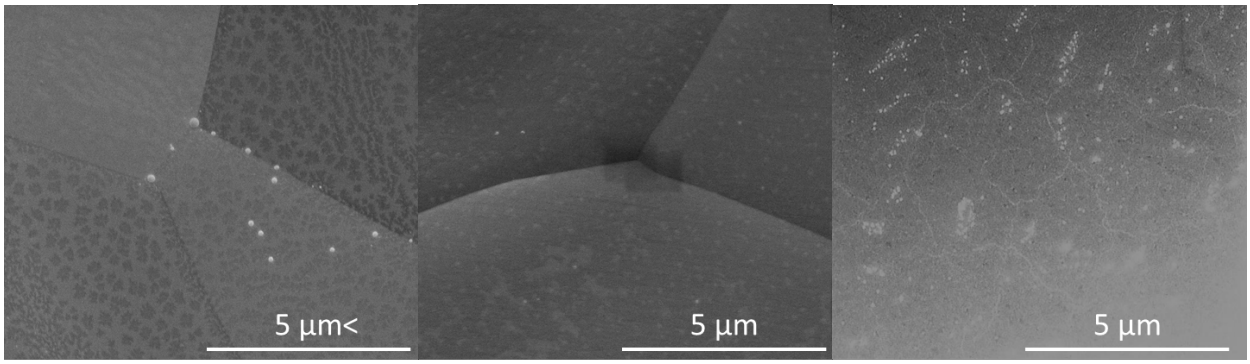

(a) (b) (c)

Figure 4.6: SEM images of hBN on copper foil after 3 (a), 6 (b) and 10 (c) pulses. The hBN film synthesis can be seen to be controllable.

was stopped and the system pumped down to reduce the amount of borazine present in the chamber to a very small fraction of the normal synthesis pressure. This was repeated a number of times, and using this technique we were able to obtain a high control of the hexagonal boron nitride synthesised, starting from single triangular flakes after 3 pulses, over connected flakes after 6 pulses and finally a complete film after 10 pulses, as can be seen on figure 4.6. Publication 7 describes this method and the patent application has been submitted[94].

Chapter 5

Single-Layer Coatings

This chapter will cover the testing of single layer coatings, both made of graphene and hBN, focusing on oxidation protection is based on paper 4. *This is mainly based on the manuscript, where the work was done in close collaboration with my student, Miriam Galbiati. I have supervised the work with Dr. Luca Camilli, designed many of the experiments and either done the practical work or been part of it and instructed M. Galbiati in how it should be done.*

5.1 Oxidation Resistance of Single-layers Hexagonal Boron Nitride and Graphene Barrier Coatings

In this section single layer graphene coatings are compared to similar systems based on hexagonal boron nitride. Due to the widely different electronic properties of the two materials, their protective behaviour is also remarkably different, even though both 2D materials have similar barrier properties[95, 96].

Single layer graphene barrier coatings have been widely described in literature[6, 7, 12, 16], and some attention has also fallen on hBN[31, 95, 97], however, although graphene research has progressed to a stage where centimetre sized single crystals can be synthesised on copper[89], the same is not the case for hBN, where single crystals are much smaller[98]. The quality is also harder to asses with techniques such as Raman spectroscopy, as only a single peak in the Raman spectrum arise with an intensity approximately 50 times smaller than that of the G-peak in graphene[52]. The protective properties of high quality hBN can nonetheless easily be demonstrated, as can be seen on figure 5.1a, where a shortened tube furnace synthesis of 5 minutes produces individual flakes. By placing the 25 µm thick copper foil, which was used for the synthesis, on a hotplate, the surrounding copper oxidises,

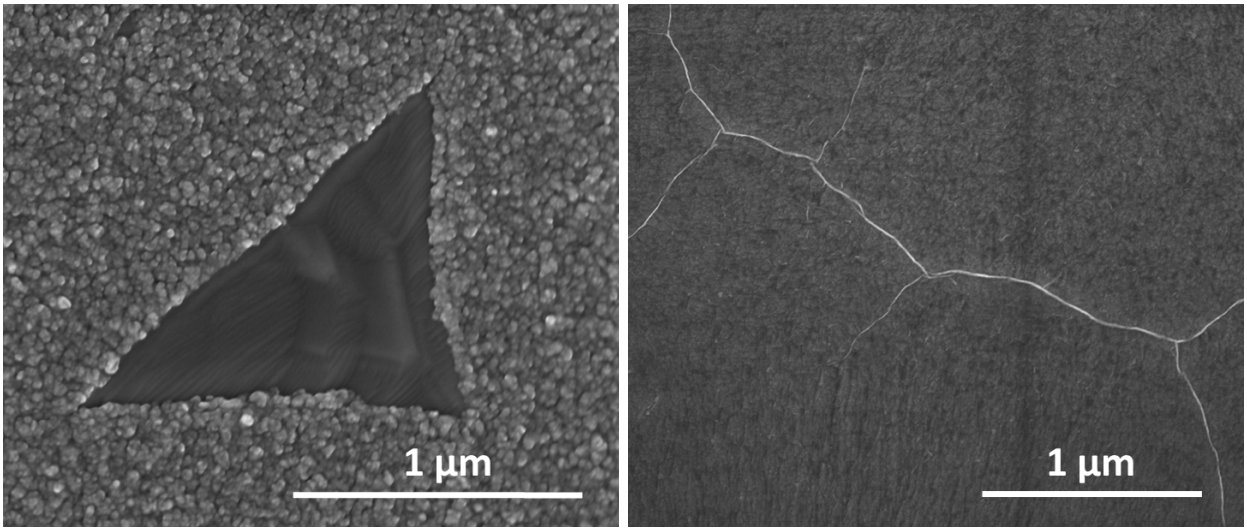

(a) (b)

Figure 5.1: (a) Image of a hBN grain after 5 minute of synthesis and subsequent oxidation on a hotplate. The area under the grain appears darker and smoother, and exhibit visible step edges, indicating the copper is unoxidised, while the surrounding region of the copper can be seen to be oxidized. (b) Full coverage hBN after similar hotplate exposure. No signs of copper oxidation can be seen. Wrinkles have formed due to the different thermal expansion coefficients of the materials and can be seen due to a higher secondary electron yield from the out-of-plane nature of the wirnkles.

however, the area under the hBN flake seems unaffected. Extending the synthesis time to 15 minutes or above results in full coverage, which can be seen on figure 5.1b for a 30 minute process. The sample had been placed on a hotplate in a similar fashion, but no apparent oxidation had taken place. Moreover, a clear wrinkle can be seen running through the SEM micrograph, indicative of the thin film with a different thermal expansion coefficient from the copper underneath. The presence of hBN was also confirmed with XPS from the 1:1 ratio of nitrogen and boron.

Ambient air exposure of copper form the following three oxides: Cu_2O, $Cu(OH)_2$ and CuO[99]. Cu_2O is the native oxide of copper, and is readily formed in the reaction

$$4\,\mathrm{Cu(s)} + \mathrm{O_2(g)} \longrightarrow 2\,\mathrm{Cu_2O(s)} \tag{5.1}$$

The copper in copper(I)oxide can be further oxidised in the reaction[100, 101]

$$2\,\mathrm{Cu_2O(s)} + \mathrm{O_2(g)} \longrightarrow 4\,\mathrm{CuO(s)}$$

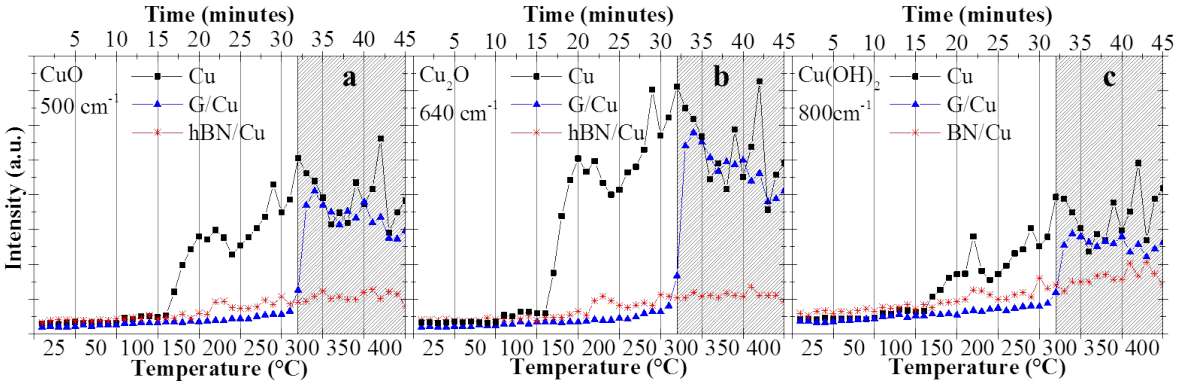

Figure 5.2: Evolution of the Raman signal intensity of Cu_2O, $Cu(OH)_2$ and CuO on pristine copper (Cu), graphene coated copper (G/Cu) and hexagonal boron nitride coated copper (BN/Cu). The grey area indicates the region where the graphene film itself is oxidised, exposing the copper surface. *From publication 4*

Moreover other compounds, such as copper(II)hydroxide ($Cu(OH)_2$) are expected to be present in wet air oxidation[99].

In the following graphene and hBN coatings ability to reduce oxidation of copper samples were compared. Tests were conducted in a commercial Linkam stage (LN600P), where atmosphere and temperature could be controlled while the sample surface could be studied using optical microscopy or Raman spectroscopy. Two sets of experiments were performed, one at which the temperature was increased stepwise from room-temperature up to 400 °C, while in the other experiment the temperature was kept constant at 50°C.

On figure 5.2 the presence of Cu_2O (around 640 cm^{-1}[6, 102]), $Cu(OH)_2$ (800 cm^{-1}[102]) and CuO (500 cm^{-1}[6, 31]) is monitored using a single spot directly on samples. Each temperature was held for 5 minutes while collecting spectra and then rapidly increased to the next temperature level. At around 150 °C the oxidation of the pristine copper is apparent, while the signal from the graphene and hBN-coated samples only indicates mild oxidation. The clear rate change of copper oxidation have been described previously at this temperature[103]. At 300 °C the graphene coated sample is rapidly oxidised, while the hBN-coating remains protective. The failure of the graphene coating becomes apparent on figure 5.3a, where the part of the Raman spectrum indicating the graphene film is shown (full spectra on figure 5.3b). First the initial spectra at 25 °C is seen. In the next spectrum at 300 °C surface oxide decouples graphene from the copper, enhancing the signal strength[48], however, in the last spectrum no graphene can be detected, at the exact same time as the rapid oxidation of the copper begins.

An isothermal experiment was conducted to test the longevity of the coatings at milder

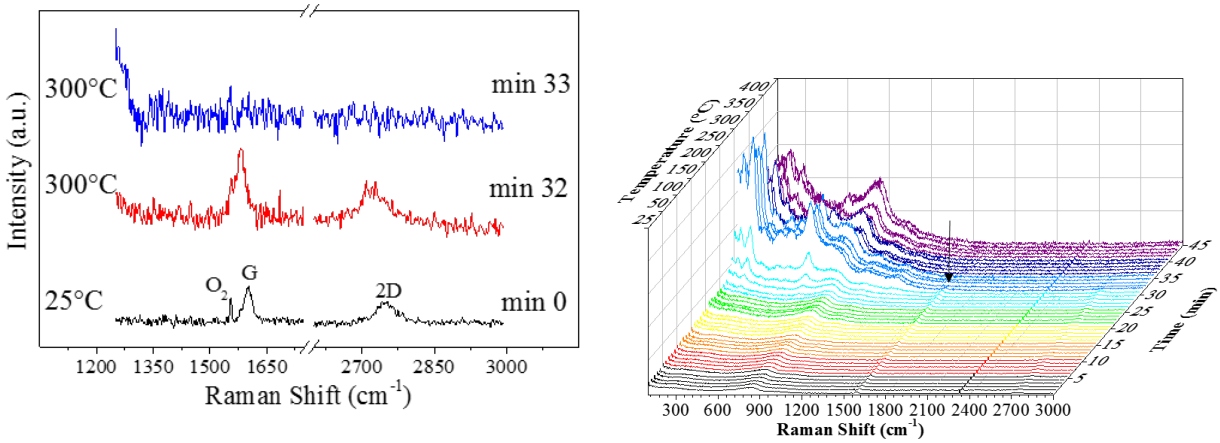

(a) (b)

Figure 5.3: (a) Cropped Raman spectra from the initial temperature (25 °C), from 300 °C, where the graphene peaks are red-shifted and has increased in intensity[48] and lastly shortly afterwards no graphene was detected. On (b) this point in time can be seen indicated by the black arrow. At this point the low wave-number peaks rapidly form, indicating the built-up of oxides. *From publication 4.*

conditions. In figure 5.4 samples similar to those tested with temperature steps are held at 50 °C for 60 hours. As in the stepwise temperature test, the pristine copper is the first to oxidise measurably. The graphene-coated sample seems well protected for the first 9 hours, after which both Cu_2O and CuO is formed. Curiously, the hBN-coated sample only experiences slight increase of all the oxide peaks through all 60 hours of testing.

On figure 5.5 XPS and XAES spectra of copper obtained from untested, variable temperature experiments and from the isothermal experiments are displayed. As the $2p_{3/2}$ peak of Cu and Cu_2O only differ by 0.1 eV they are indistinguishable with a lab-source XPS system such as the one used and described in section 3.6.

The $2p_{3/2}$ peak of pristine copper can be seen to have three components; one at 932.7 eV corresponding to metallic copper and Cu_2O, one at 934.0 eV corresponding to CuO and lastly one at 935.1 eV indicating $Cu(OH)_2$[99]. However, both the graphene-coated and the hBN-coated samples could be fitted by a single curve at 932.7 eV. By inspecting the more sensitive XAES spectra[62], more than one peak is apparent, but the metallic peak at 568.3 eV is the clearly most dominant for the coated samples. The metallic peak is still evident for the pristine copper, but a high contribution from other states, especially the peak at 570 eV, is detected.

After the stepwise temperature experiment, all spectra looks quite alike, both for the

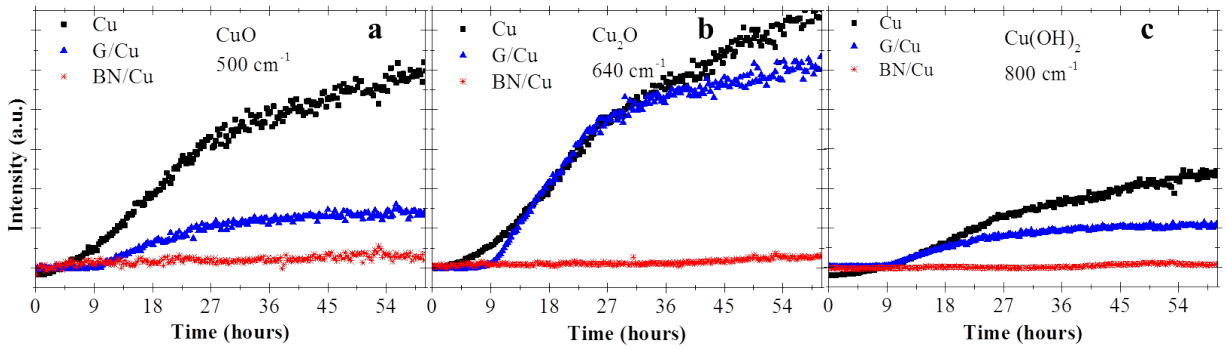

Figure 5.4: Raman intensities for the peaks representing Cu_2O, $Cu(OH)_2$ and CuO in the isothermal experiment held at 50 °C for 60 hours. The pristine copper is quickly oxidized, the graphene-coated sample starts oxidizing after 9 hours, while the hBN-coated sample seems largely protected for the duration of the experiment. *From publication 4.*

	Stepwise Temperature			Isothermal		
	Cu	G/Cu	BN/Cu	Cu	G/Cu	BN/Cu
Cu and Cu_2O	38	41	42	59	77	94
CuO	45	44	43	19	9	4
$Cu(OH)_2$	17	15	15	22	13	2

Table 5.1: Elemental analysis after the stepwise temperature ramp and isothermal experiments. All values are in percent. The stepwise temperature experiment does not reveal a large difference between the sample surfaces, however, in the isothermal experiment the hBN-coating is only slightly oxidized, and the graphene coating still seems to protect the surface to some degree compared with the pristine sample.

pristine copper sample and for the coated ones, with a high contribution from the oxide states (935.1 eV and 934.0 eV). This can be summarised in an elemental composition analysis, which can be seen in table 5.1. This lack of a clear difference between the samples can be ascribed to depth sensitivity of the technique used; XPS is only sensitive to the top few atomic layers, while the laser in the Raman system easily penetrates the semiconducting copper oxide and will get information from much further into the sample. More surprising is the absence of boron and nitrogen signals from the XPS after the experiment. By stopping the experiment at a lower temperature, we observed that the coating signal disappears at a temperature around 350 °C. On figure 5.6a XPS-spectra of boron and nitrogen on samples where the experiment was stopped at 300 °C, 350 °C and 400 °C is shown.

Returning to figure 5.5, the isothermal experiment reveals a different story. From the core level $Cu2p_{3/2}$ spectra, the pristine copper is clearly more oxidised than before the experiment, while the graphene coated is clearly less oxidised than the copper with the 932.7 eV peak

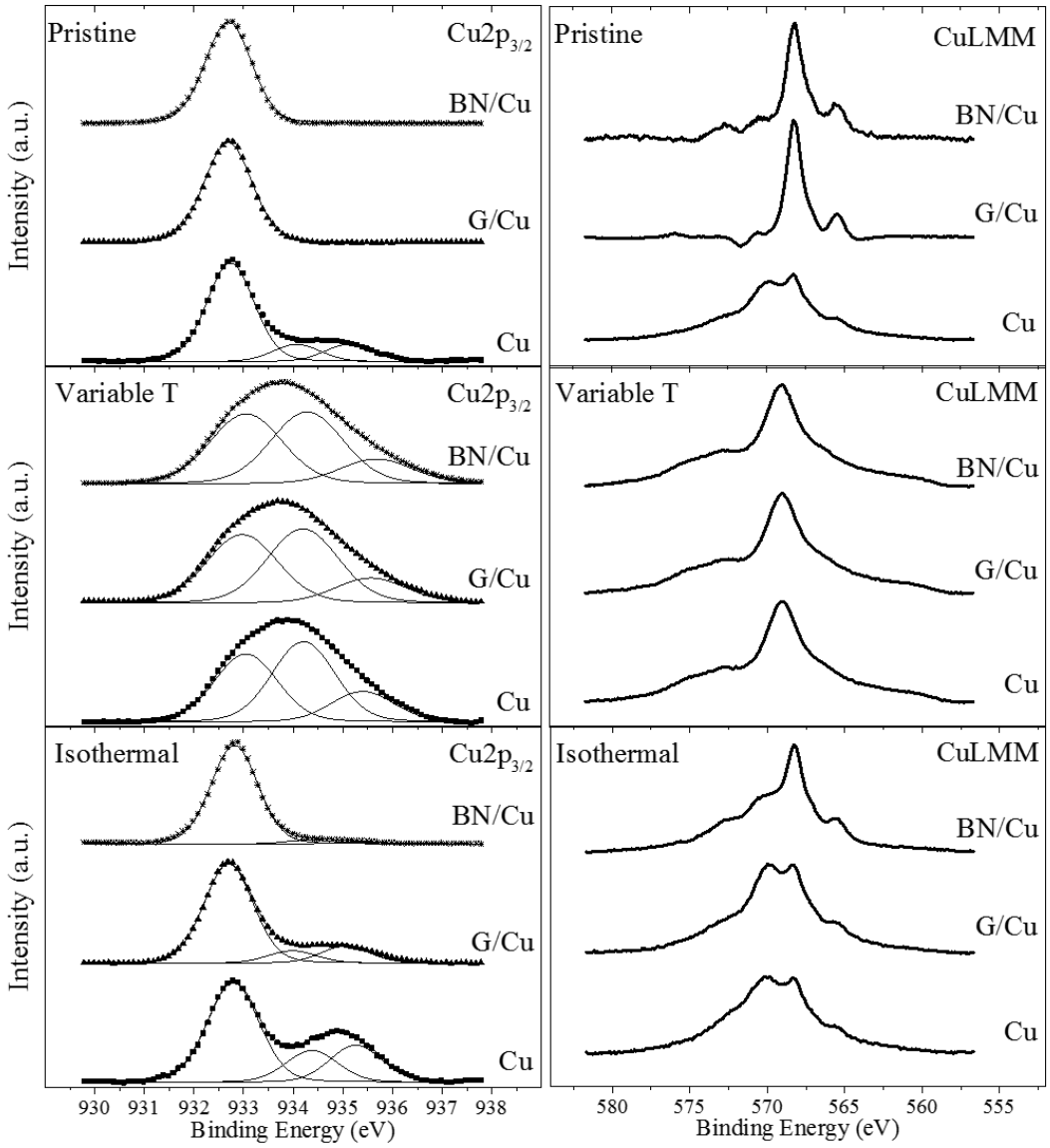

Figure 5.5: XPS (left) and XAES (right) spectra of untested samples, stepwise temperature tested samples and samples subjected to isothermal conditions for 60 hours. The small shift of all the peaks observed for the stepwise temperature experiment may be due to a slight charging of the surface, which in turn may witness the thicker oxide layer. *From publication 4.*

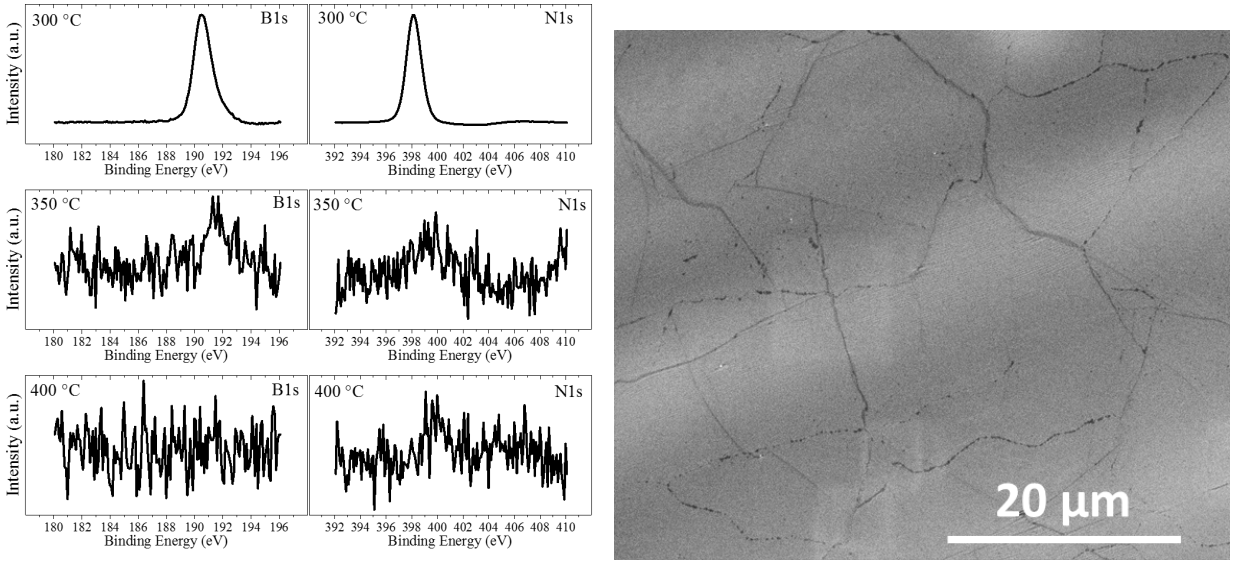

(a) (b)

Figure 5.6: (a) XPS-spectra of B1s and N1s obtained at 300 °C, 350 °C and 400 °C. While clear signatures of boron and nitrogen from the hBN-coating is seen at 300 °C, only a weak signal is seen at 350°C, and no clear signal is detected at 400 °C. (b) Graphene coating on copper annealed in air on hotplate to start oxidation through grain boundaries, making the graphene domain size visible. *From publication 4.*

being dominant. The hBN coated sample can barely be seen to be oxidised. Proceeding to the Auger spectra, a similar story can be told. Here, however, the pristine and the graphene-coated samples appear similarly oxidised, while only the hBN-coated sample has a clearly dominant metallic peak. The quantification of the results have been added to table 5.1.

In both the stepwise temperature experiment and the isothermal experiment the graphene-coating appears to be a more efficient barrier than the hBN-coating in the short term, showing less increase in the Raman signal of all oxide peaks. In both cases the trend reverses further into the experiment (250 °C and after approximately 9 hours respectively). This can be ascribed to the quality of the coatings; the average size of domains in the synthesized graphene was estimated to be approximately 20 µm, whereas the domain size of the hBN film is only a few µm. This is apparent from figure 5.6b, where the domain size is also visible by the oxidation initiated from the domain boundaries. The hBN has smaller domains, thus a larger boundary density and therefore initially a higher degree of oxidation will occur. However, in both coatings the build up of oxide will expand the crevices, and in the case of the graphene coating the galvanic coupling can take over, accelerating the corrosion (see section 2.5)[15]. On the other hand, hBN is not conducting, and will continue to protect

most of the surface.

Some of the largest synthesised single grains of graphene is in the order of millimetres[89], which in turn would significantly extend the protection offered from the coating. Larger hBN grains have been shown, but they are still orders of magnitude smaller than the ones presented of graphene. However, this does not remove the inherent issues of graphene, and such a coating will eventually fail, while the hBN coating will continue to protect the surface. Even if it should de-laminate or be damaged (as was seen after the stepwise temperature experiment at around 350 °C) it will not increase the corrosion rate.

Comparing the Raman data from the stepwise temperature experiment with the XPS-data obtained afterwards, a discrepancy can be observed; in the Raman a clear increase of both the cuprous oxide (Cu_2O) and the cupric oxide (CuO) is observed, while the XPS spectra mainly indicate much more cupric oxide. This can again be ascribed to the penetration depth of the instruments, where the XPS only probes the top atomic layers, while the Raman get information further within the sample (see corresponding sections in chapter 3). This could indicate that the topmost layers are further oxidised than those further into the sample, which is as expected[104].

In conclusion, the graphene-coating acted as a better barrier for oxidation protection in the short term at lower temperature, which was attributed to the inherently better quality of the film synthesised. However, at longer durations or at elevated temperatures (above 250 °C), no advantage was found using a graphene coating. The hBN-coating, on the other hand, offered significant protection at temperatures up to at least 300 °C and during longer tests. This is somewhat lower than the 750 °C measured by Li et al.[28], however, these measurement were exfoliated hBN on silicon dioxide. The quality of the produced film may have a large influence on the oxidation temperature, and moreover, the copper surface may also, as was the case with graphene, influence the stability of the thin hBN film.

Chapter 6

Multi-Layer Coatings

This chapter will cover corrosion testing of multi-layer (ML) graphene coatings. The following sections will cover the performance of the ML coatings in different media. Graphene-coated nickel electroplated on steel is tested in simulated seawater, which is one of the most common corrosion agents with a neutral pH. This is based on publication 1. The next section will cover graphene-coatings used in strong acidic media, where the impermeability of the coating gives rise to new challenges based on publication 2.

All the work in article 1 was performed by me, only with discussional input, and with the help from Accoat A/S with the Atlas cell test. In article 2 I contributed with discussion, writing, the graphene synthesis recipe, electron microscopy experiment and generally helped with characterization etc.. In publication 8 I mainly contributed with discussing ideas and with understanding the mechanisms at play.

6.1 Seawater - a pH Neutral Electrolyte

In article 1[76] we used type 304 stainless steel discs with a 2" diameter throughout the experiments. Electroplating was used to pre-coat the samples with nickel, and the "ACS_stdGonNi" recipe was used with the home-built CVD system described in section 3.1.1. The synthesized coatings had a moderate number of defects as seen from the Raman spectrum on figure 4.2b, indicated by the D/G peak intensity ratio of 0.19 ± 0.07. The 2D/G intensity ratio of 0.26 ± 0.01 is a result of the multiple layers of graphene[45]. Micro-Raman mapping resulted in almost identical spectra across the surface. A local map of the 2D/G intensity ratio reveal no large variation locally either as shown on figure 6.1a.

Using FIB milling a trench was cut in a sample, polished and subsequently studied using

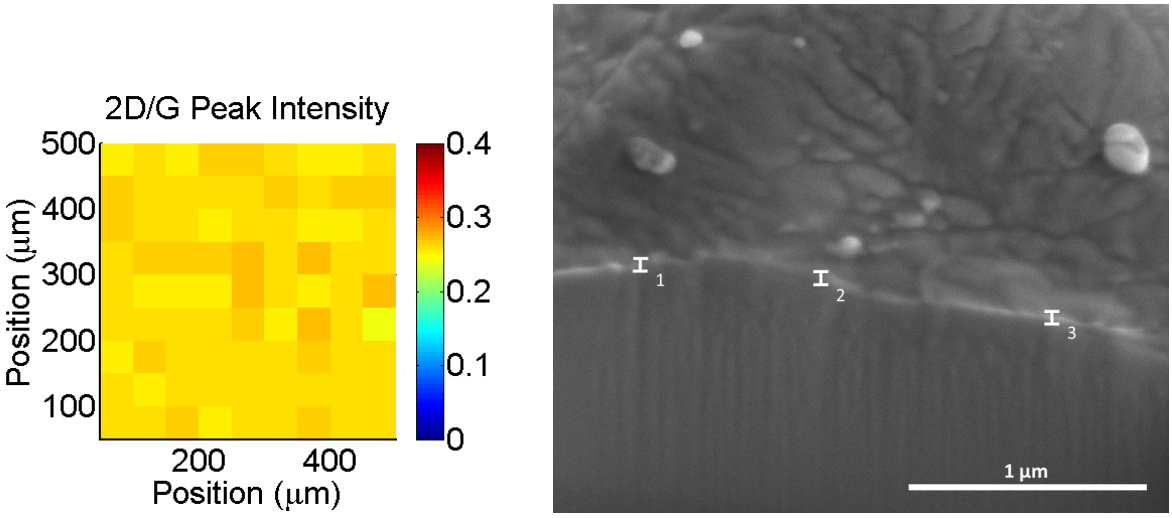

(a) (b)

Figure 6.1: (a) 2D/G intensity ratio map of part of the sample surface reveals that the coating is multi-layered in all inspected points and has little variation. (b) After using FIB milling to cut a trench in the sample, the coating thickness could be assess from SEM to be between 25 nm and 40 nm, corresponding to approximately 75-120 graphene layers.[76]

SEM. Here a rough estimate for the graphene coating thickness could be made. As can be seen on figure 6.1b, the thickness ranges roughly between 25 nm and 40 nm, corresponding to 75-120 layers. No unprotected areas were found using Raman spectroscopy, optical and SEM inspection.

Samples were tested in Atlas cells as described in section 3.8. Here coated and uncoated samples were tested pairwise in the same cell, to keep experimental conditions identical. A set of samples can be seen on figure 6.2. The graphene-coated sample can be seen to have areas that optically appear darker as seen on figure 6.1a.. These areas did, however, not result in variations in the Raman spectrum.

After 3 weeks where samples were halfway submerged in boiling simulated seawater (3.5 wt% NaCl), visible damage could be observed on the uncoated samples. The liquid-gas interface level is clearly visible, with significant colour changes in the gas phase, mostly towards green (corresponds to nickel(II)oxide or nickel(II)hydroxide), which could be due to the larger availability of oxygen. Moreover, some damage near the edge of the samples both in the gas and in the liquid phase can be seen.

After the tests, the graphene-coated samples were characterised using Raman spectroscopy. On figure 6.3a the averaged Raman spectra before and after the 3 week test are shown next to each other with the linewidth indicating the standard deviation. Here it is apparent

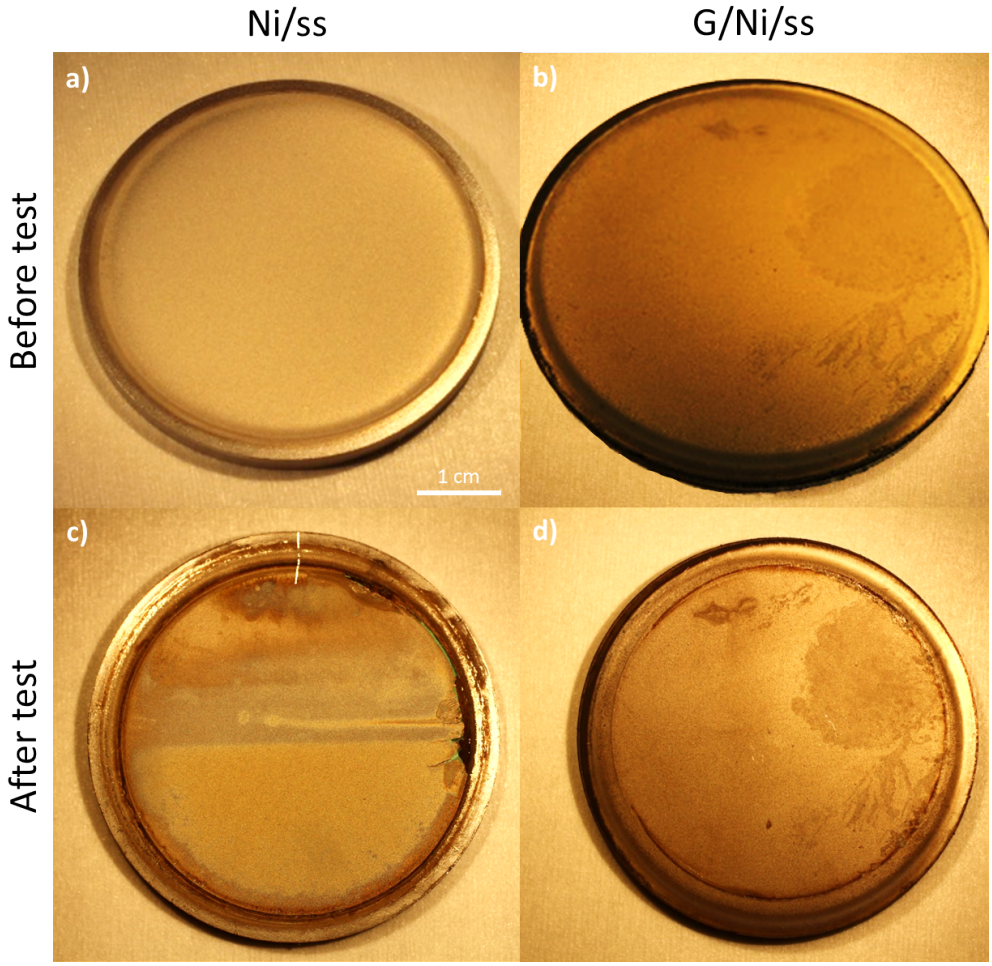

Figure 6.2: 2 inch steel samples with a layer of electroplated nickel (a) and with a multi-layer graphene coating (b). In (a) and (b) the pristine samples can be seen, while on (c) and (d) the samples after 3 week in boiling simulated seawater are shown[76].

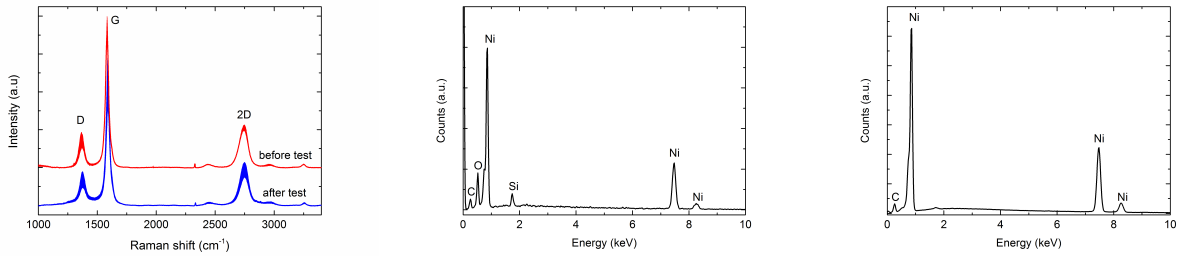

(a) (b) (c)

Figure 6.3: (a) Averaged Raman spectra of a sample before (red) and after (blue) 3 weeks of submersion into simulated seawater. The standard deviation is plotted as the width of the curves. The spectra are nearly identical[76]. (b) EDS-spectrum of a nickel coated sample after 3 weeks in an Atlas cell. Oxygen is clearly visible along with the nickel. (c) EDS-spectrum of the graphene and nickel coated sample after three weeks in the Atlas cell. Here oxygen is only present in very limited quantities. Both EDS-spectra were obtained with 15 kV acceleration voltage.

the the graphene coating is still intact. The D- to G-peak intensity ratio before the test was found to be 0.19 ± 0.07 while it was found to be 0.16 ± 0.04 after the test, thus unchanged within the measurement uncertainty.

As described previously, XPS is extremely surface sensitive, and thus not suited for probing through such a thick graphene coating, so EDS was utilized instead. On figure 6.3b the uncoated sample can be seen. Besides the relatively thick nickel layer, which obscures any signal from the steel underneath, an oxygen peak is clearly visible along with some carbon.

Due to the large penetration depth of the 15 keV incident electron beam, information from the graphene-nickel interface is available, and an EDS-spectrum obtained from the graphene coated sample can be seen on figure 6.3c. Here no clear oxygen peak can be seen.

Polarisation scans can be used to assess a corrosion rate of a system, however, as it is a destructive characterisation technique, it should normally not be used consecutive times. However, consecutive polarisation scans can be used as an extreme way of subjecting a candidate coating to corrosive stress, and can therefore be used as an alternative way of obtaining an indication of the corrosion resistance from a highly passivating coating. According to Pu et al.[105], it may even be used to simulate long-term tests. Besides the nickel coated (Ni/SS) and nickel coated sample with graphene grown on it (G/Ni/SS) the bare stainless steel disc was tested (SS). The data for G/Ni/SS produced by Pu et al. are also plotted for reference.

The testing of the samples were done using a platinum counter electrode, a silver/silver-chloride reference electrode, the Quick WE holder for the test samples (described in section

3.7.4) and the simulated seawater as electrolyte. 20 consecutive series consisting of OCP for stabilisation and a polarisation scan were conducted. On figure 6.4a and b the 1^{st} and the 20^{th} scan can be seen. The passivation layer formed on the stainless steel is clear in the first scan; its formation is marked by the red arrow and its breakdown by the blue arrow. However, after 20 scans a clear passivating layer is no longer formed while the corrosion current has increased and the corrosion potential decreased. It is also clear that the graphene produced by Pu et al. performs better than the graphene produced here, with a lower corrosion current. This can be explained by defects in our graphene film, as ions, such as Cl^- present in seawater, can diffuse through defects such as grain boundaries and cracks[16]. It should also be noted that the Ni/SS sample performed quite well, and indeed similarly to the graphene coated sample from Ref. 105.

After 20 scans the SS sample could be seen to be highly corroded, and the corrosion potential down-shifted by 166 mV attributed to the breakdown of the passivating metal oxide film. The Ni/SS and the G/Ni/SS from Ref. 105 performs very similarly, while the G/Ni/SS sample has a slightly higher corrosion current. However, the line shape did not change during the 20 scans, indicating a far better stability than that of the SS.

Figure 6.4c and d depict the I(D)/I(G) ratio of an area of the G/Ni/SS sample before and after 20 scans respectively. No quantitative difference can be seen before (I(D)/I(G) of 0.16 ± 0.01) and after (0.17 ± 0.02) the scans. As the I(D)/I(G) ratio is an indication on the density of lattice defects, this suggests that the graphene film is not damaged by the tests.

However, this method cannot definitively distinguish between the performance of the nickel and the graphene coating on top of it, and thus the method of accelerating corrosion with polarisation techniques should therefore not be used instead of a real long term test.

It was shown that graphene on nickel on stainless steel can protect a metal surface considerably better than a pure nickel coating in a heated seawater environment. Even defected graphene (as was seen from Raman spectroscopy and performance comparison with Ref. [105]) can effectively protect a surface in a wet environment. It can be argued that the reduction in corrosion current could be due to the increased diffusion length of non-overlapping defects, where the diffusion between the layers considerably increased the total diffusion path, and thus by limiting diffusion reduce the transport of corrosive species. This is in contrast to the mechanism in single layer graphene where a small defect may lead to a large diffusion, as the path length is extremely small and thus the hydraulic resistance similarly small[106]. A schematic illustration can be seen on figure 6.5.

It was also seen that the contribution of the nickel seed layer cannot be neglected in polarisation experiments when protecting stainless steel.

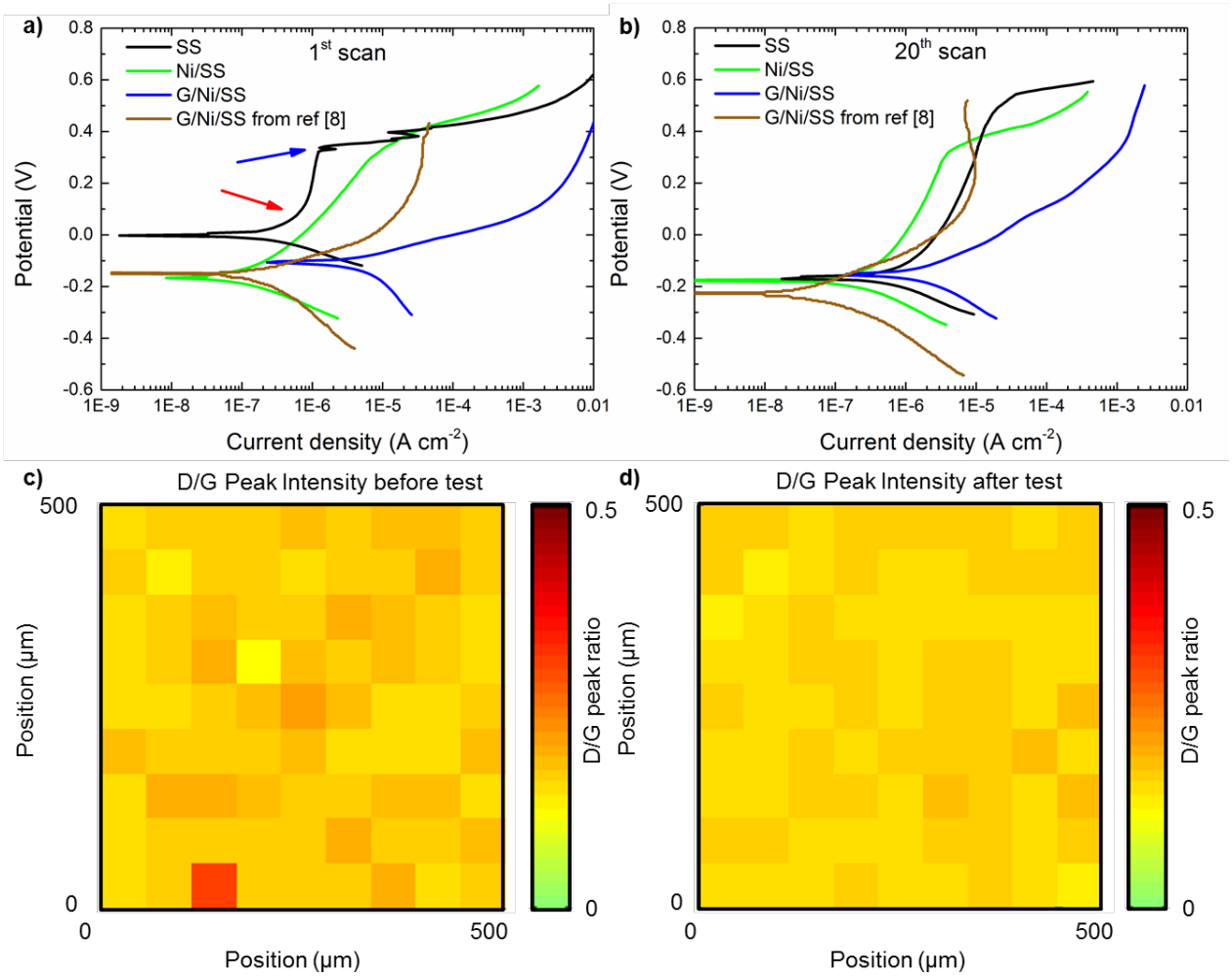

Figure 6.4: 1st (a) and 20th (b) polarisation scan of a stainless steel sample (SS), nickel coated stainless steel sample (Ni/SS), nickel coated stainless steel sample with graphene synthesised on top (G/Ni/SS) and a similar sample from [105]. Spatial Raman map of the D/G intensity ratio can be seen on (c) before testing, and on (d) after testing, revealing the defect distribution[76].

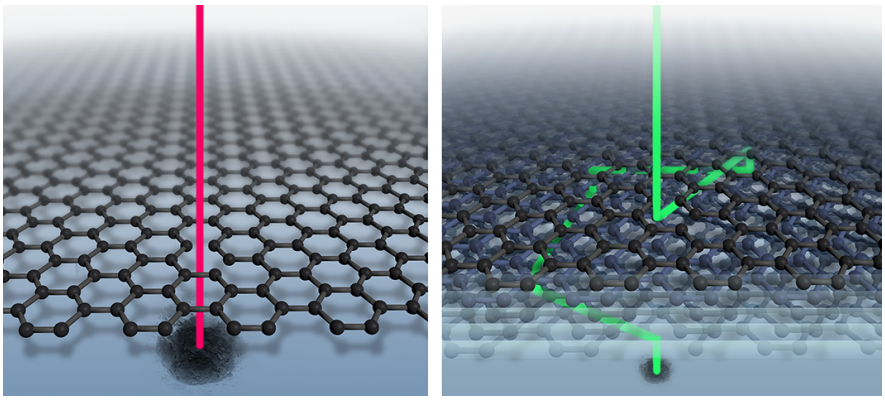

Figure 6.5: Rendering of single layer graphene protecting a surface. Vacancy defects can result in species penetrating the coating. On the right a similar system with ML graphene film protecting the surface can be seen. Unless the defects in the different layers are perfectly aligned, the total diffusion pathway can be dramatically increased in multi-layer graphene films, even in case of a high defect density[76].

6.2 Acidic Media

While protection against seawater and other pH neutral environments is highly important, an impermeable coating could possibly also be used in acidic media where fewer alternatives exist. This section describes the work described in publication 2, where multilayer graphene coatings were tested in strong acidic environments.

Samples were prepared using the "APCVD" recipe (described in section 4.1.2) on 25 µm thick nickel foils (from Alfa Aesar) as shown on figure 4.4. Using a 3 electrode setup, a polarisation scan of the sample was performed in a 0.5 M HCl solution (pH = 0.3) as can be seen on figure 6.6a. A slight lowering of the corrosion potential was observed (25 mV), however, the reduction of the corrosion current compared with the uncoated nickel sample indicated an improvement of the protection provided ($I_{corr,Ni}$ = 21 µA/cm^2 and $I_{corr,MLG}$ = 9 µA/cm^2). Using equation 3.1, this translates to corrosion rates of CR_{Ni} = 226 µm/year and CR_{MLG} = 97 µm/year. Similarly, EIS-measurements of the graphene coated samples only displayed a 1.7 times improvement of the charge transfer resistance over the uncoated ones. A small improvement taking the quality and thickness of the graphene film into account. On figure 6.6b the rapid bubble formation in the most negative part of the polarisation scan can be seen through the side of a glass beaker. Hydrogen bubbles are formed at negative potentials[107] through the reduction reaction

$$2\,H_3O^+(aq) + 2\,e^- \rightarrow H_2(g) + 2\,H_2O(aq) \tag{6.1}$$

To investigate whether the bubbles were formed on the surface of the coating, in between coating layers or in the interface between the coating and the substrate, SEM was performed after the potentiodynamic scan, and the obtained results are visible on figure 6.6c. Here part of the MLG film is clearly delaminated. The orientation of the edges of the delaminated area are bended outwards indicating an burst-like delamination stemming form the interface. The insert shows a close up of the edge of this area, where the torn MLG film can be seen.

Applying a constant potential of -0.6 V for 3 minutes before inserting a sample into the SEM reveals the initiation of bubble formation. On figure 6.6d two bubbles can be seen under the graphene film. The wrinkles in the film are unfolded near the centre of the bubbles. Moreover, it should be noted that the bubbles are not emptied by the vacuum of the SEM, and the graphene film seems hydrogen tight, which could indicate a behaviour similar to the one observed by Bunch et al. for single layer membranes[12]. Keeping the -0.6 V potential for longer results in continuous bubble formation and eventually rupture of the film. To confirm that no graphene was left in these areas, and bubbles did not form between the layers, Raman spectroscopy was employed. No graphene related peaks were detected in the areas where bubbles had burst.

To further investigate the bubble formation, droplets of HCl were placed on MLG-coated samples under an optical microscope. After 2 hours the bubbles can reach sizes of up to approximately 100 µm in diameter, as can be seen on figure 6.7. At the perimeter of the bubbles radial lines show a buckling pattern the resembles trapped gas under a membrane[109].

In figure 6.7b, the HCl droplet has been removed and the dried area underneath is investigated. Here some folded regions appear that were not present prior to introducing the hydrochloric acid droplet, two of which have been marked using red circles.These could be burst hydrogen bubbles. Other, smaller bubbles may still be inflated. On figure 6.7c, an area outside where the HCl droplet was placed is investigated. Here circular areas have undergone a clear colour change. The colours observed could be due to nickel oxidation. However, this is not normally observed for nickel in contact with air, and is not seen on neither MLG-coated samples in air or uncoated samples introduced to a droplet of HCl.

To further investigate bubble formation another experiment was conducted. Here a droplet of 0.5 M HCl was placed on a sample and then immediately removed with a tissue. Without any blow-drying or further cleaning, the sample was loaded directly into a FEI Helios SEM. In this way, bubble formation could be monitored, as the bubbles had not formed before the experiment started. As this effect is not observed only inserting a graphene-coated nickel foil into the SEM, the bubble formation was ascribed to the HCl left on the sample surface. Curiously, bubble formation only occurred during irradiation of the

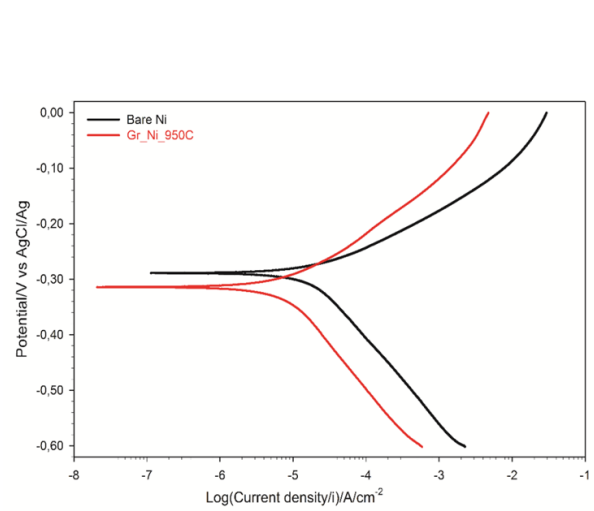

(a)

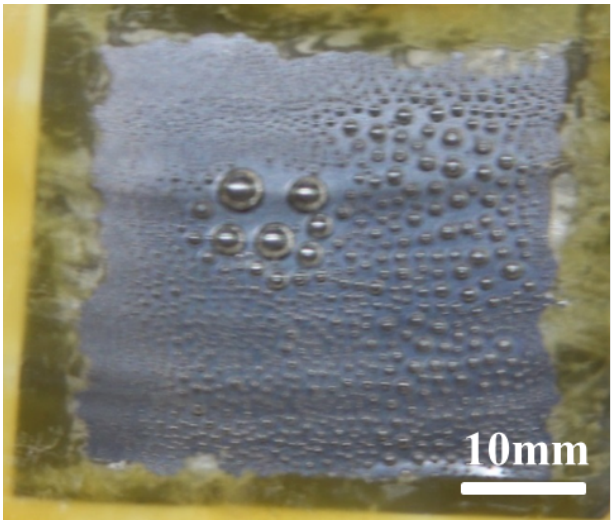

(b)

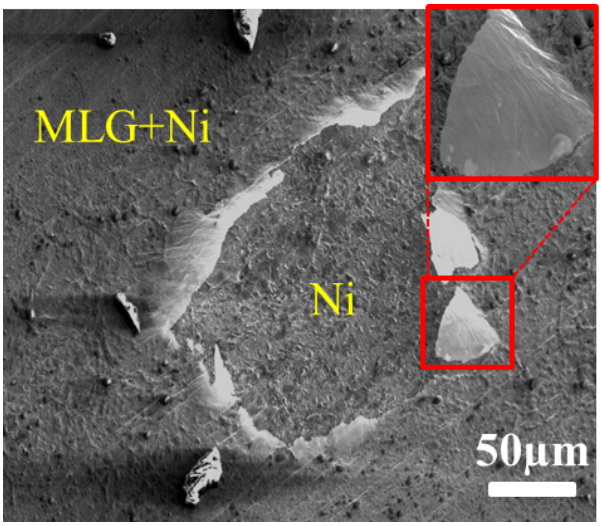

(c)

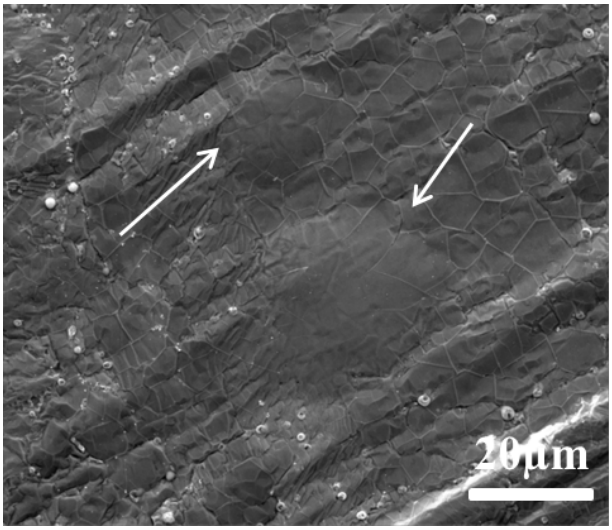

(d)

Figure 6.6: (a) Potentiodynamic scan from −300 mV to 300 mV vs OCP of the uncoated nickel sample and a MLG coated sample. The corrosion potential of −290 mV for bare nickel and −315 mV for MLG-coated nickel can be read of the graph. Scan rate: 0.5 mV/s. (b) Image of MLG-coated nickel foil during potentiodynamic scan. Here hydrogen bubble formation is apparent. (c) SEM micrograph of MLG-coating on nickel foil after a potentiodynamic scan. Here a piece of the graphene coating has been delaminated from the nickel surface. The sides of the delaminated area are bent outwards, which suggest that the rupture was caused by an overpressure bubble underneath the coating. Insert makes the delamination clear. (d) SEM micrograph of two bubbles not yet burst after 3 minutes of −0.6 V vs Ag/AgCl counter electrode[108].

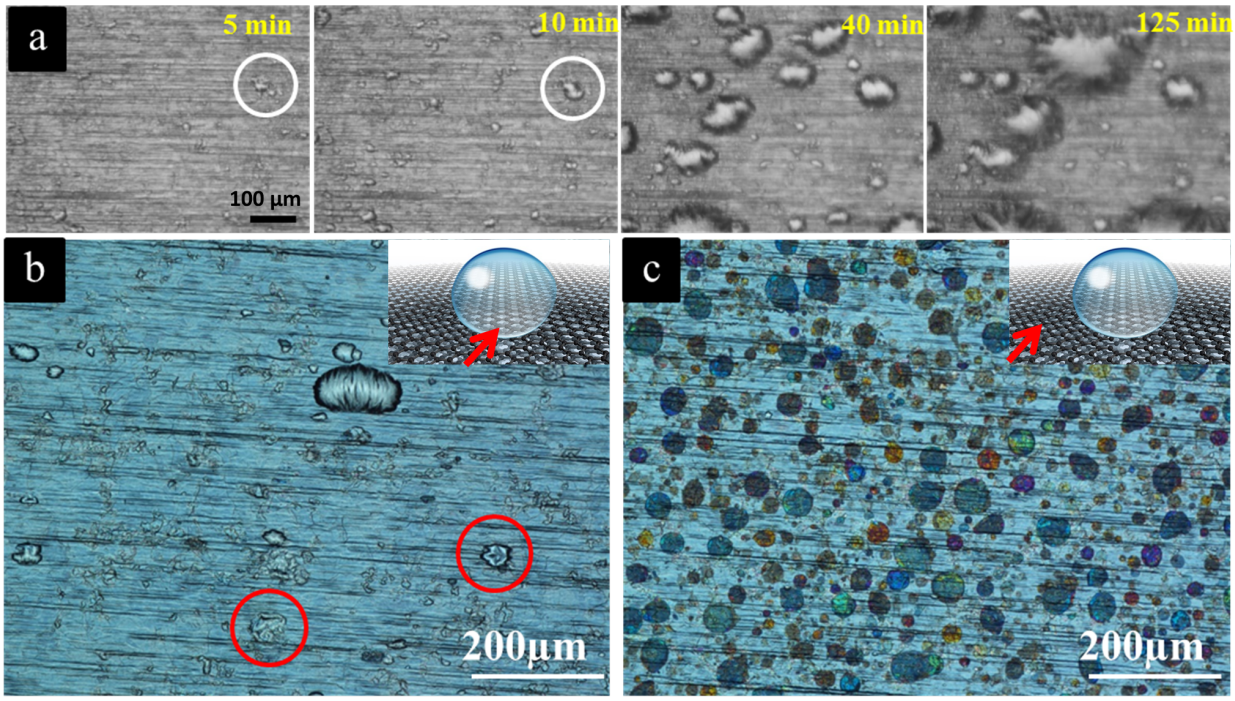

Figure 6.7: (a) Time evolution of bubble formation at zero potential under an optical microscope. The images where acquired through the bubble and they all share the same scale bar of 100 µm. After removing the droplets higher quality images could be obtained and (b) shows an area where bubbles had evolved (two residues after such bubbles marked in red). (c) shows an area away from the bubble on the same sample. Here the colour changes indicate oxidation of the nickel surface[108].

electron beam, as can be seen on figure 6.8. There are 2.5 s between each frame shown here. First an area with no apparent bubbles can be seen. Increasing the magnification, and thus concentrating the electron beam in a smaller area, resulted in bubble formation, which was easily observed by subsequently decreasing the magnification again. The last four frames are held at the same magnification, and further bubbles can be seen to be formed. It is noteworthy to remark, that the bubbles did not seem to deflate again, which indicates that the bubbles remain stable, despite the comparably shorter time of inflation. This shows that the question of permeability is not a simple one to answer.

Outside the SEM, bubbles could reach a size easily visible with the naked eye (during several hours exposure to acid). Bursting such a bubble resulted in no visible substance escaping the bubble, which support the hypothesis that the bubbles are filled with hydrogen.

As the experiment in the SEM was conducted in vacuum (10^{-5} mbar-range), the risk that contaminants other than those introduced on purpose affects the experiment is very limited. The bubble formation is sped up dramatically by the electron beam exposure, to a rate that cannot be explained by transport of species not already present locally on the surface. The atmosphere inside the microscope consists nearly exclusively of nitrogen, which does not easily dissociate at room temperature. A one-way transport of nitrogen in through the graphene membrane seems highly unlikely, as the pressure generated by the adhesion of the graphene membrane works to empty the bubble, not fill it. This leaved hydrogen gas as the prime candidate for bubble formation.

The triggering by electron irradiation is itself puzzling. One possible explanation could be that local heating by the electron beam could accelerate water diffusion through defect channels in the graphene coating. As 0.5 M HCl has a pH of 0.3, a large amount of aqueous protons would be present in the water. Reaching the surface of the nickel, hydrogen evolution would take place, increasing the pH locally. Diffusion would call for further aqueous protons, which could be transported via a Grotthuss mechanism[110]. The process is schematically illustrated on figure 6.9, where an initial defect channel filled with water is illustrated. As more protons combine with electrons at the nickel-surface, more hydrogen is evolved, eventually resulting in delamination of the graphene film. The hydrogen evolution reaction (equation 6.1) requires excess electrons. These are easily available from the electron beam bombardment in the SEM, further accelerating the reaction. However, in the experiment with a droplet of HCl under the optical microscope, the sample is an electrically isolated system. This explains the area outside the bubble where the not normally occurring oxidation of the nickel surface can be seen (figure 6.7). This effect was not observed using just nickel foil. Here the conducting nature of graphene might be at play, both acting as a

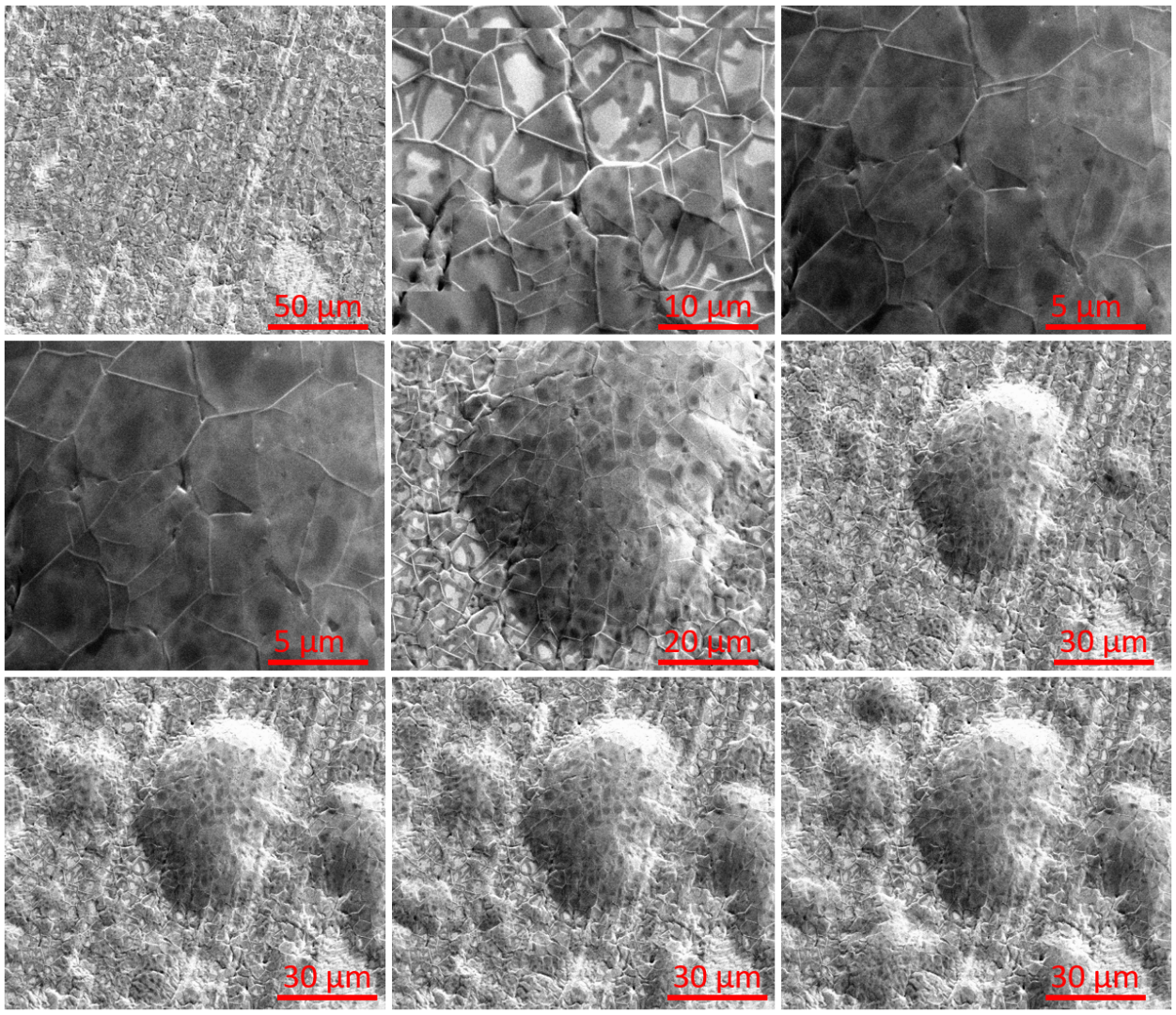

Figure 6.8: SEM-inflation of bubbles in the graphene-nickel interface. Nickel is inserted into the FEI Helios SEM with tiny amount of HCl. A zoom in concentrates the electron beam, accelerating bubble formation. Time between each micrograph is 2.5 s.

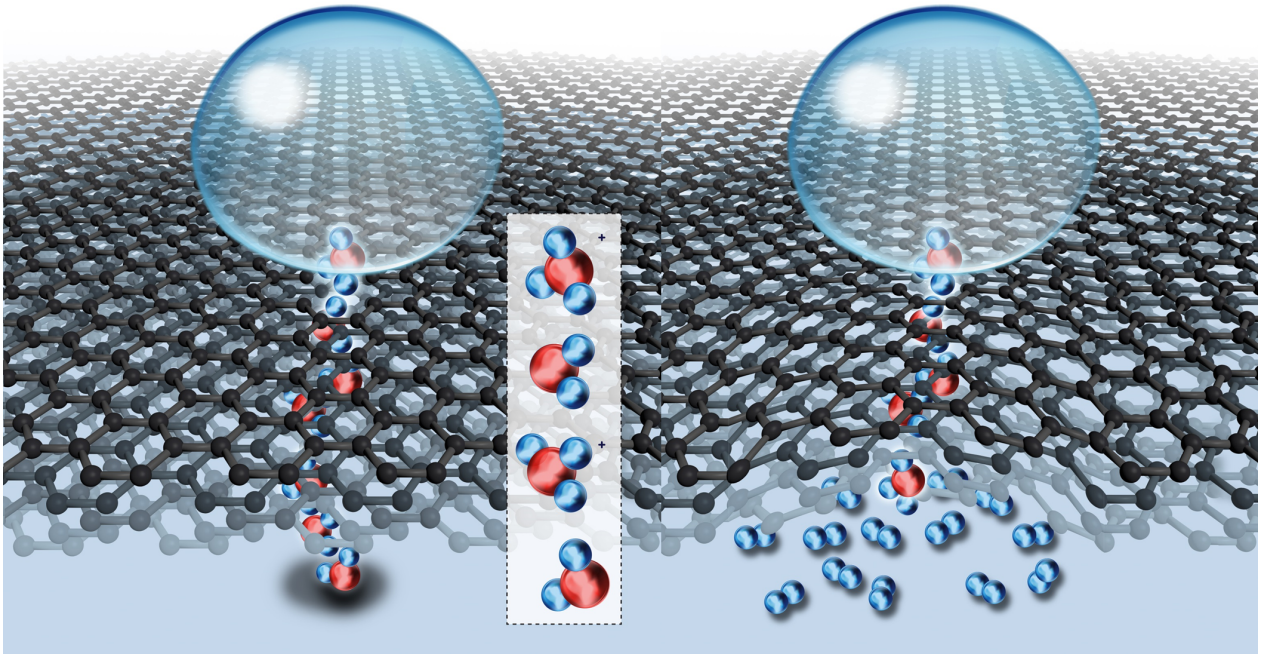

Figure 6.9: Schematic illustration of the process of bubble formation. The aqueous protons can be transported, for instance via a Grotthuss mechanism, through defects in the graphene coating and reach the metal surface. Here hydrogen evolution is favourable to take place at the low pH and hydrogen can built up in the interface, delaminating the graphene. The hydrogen escape rate is lower than the evolution rate, as channels from the interface are blocked by water molecules.

local cathode, withdrawing electrons from the nickel, but furthermore as a good conductor, easily transporting electrons from the oxidised parts to the site of the hydrogen evolution.

To further confirm that it is hydrogen that is evolved by the reduction reaction described in equation 6.1 even at no applied potential, and that the chlorine is not involved in the process, other experiments were conducted. Droplets of H_2SO_4 and HNO_3 were also tested. As shown in figure 6.10, even though the shape and formation speed of the bubbles are not identical, all three 0.5 M acids resulted in bubble formation on nickel foils, which is to be expected from the Pourbaix diagram of nickel[111].

It was seen that even high quality multi-layer graphene may fail as a viable coating on nickel surfaces in strong acidic environments, as protons can pass through, commence hydrogen evolution and efficiently delaminate the graphene film. This is not solely a problem for nickel, but for a whole range of metals, where spontaneous hydrogen evolution will occur at low pH values[112]. This includes all the metals with negative standard potential. The graphene coating might even hinder formation of a passivating layer, so metals such as Cr

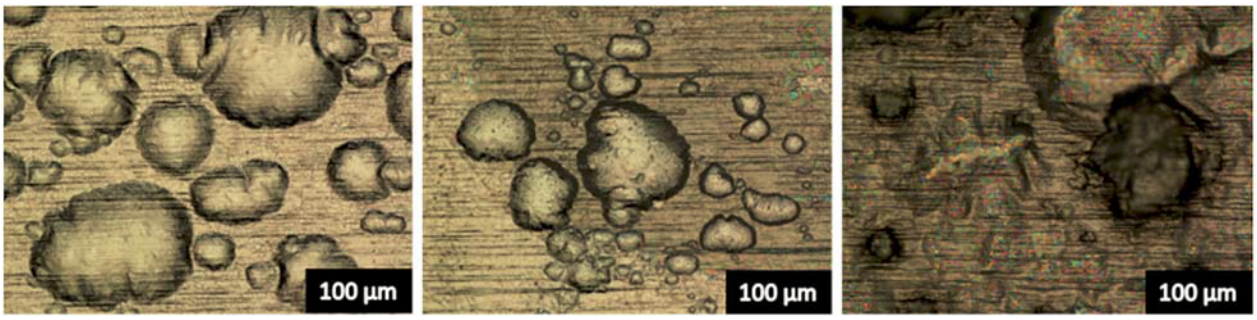

Figure 6.10: MLG coated nickel film using the APCVD recipe after 4 hours exposure to (left) 0.5M hydrochloric acid, (middle) 0.5M sulphuric acid and (right) 0.5 M nitric acid. All three acids gave rise to bubble formation in the graphene/nickel interface.[108]

can also give rise to hydrogen evolution at the interface. Other common susceptible metals include Fe, Mg, Al and Ti[112].

However, later Zhou et al. published a theoretical study, wherein they explain that the confined space under the graphene coating on nickel surfaces enhances the hydrogen evolution rate, making nickel as effective a catalyst as platinum [113]. The problem of hydrogen evolution delaminating the coating should therefore be most pronounced on nickel. However, as first mentioned in Ref. 108 and later in Ref. 113 this might instead lead to faster and cheaper hydrogen evolution reactions.

As an alternative to simply using MLG coatings, other materials can be included to create a composite. One concept includes transferring graphene on polymers, making a sandwich structure where high quality graphene aligned parallel to the surface and separated by polymers protect the surface. A patent application have been submitted, but the data is not presented in this thesis (publication 8).

Chapter 7

Conclusion and Perspectives

This chapter will conclude on the work conducted with graphene, single and multi-layered, and hBN coatings, and try to give perspectives on how the society can benefit from this knowledge. Here the possible uses of the different coating technologies based on 2D materials will be discussed, and moreover, other uses of the technologies developed will be given as well.

This thesis has presented the main results of the PhD-project about "Protective coatings based on 2D-materials". Here the key goal was to fabricate and utilize 2D-materials for protective purposes in a scalable way. More specifically, how to circumvent the galvanic coupling arisen by combining graphene and most metals. Testing of such systems were to take place in saline and even harsher environments. Moreover, a comparison of graphene and another 2D-material, hexagonal boron nitride, was done for oxidation protection.

In chapter 2 fundamental properties of especially graphene, and also hexagonal boron nitride, was given.

In chapter 3 the experimental setups used for the synthesis of graphene were described. Here the special properties of these systems were given, and the importance of having a controlled atmosphere was shown. Also, the main characterisation techniques used throughout the thesis were described, including, where applicable, the specifics necessary to understand the 2D-materials investigated. *The Quick Working Electrode invention led to a patent which was subsequently commercialised (publication 6).*

In chapter 4 the actual synthesis of primarily graphene, single and multilayered, but also hexagonal boron nitride was described. *One of these methods, the synthesis of hexagonal boron nitride from an infrared active precursor molecule in a rapid thermal chemical vapour deposition system, was presented and the intellectual property protected (publication 7).*

In chapter 5 single layer coatings of both graphene and hexagonal boron nitride were synthesized on a copper surface to compare the oxidative barrier properties. The evolution of copper oxides was monitored live using Raman spectroscopy, and the graphene layers were found to offer a better protection in the short term, which was explained by the larger grain size. In the long term, however, no improvement using the graphene film was seen compared to the unprotected copper. Hexagonal boron nitride films, on the other hand, showed a stable protection even at longer duration. The hexagonal boron nitride also outperformed the graphene at higher temperatures. *A manuscript based on this work is under review in Scientific Reports (publication 4).*

In chapter 6 multi-layer graphene coatings were tested. First, such coatings were synthesised on nickel-electroplated steel for protection against saline environment. The Atlas cell is a harsh, accelerated corrosion test, which despite Nickels already excellent corrosion resistant properties, induces extensive damage to the surface of unprotected nickel films. The long term stability was explained by a low diffusion rate. Diffusion through multiple partially damaged layers, where the diffusion length is increased by the damage/perforations to occur in a non-overlapping manner was deemed to be rate limiting. *These finding were published in Journal of Power Sources (publication 1).* A similar multilayer graphene coating with a lower amount of visible as well as intrinsic defects, was tested in strong acidic media. The gas-tight coating did not allow hydrogen to escape, resulting in blisters, bubbles and eventually delamination of the graphene. It was inferred that protons reaching the nickel surface under the coating combined with electrons and evolved hydrogen. This was found as a major weakness of such graphene coatings, however, this attribute might be utilized for hydrogen gas production. *These findings were published in RCS Advances in publication 2. Another patent application was submitted based on stacking of polymer and graphene layers for a galvanic-decoupled diffusion barrier coating in publication 8.*

The results of this PhD-project have confirmed the pitfalls of using single layer graphene coatings, but have shown a viable route for multi-layers coatings, where diffusion limitations outbalance the galvanic coupling that may arise between the noble graphene and the less noble metals. It is, however, important to take into account the media in which the coatings are to be used, as strong acidic media was found to give rise to hydrogen bubbles in the metal (nickel)/graphene interface. The tightness of the coating was here found to be a surprising potential disadvantage, as the gas built-up will eventually delaminate the coating. However, this type of behaviour might be relevant for hydrogen production, in that element separation takes place without external potentials.

Hexagonal boron nitride has been demonstrated not to have the pitfalls of single layer

graphene, in both short- and long-term tests for oxidation protection. Graphene films synthesised in this project are based on the common and in-expensive precursors methane and acetylene, while the hexagonal boron nitride films are based on the much more expensive borazine molecules. Even though only tiny amounts of precursor gas is used for the single layer coatings, it must be taken into account when choosing a coating technology for a specific application. However, a whole range of 2D-materials exists, whereof some may have similar barrier properties but be less expensive to produce. The huge attention on such materials may lead to the discovery of another 2D-material as a coating candidate.

An issue that should be further addressed is the synthesis temperature. The defect density of graphene coatings were clearly seen to be related to the temperature. This might not be an issues for metals such as nickel, but alloys such as steel may change their properties at a much lower threshold temperature. Coatings directly synthesised on a surface is so far limited to substrates that can withstand high temperatures. However, we have preliminary results from a collaboration with the University of Aarhus, using a more complex precursor molecule, revealing a promising route for low temperature direct synthesis of coatings.

Instead of choosing a graphene coating, that is conductive but gives rise to galvanic couples, or a hBN coating, that is insulating, a hybrid can be synthesised. The similar lattice parameters of the two materials allows for in-plane hetero-structures, where properties can be tailored. An in-plane system of graphene quantum dots in hexagonal boron nitride or BCN (a boron nitride/graphene hybrid), could be synthesized directly on a surface. In this way one could imagine not only applying a coating for protective purposes, but one that at the same time was made e.g. photo-luminescent.

We have synthesised such a system under UHV-conditions, and the findings are under review by Nature Communications (publication 3).

Indirect synthesis and chemical exfoliation may have a broader scope. By synthesising the coatings at high temperatures on one surface and afterwards transferring them to the substrate to be protected, heating up the substrate above critical temperatures can be avoided. Some advantages will be lost, as the coating will neither be as thin as the directly synthesised coating nor naturally conform to the surface. *Publication 8 is a patent application of the intellectual property based on such a transferred coating[114].*

There are still many challenges to solve before coatings based on graphene and other 2D-materials are ready for full scale industrial implementation. Directly synthesised coating have a great potential, but major issues needs to be solved; galvanic couples can form between graphene and the metal to be protected, delamination from substrate surfaces and the high synthesis temperatures needed for high quality graphene, which can damage the

substrate itself. Galvanic corrosion was limited using multi-layer coatings and circumvented using insulating alternatives such as hBN, however, even though neutral electrolyte tests did not result in delamination issues, strong acidic environments provided an unexpected delamination mechanism where the impermeability of multi-layer graphene played an undesired role. Adding binders, and chemically functionalizing graphene may be a viable route for increasing graphene adhesion. Lowering of the synthesis temperatures will generally lead to a decrease of the coating quality, however, recent progress have been made with more complex precursor molecules, which could enable low temperature synthesis - even without nickel seeding layers. Another possibility is rapid flash synthesis, where the capabilities of the RT-CVD system is utilised for short high energy pulses heating the substrate surface to allow graphene formation. Pauses in between pulses can possibly avoid higher temperatures in the bulk.

Ultimately, the demonstrated advances may contribute to new applications where coatings can be applied or cases where traditional coatings can be replaced for improved protection, reducing the negative impact of corrosion on both durability and costs.

Bibliography

[1] A. El-Meligi, "Corrosion preventive strategies as a crucial need for decreasing environmental pollution and saving economics," *Recent Patents on Corrosion Science*, 2010.

[2] R. K. Singh Raman and A. Tiwari, "Graphene: The thinnest known coating for corrosion protection," *JOM*, vol. 66, no. 4, pp. 637–642, 2014. [Online]. Available: http://dx.doi.org/10.1007/s11837-014-0921-3

[3] M. Lilly, S. Ihekwoaba, S. Ogaji, and S. Probert, "Prolonging the lives of buried crude-oil and natural-gas pipelines by cathodic protection," *Applied Energy*, vol. 84, no. 9, pp. 958 – 970, 2007. [Online]. Available: http://www.sciencedirect.com/science/article/pii/S0306261907000220

[4] S. Xia, Y. Gao, A. Bower, L. Lev, and Y.-T. Cheng, "Delamination mechanism maps for a strong elastic coating on an elastic-plastic substrate subjected to contact loading," *International Journal of Solids and Structures*, vol. 44, no. 11-12, pp. 3685–3699, 2007. [Online]. Available: http://www.sciencedirect.com/science/article/pii/S002076830600415X

[5] G. H. Koch, M. P. Brongers, N. G. Thompson, Y. P. Virmani, and J. H. Payer, "Corrosion cost and preventive strategies in the united states," The National Academies of Sciences, Engineering, and Medicine, National Technical Information Service 5301 Shawnee Road Alexandria, VA 22312 USA, Tech. Rep., apr 2002. [Online]. Available: https://trid.trb.org/view.aspx?id=707382

[6] S. Chen, L. Brown, M. Levendorf, W. Cai, S.-Y. Ju, J. Edgeworth, X. Li, C. W. Magnuson, A. Velamakanni, R. D. Piner, J. Kang, J. Park, and R. S. Ruoff, "Oxidation resistance of graphene-coated cu and cu/ni alloy," *ACS Nano*, vol. 5, no. 2, pp. 1321–1327, 2011.

[7] N. Kirkland, T. Schiller, N. Medhekar, and N. Birbilis, "Exploring graphene as a corrosion protection barrier," *Corrosion Science*, vol. 56, pp. 1 – 4, 2012. [Online]. Available: http://www.sciencedirect.com/science/article/pii/S0010938X11006421

[8] D. Prasai, J. C. Tuberquia, R. R. Harl, G. K. Jennings, and K. I. Bolotin, "Graphene: Corrosion-inhibiting coating," *ACS Nano*, vol. 6, no. 2, pp. 1102–1108, 2012.

[9] M. Topsakal, H. Sahin, and S. Ciraci, "Graphene coatings: An efficient protection from oxidation," *Physical Review B*, vol. 85, no. 15, p. 155445, 2012.

[10] K. S. Novoselov, A. K. Geim, S. V. Morozov, D. Jiang, Y. Zhang, S. V. Dubonos, I. V. Grigorieva, and A. A. Firsov, "Electric field effect in atomically thin carbon films," *Science*, vol. 306, pp. 666–669, 2004.

[11] K. S. Novoselov and A. K. Geim, "The rise of graphene," *Nat Mater*, vol. 5, no. 3, pp. 183–191, 2007.

[12] J. S. Bunch, S. S. Verbridge, J. S. Alden, A. M. van der Zande, J. M. Parpia, H. G. Craighead, and P. L. McEuen, "Impermeable atomic membranes from graphene sheets," *Nano Letters*, vol. 8, no. 8, pp. 2458–2462, 2008.

[13] Z. Chen, W. Ren, L. Gao, B. Liu, S. Pei, and H.-M. Cheng, "Three-dimensional flexible and conductive interconnected graphene networks grown by chemical vapour deposition," *Nat Mater*, vol. 10, no. 6, pp. 424–428, Jun. 2011. [Online]. Available: http://dx.doi.org/10.1038/nmat3001

[14] H. Y. Nan, Z. H. Ni, J. Wang, Z. Zafar, Z. X. Shi, and Y. Y. Wang, "The thermal stability of graphene in air investigated by raman spectroscopy," *Journal of Raman Spectroscopy*, vol. 44, no. 7, pp. 1018–1021, 2013. [Online]. Available: http://dx.doi.org/10.1002/jrs.4312

[15] M. Schriver, W. Regan, W. J. Gannett, A. M. Zaniewski, M. F. Crommie, and A. Zettl, "Graphene as a long-term metal oxidation barrier: Worse than nothing," *ACS Nano*, vol. 7, no. 7, pp. 5763–5768, 2013.

[16] Y.-P. Hsieh, M. Hofmann, K.-W. Chang, J. G. Jhu, Y.-Y. Li, K. Y. Chen, C. C. Yang, W.-S. Chang, and L.-C. Chen, "Complete corrosion inhibition through graphene defect passivation," *ACS Nano*, vol. 8, no. 1, pp. 443–448, 2014.

[17] X. Li, W. Cai, J. An, S. Kim, J. Nah, D. Yang, R. Piner, A. Velamakanni, I. Jung, E. Tutuc, S. K. Banerjee, L. Colombo, and R. S. Ruoff, "Large-area synthesis of high-quality and uniform graphene films on copper foils," *Science*, vol. 324, no. 5932, pp. 1312–1314, 2009. [Online]. Available: http://science.sciencemag.org/content/324/5932/1312

[18] S. Bae, H. Kim, Y. Lee, X. Xu, J.-S. Park, Y. Zheng, J. Balakrishnan, T. Lei, H. Ri Kim, Y. I. Song, Y.-J. Kim, K. S. Kim, B. Ozyilmaz, J.-H. Ahn, B. H. Hong, and S. Iijima, "Roll-to-roll production of 30-inch graphene films for transparent electrodes," *Nat Nano*, vol. 5, no. 8, pp. 574–578, Aug. 2010. [Online]. Available: http://dx.doi.org/10.1038/nnano.2010.132

[19] K. S. Novoselov, V. I. Fal'ko, L. Colombo, P. R. Gellert, M. G. Schwab, and K. Kim, "A roadmap for graphene," *Nature*, vol. 490, no. 7419, pp. 192–200, Oct. 2012. [Online]. Available: http://dx.doi.org/10.1038/nature11458

[20] J. H. Los, K. V. Zakharchenko, M. I. Katsnelson, and A. Fasolino, "Melting temperature of graphene," *Phys. Rev. B*, vol. 91, p. 045415, Jan 2015. [Online]. Available: http://link.aps.org/doi/10.1103/PhysRevB.91.045415

[21] L. Liu, S. Ryu, M. R. Tomasik, E. Stolyarova, N. Jung, M. S. Hybertsen, M. L. Steigerwald, L. E. Brus, and G. W. Flynn, "Graphene oxidation: Thickness-dependent etching and strong chemical doping," *Nano Lett.*, vol. 8, no. 7, pp. 1965–1970, Jul. 2008. [Online]. Available: http://dx.doi.org/10.1021/nl0808684

[22] F. Bundy, "Pressure-temperature phase diagram of elemental carbon," *Physica A: Statistical Mechanics and its Applications*, vol. 156, no. 1, pp. 169 – 178, 1989. [Online]. Available: http://www.sciencedirect.com/science/article/pii/0378437189901155

[23] A. K. Geim, "Graphene: Status and prospects," *Science*, vol. 324, no. 5934, pp. 1530–1534, 2009. [Online]. Available: http://science.sciencemag.org/content/324/5934/1530

[24] D. C. Elias, R. R. Nair, T. M. G. Mohiuddin, S. V. Morozov, P. Blake, M. P. Halsall, A. C. Ferrari, D. W. Boukhvalov, M. I. Katsnelson, A. K. Geim, and K. S. Novoselov, "Control of graphene's properties by reversible hydrogenation: Evidence for graphane," *Science*, vol. 323, no. 5914, pp. 610–613, 2009. [Online]. Available: http://science.sciencemag.org/content/323/5914/610

[25] W. S. Hummers and R. E. Offeman, "Preparation of graphitic oxide," *Journal of the American Chemical Society*, vol. 80, no. 6, pp. 1339–1339, 1958. [Online]. Available: http://dx.doi.org/10.1021/ja01539a017

[26] Z. Li, W. Zhang, Y. Luo, J. Yang, and J. G. Hou, "How graphene is cut upon oxidation?" *J. Am. Chem. Soc.*, vol. 131, no. 18, pp. 6320–6321, May 2009. [Online]. Available: http://dx.doi.org/10.1021/ja8094729

[27] Y. Stehle, H. M. Meyer, R. R. Unocic, M. Kidder, G. Polizos, P. G. Datskos, R. Jackson, S. N. Smirnov, and I. V. Vlassiouk, "Synthesis of hexagonal boron nitride monolayer: Control of nucleation and crystal morphology," *Chem. Mater.*, vol. 27, no. 23, pp. 8041–8047, Dec. 2015. [Online]. Available: http://dx.doi.org/10.1021/acs.chemmater.5b03607

[28] L. H. Li, J. Cervenka, K. Watanabe, T. Taniguchi, and Y. Chen, "Strong oxidation resistance of atomically thin boron nitride nanosheets," *ACS Nano*, vol. 8, no. 2, pp. 1457–1462, Feb. 2014. [Online]. Available: http://dx.doi.org/10.1021/nn500059s

[29] N. Kostoglou, K. Polychronopoulou, and C. Rebholz, "Thermal and chemical stability of hexagonal boron nitride (h-bn) nanoplatelets," *Vacuum*, vol. 112, pp. 42 – 45, 2015. [Online]. Available: http://www.sciencedirect.com/science/article/pii/S0042207X14003625

[30] X. Li, X. Hao, M. Zhao, Y. Wu, J. Yang, Y. Tian, and G. Qian, "Exfoliation of hexagonal boron nitride by molten hydroxides," *Advanced Materials*, vol. 25, no. 15, pp. 2200–2204, 2013. [Online]. Available: http://dx.doi.org/10.1002/adma.201204031

[31] L. Shen, Y. Zhao, Y. Wang, R. Song, Q. Yao, S. Chen, and Y. Chai, "A long-term corrosion barrier with an insulating boron nitride monolayer," *J. Mater. Chem. A*, vol. 4, pp. 5044–5050, 2016. [Online]. Available: http://dx.doi.org/10.1039/C6TA01604A

[32] T. Belytschko, S. P. Xiao, G. C. Schatz, and R. S. Ruoff, "Atomistic simulations of nanotube fracture," *Phys. Rev. B*, vol. 65, p. 235430, Jun 2002. [Online]. Available: http://link.aps.org/doi/10.1103/PhysRevB.65.235430

[33] D. D. L. Chung, "Review graphite," *Journal of Materials Science*, vol. 37, no. 8, pp. 1475–1489, 2002. [Online]. Available: http://dx.doi.org/10.1023/A:1014915307738

[34] C. Lee, X. Wei, J. W. Kysar, and J. Hone, "Measurement of the elastic properties and intrinsic strength of monolayer graphene," *Science*, vol. 321, pp. 385–388, 2008.

[35] K. L. Johnson, K. Kendall, and A. D. Roberts, "Surface energy and the contact of elastic solids," *Proceedings of the Royal Society of London A: Mathematical, Physical and Engineering Sciences*, vol. 324, no. 1558, pp. 301–313, 1971. [Online]. Available: http://rspa.royalsocietypublishing.org/content/324/1558/301

[36] J. Castle and R. Ke, "Studies by auger spectroscopy of pit initiation at the site of inclusions in stainless steel," *Corrosion Science*, vol. 30, no. 4, pp. 409 – 428, 1990. [Online]. Available: http://www.sciencedirect.com/science/article/pii/0010938X90900479

[37] G. S. Eklund, "Initiation of pitting at sulfide inclusions in stainless steel," *Journal of The Electrochemical Society*, vol. 121, no. 4, pp. 467–473, 1974. [Online]. Available: http://jes.ecsdl.org/content/121/4/467.abstract

[38] J. Davis, *Corrosion: Understanding the Basics*. ASM International, 2000. [Online]. Available: https://books.google.dk/books?id=D0nAMorpSIYC

[39] B. Weiss and R. Stickler, "Phase instabilities during high temperature exposure of 316 austenitic stainless steel," *Metallurgical Transactions*, vol. 3, no. 4, pp. 851–866, 1972. [Online]. Available: http://dx.doi.org/10.1007/BF02647659

[40] P. Blake, E. W. Hill, A. H. Castro Neto, K. S. Novoselov, D. Jiang, R. Yang, T. J. Booth, and A. K. Geim, "Making graphene visible," *Applied Physics Letters*, vol. 91, no. 6, 2007. [Online]. Available: http://scitation.aip.org/content/aip/journal/apl/91/6/10.1063/1.2768624

[41] X. H. Kong, H. X. Ji, R. D. Piner, H. F. Li, C. W. Magnuson, C. Tan, A. Ismach, H. Chou, and R. S. Ruoff, "Non-destructive and rapid evaluation of chemical vapor deposition graphene by dark field optical microscopy," *Applied Physics Letters*, vol. 103, no. 4, 2013. [Online]. Available: http://scitation.aip.org/content/aip/journal/apl/103/4/10.1063/1.4816752

[42] M. S. Dresselhaus, A. Jorio, M. Hofmann, G. Dresselhaus, and R. Saito, "Perspectives on carbon nanotubes and graphene raman spectroscopy," *Nano Letters*, vol. 10, no. 3, pp. 751–758, 2010.

[43] A. C. Ferrari, "Raman spectroscopy of graphene and graphite: Disorder, electron-phonon coupling, doping and nonadiabatic effects," *Solid State Communications*, vol. 143, no. 1-2, pp. 47 – 57, 2007, exploring grapheneRecent research advances. [Online]. Available: http://www.sciencedirect.com/science/article/pii/S0038109807002967

[44] A. C. F. . D. M. Basko, "Raman spectroscopy as a versatile tool for studying the properties of graphene," *NATURE NANOTECHNOLOGY*, vol. 8, pp. 235–246, 2013.

[45] A. C. Ferrari, J. C. Meyer, V. Scardaci, C. Casiraghi, M. Lazzeri, F. Mauri, S. Piscanec, D. Jiang, K. S. Novoselov, S. Roth, and A. K. Geim, "Raman spectrum of graphene and graphene layers," *Phys. Rev. Lett.*, vol. 97, p. 187401, Oct 2006. [Online]. Available: http://link.aps.org/doi/10.1103/PhysRevLett.97.187401

[46] L. Malard, M. Pimenta, G. Dresselhaus, and M. Dresselhaus, "Raman spectroscopy in graphene," *Physics Reports*, vol. 473, no. 5-6, pp. 51 – 87, 2009. [Online]. Available: http://www.sciencedirect.com/science/article/pii/S0370157309000520

[47] S. D. Costa, A. Righi, C. Fantini, Y. Hao, C. Magnuson, L. Colombo, R. S. Ruoff, and M. A. Pimenta, "Resonant raman spectroscopy of graphene grown on copper substrates," *Solid State Communications*, vol. 152, no. 15, pp. 1317 – 1320, 2012, exploring Graphene, Recent Research Advances. [Online]. Available: http://www.sciencedirect.com/science/article/pii/S0038109812002992

[48] X. Yin, Y. Li, F. Ke, C. Lin, H. Zhao, L. Gan, Z. Luo, R. Zhao, T. F. Heinz, and Z. Hu, "Evolution of the raman spectrum of graphene grown on copper upon oxidation of the substrate," *Nano Research*, vol. 7, no. 11, pp. 1613–1622, 2014. [Online]. Available: http://dx.doi.org/10.1007/s12274-014-0521-0

[49] J. Dubessy, M. Caumon, and F. Rull, *Raman Spectroscopy Applied to Earth Sciences and Cultural Heritage:*, ser. EMU Notes. European Mineralogical Union, 2012. [Online]. Available: https://books.google.dk/books?id=_am_CQAAQBAJ

[50] X. Wang, Y. P. Chen, and D. D. Nolte, "Strong anomalous optical dispersion of graphene: complex refractive index measured by picometrology," *Opt. Express*, vol. 16, no. 26, pp. 22 105–22 112, Dec 2008. [Online]. Available: http://www.opticsexpress.org/abstract.cfm?URI=oe-16-26-22105

[51] J. Cazes, *Analytical Instrumentation Handbook, Third Edition*. CRC Press, 2004. [Online]. Available: https://books.google.dk/books?id=DN2zCrS6wywC

[52] R. V. Gorbachev, I. Riaz, R. R. Nair, R. Jalil, L. Britnell, B. D. Belle, E. W. Hill, K. S. Novoselov, K. Watanabe, T. Taniguchi, A. K. Geim, and P. Blake, "Hunting for monolayer boron nitride: Optical and raman signatures," *Small*, vol. 7, no. 4, pp. 465–468, 2011. [Online]. Available: http://dx.doi.org/10.1002/smll.201001628

[53] C. Oatley, W. Nixon, and R. Pease, "Scanning electron microscopy," *Advances in Electronics and Electron Physics*, vol. 21, pp. 181 – 247, 1966. [Online]. Available: http://www.sciencedirect.com/science/article/pii/S0065253908610100

[54] D. C. Joy, "Beam interactions, contrast and resolution in the sem," *Journal of Microscopy*, vol. 136, no. 2, pp. 241–258, 1984. [Online]. Available: http://dx.doi.org/10.1111/j.1365-2818.1984.tb00532.x

[55] L. Giannuzzi and F. Stevie, "A review of focused ion beam milling techniques for {TEM} specimen preparation," *Micron*, vol. 30, no. 3, pp. 197 – 204, 1999. [Online]. Available: http://www.sciencedirect.com/science/article/pii/S0968432899000050

[56] J. H. Warner, M. H. Rummeli, L. Ge, T. Gemming, B. Montanari, N. M. Harrison, B. Buchner, and G. A. D. Briggs, "Structural transformations in graphene studied with high spatial and temporal resolution," *Nature Nanotechnology*, vol. 4, no. 8, pp. 500–504, Aug. 2009. [Online]. Available: http://dx.doi.org/10.1038/nnano.2009.194

[57] D. Bell and N. Erdman, *Low Voltage Electron Microscopy: Principles and Applications*, ser. RMS - Royal Microscopical Society. Wiley, 2012. [Online]. Available: https://books.google.dk/books?id=o7NP9apZkpAC

[58] A. Jablonski and C. J. Powell, "Information depth and the mean escape depth in auger electron spectroscopy and x-ray photoelectron spectroscopy," *Journal of Vacuum Science & Technology A*, vol. 21, no. 1, pp. 274–283, 2003. [Online]. Available: http://scitation.aip.org/content/avs/journal/jvsta/21/1/10.1116/1.1538370

[59] J. Díaz, G. Paolicelli, S. Ferrer, and F. Comin, "Separation of the sp^3 and sp^2 components in the c1 s photoemission spectra of amorphous carbon films," *Phys. Rev. B*, vol. 54, pp. 8064–8069, Sep 1996. [Online]. Available: http://link.aps.org/doi/10.1103/PhysRevB.54.8064

[60] I. Platzman, R. Brener, H. Haick, and R. Tannenbaum, "Oxidation of polycrystalline copper thin films at ambient conditions," *The Journal of Physical Chemistry C*, vol. 112, no. 4, pp. 1101–1108, 2008. [Online]. Available: http://dx.doi.org/10.1021/jp076981k

[61] C. Wagner, "Sensitivity factors for xps analysis of surface atoms," *Journal of Electron Spectroscopy and Related Phenomena*, vol. 32, no. 2, pp. 99 – 102, 1983. [Online]. Available: http://www.sciencedirect.com/science/article/pii/0368204883850877

[62] P. R. Kidambi, R. Blume, J. Kling, J. B. Wagner, C. Baehtz, R. S. Weatherup, R. Schloegl, B. C. Bayer, and S. Hofmann, "In situ observations during chemical vapor deposition of hexagonal boron nitride on polycrystalline copper," *Chemistry of Materials*, vol. 26, no. 22, pp. 6380–6392, 2014, pMID: 25673919. [Online]. Available: http://dx.doi.org/10.1021/cm502603n

[63] O. W. Stokes, P. M. D. Fiore, J. T. Barss, A. Koerber, J. L. Gilbert, and E. P. Lautenschlager, "Corrosion in stainless-steel and nickel-titanium files," *Journal of Endodontics*, vol. 25, no. 1, pp. 17 – 20, 1999. [Online]. Available: http://www.sciencedirect.com/science/article/pii/S0099239999803926

[64] D. Strmcnik, P. P. Lopes, B. Genorio, V. R. Stamenkovic, and N. M. Markovic, "Design principles for hydrogen evolution reaction catalyst materials," *Nano Energy*, pp. –, 2016. [Online]. Available: http://www.sciencedirect.com/science/article/pii/S2211285516300738

[65] R. Rofagha, R. Langer, A. El-Sherik, U. Erb, G. Palumbo, and K. Aust, "The corrosion behaviour of nanocrystalline nickel," *Scripta Metallurgica et Materialia*, vol. 25, no. 12, pp. 2867 – 2872, 1991. [Online]. Available: http://www.sciencedirect.com/science/article/pii/0956716X9190171V

[66] C. Clayton and Y. Lu, "A bipolar model of the passivity of stainless steel: the role of mo addition," *Journal of the Electrochemical Society*, vol. 133, no. 12, pp. 2465–2473, 1986. [Online]. Available: http://jes.ecsdl.org.globalproxy.cvt.dk/content/133/12/2465.full.pdf

[67] M. Orazem and B. Tribollet, *Electrochemical Impedance Spectroscopy*, ser. The ECS Series of Texts and Monographs. Wiley, 2011. [Online]. Available: https://books.google.dk/books?id=uSO08d-FBh0C

[68] A. C. Stoot, R. Birney, and T. Booth, "Working electrode holder and electrochemical cell," European Patent EP14 178 928, jul 29, 2014. [Online]. Available: https://patentscope.wipo.int/search/en/detail.jsf?docId=WO2016016214

[69] L. Gray, N. Varennes, B. A. Bloor, M. O'Donoghue, R. Garrett, R. Graham, V. Datta, and B. Franke, "08027 insights into atlas cell testing for selection of linings for oil and gas production vessels and tanks," in *NACE*, New Orleans, Louisiana,, 2008. [Online]. Available: http://www.nace.org/cstm/Store/Product.aspx?id=2b1bbf16-f82b-dd11-9bd4-0017a446694e

[70] S. Hofmann, P. Braeuninger-Weimer, and R. S. Weatherup, "Cvd-enabled graphene manufacture and technology," *The Journal of Physical Chemistry Letters*, vol. 6, no. 14, pp. 2714–2721, 2015. [Online]. Available: http://dx.doi.org/10.1021/acs.jpclett.5b01052

[71] R. S. Weatherup, B. Dlubak, and S. Hofmann, "Kinetic control of catalytic cvd for high-quality graphene at low temperatures," *ACS Nano*, vol. 6, no. 11, pp. 9996–10 003, 2012, pMID: 23025628. [Online]. Available: http://dx.doi.org/10.1021/nn303674g

[72] Y. Huang, X. Zeng, X. Hu, and F. Liu, "Corrosion resistance properties of electroless nickel composite coatings," *Electrochimica Acta*, vol. 49, no. 25, pp. 4313 – 4319, 2004. [Online]. Available: http://www.sciencedirect.com/science/article/pii/S0013468604003780

[73] J. J. Lander, H. E. Kern, and A. L. Beach, "Solubility and diffusion coefficient of carbon in nickel: Reaction rates of nickel-carbon alloys with barium oxide," *Journal of Applied Physics*, vol. 23, no. 12, pp. 1305–1309, 1952. [Online]. Available: http://scitation.aip.org/content/aip/journal/jap/23/12/10.1063/1.1702064

[74] J. H. Mun and B. J. Cho, "Synthesis of monolayer graphene having a negligible amount of wrinkles by stress relaxation," *Nano Lett.*, vol. 13, no. 6, pp. 2496–2499, Jun. 2013. [Online]. Available: http://dx.doi.org/10.1021/nl4005578

[75] A. Cabrero-Vilatela, R. S. Weatherup, P. Braeuninger-Weimer, S. Caneva, and S. Hofmann, "Towards a general growth model for graphene cvd on transition metal catalysts," *Nanoscale*, vol. 8, pp. 2149–2158, 2016. [Online]. Available: http://dx.doi.org/10.1039/C5NR06873H

[76] A. C. Stoot, L. Camilli, S.-A. Spiegelhauer, F. Yu, and P. Bøggild, "Multilayer graphene for long-term corrosion protection of stainless steel bipolar plates for polymer electrolyte membrane fuel cell," *Journal of Power Sources*, vol. 293, pp. 846 – 851, 2015. [Online]. Available: http://www.sciencedirect.com/science/article/pii/S0378775315010435

[77] R. S. Weatherup, B. C. Bayer, R. Blume, C. Baehtz, P. R. Kidambi, M. Fouquet, C. T. Wirth, R. Schlögl, and S. Hofmann, "On the mechanisms of ni-catalysed graphene chemical vapour deposition," *ChemPhysChem*, vol. 13, no. 10, pp. 2544–2549, 2012. [Online]. Available: http://dx.doi.org/10.1002/cphc.201101020

[78] I. Adams, "Improved mode of electroplating with nickel," May 25 1869, uS Patent 90,332. [Online]. Available: https://www.google.com/patents/US90332

[79] K. Liu, Y.-M. Chen, G. M. Policastro, M. L. Becker, and Y. Zhu, "Three-dimensional bicontinuous graphene monolith from polymer templates," *ACS Nano*, vol. 9, no. 6, pp. 6041–6049, Jun. 2015. [Online]. Available: http://dx.doi.org/10.1021/acsnano.5b01006

[80] R. Rao, R. Podila, R. Tsuchikawa, J. Katoch, D. Tishler, A. M. Rao, and M. Ishigami, "Effects of layer stacking on the combination raman modes in graphene," *ACS Nano*, vol. 5, no. 3, pp. 1594–1599, 2011, pMID: 21204569. [Online]. Available: http://dx.doi.org/10.1021/nn1031017

[81] D. R. Lenski and M. S. Fuhrer, "Raman and optical characterization of multilayer turbostratic graphene grown via chemical vapor deposition," *Journal of Applied Physics*, vol. 110, no. 1, 2011. [Online]. Available: http://scitation.aip.org/content/aip/journal/jap/110/1/10.1063/1.3605545

[82] A. Reina, X. Jia, J. Ho, D. Nezich, H. Son, V. Bulovic, M. S. Dresselhaus, and J. Kong, "Large area, few-layer graphene films on arbitrary substrates by chemical vapor deposition," *Nano Letters*, vol. 9, no. 1, pp. 30–35, 2009, pMID: 19046078. [Online]. Available: http://dx.doi.org/10.1021/nl801827v

[83] I. Vlassiouk, M. Regmi, P. Fulvio, S. Dai, P. Datskos, G. Eres, and S. Smirnov, "Role of hydrogen in chemical vapor deposition growth of large single-crystal graphene," *ACS Nano*, vol. 5, no. 7, pp. 6069–6076, 2011, pMID: 21707037. [Online]. Available: http://dx.doi.org/10.1021/nn201978y

[84] A. C. Stoot, "Graphene on steel for protection against abrasive and corrosive environments," Master's thesis, DTU Nanotech, dec 2012.

[85] X. Li, W. Cai, L. Colombo, and R. S. Ruoff, "Evolution of graphene growth on ni and cu by carbon isotope labeling," *Nano Letters*, vol. 9, no. 12, pp. 4268–4272, 2009, pMID: 19711970. [Online]. Available: http://dx.doi.org/10.1021/nl902515k

[86] D. Yoon, Y.-W. Son, and H. Cheong, "Negative thermal expansion coefficient of graphene measured by raman spectroscopy," *Nano Letters*, vol. 11, no. 8, pp. 3227–3231, 2011, pMID: 21728349. [Online]. Available: http://dx.doi.org/10.1021/nl201488g

[87] T. Filleter, J. L. McChesney, A. Bostwick, E. Rotenberg, K. V. Emtsev, T. Seyller, K. Horn, and R. Bennewitz, "Friction and dissipation in epitaxial graphene films," *Phys. Rev. Lett.*, vol. 102, p. 086102, Feb 2009. [Online]. Available: http://link.aps.org/doi/10.1103/PhysRevLett.102.086102

[88] W. Cai, J. An, S. Kim, J. Nah, D. Yang, R. Piner, A. Velamakanni, I. Jung, E. Tutuc, S. K. Banerjee, L. Colombo, R. S. Ruoff, and X. Li, "Large-area synthesis of high-quality and uniform graphene films on copper foils," *Science*, vol. 324, pp. 1312–1314, 2009.

[89] V. Miseikis, D. Convertino, N. Mishra, M. Gemmi, T. Mashoff, S. Heun, N. Haghighian, F. Bisio, M. Canepa, V. Piazza, and C. Coletti, "Rapid cvd growth of millimetre-sized single crystal graphene using a cold-wall reactor," *2D Materials*, vol. 2, no. 1, p. 014006, 2015. [Online]. Available: http://stacks.iop.org/2053-1583/2/i=1/a=014006

[90] O. Frank, J. Vejpravova, V. Holy, L. Kavan, and M. Kalbac, "Interaction between graphene and copper substrate: The role of lattice orientation," *Carbon*, vol. 68, pp. 440 – 451, 2014. [Online]. Available: http://www.sciencedirect.com/science/article/pii/S0008622313010695

[91] J. A. Cahill and A. D. Kirshenbaum, "The density of liquid copper from its melting point (1356°k.) to 2500°k. and an estimate of its critical constants1,2," *The Journal of Physical Chemistry*, vol. 66, no. 6, pp. 1080–1082, 1962. [Online]. Available: http://dx.doi.org/10.1021/j100812a027

[92] S. Frueh, R. Kellett, C. Mallery, T. Molter, W. S. Willis, C. King'ondu, and S. L. Suib, "Pyrolytic decomposition of ammonia borane to boron nitride," *Inorganic Chemistry*, vol. 50, no. 3, pp. 783–792, 2011, pMID: 21182274. [Online]. Available: http://dx.doi.org/10.1021/ic101020k

[93] K. K. Kim, A. Hsu, X. Jia, S. M. Kim, Y. Shi, M. Hofmann, D. Nezich, J. F. Rodriguez-Nieva, M. Dresselhaus, T. Palacios, and J. Kong, "Synthesis of monolayer hexagonal boron nitride on cu foil using chemical vapor deposition," *Nano*

Letters, vol. 12, no. 1, pp. 161–166, 2012, pMID: 22111957. [Online]. Available: http://dx.doi.org/10.1021/nl203249a

[94] A. C. Stoot and L. Camilli, "Chemical vapour deposition from a radiation-sensitive precursor," European Patent EP 16 159 305, 2016.

[95] Z. Liu, Y. Gong, W. Zhou, L. Ma, J. Yu, J. C. Idrobo, J. Jung, A. H. MacDonald, R. Vajtai, J. Lou, and P. M. Ajayan, "Ultrathin high-temperature oxidation-resistant coatings of hexagonal boron nitride," *Nat Commun*, vol. 4, Oct. 2013. [Online]. Available: http://dx.doi.org/10.1038/ncomms3541

[96] L. Lindsay and D. A. Broido, "Enhanced thermal conductivity and isotope effect in single-layer hexagonal boron nitride," *Phys. Rev. B*, vol. 84, p. 155421, Oct 2011. [Online]. Available: http://link.aps.org/doi/10.1103/PhysRevB.84.155421

[97] L. H. Li, T. Xing, Y. Chen, and R. Jones, "Boron nitride nanosheets for metal protection," *Advanced Materials Interfaces*, vol. 1, no. 8, pp. n/a–n/a, 2014. [Online]. Available: http://dx.doi.org/10.1002/admi.201300132

[98] G. Lu, T. Wu, Q. Yuan, H. Wang, H. Wang, F. Ding, X. Xie, and M. Jiang, "Synthesis of large single-crystal hexagonal boron nitride grains on cu-ni alloy," *Nat Commun*, vol. 6, Jan. 2015. [Online]. Available: http://dx.doi.org/10.1038/ncomms7160

[99] I. Platzman, R. Brener, H. Haick, and R. Tannenbaum, "Oxidation of polycrystalline copper thin films at ambient conditions," *The Journal of Physical Chemistry C*, vol. 112, no. 4, pp. 1101–1108, 2008. [Online]. Available: http://dx.doi.org/10.1021/jp076981k

[100] R. Frerichs and I. Liberman, "Surface mobility of copper ions on cuprous oxide," *Phys. Rev.*, vol. 121, pp. 991–996, Feb 1961. [Online]. Available: http://link.aps.org/doi/10.1103/PhysRev.121.991

[101] X. Jiang, T. Herricks, and Y. Xia, "Cuo nanowires can be synthesized by heating copper substrates in air," *Nano Lett.*, vol. 2, no. 12, pp. 1333–1338, Dec. 2002. [Online]. Available: http://dx.doi.org/10.1021/nl0257519

[102] B. Wang, H. Zhang, Z. Chen, Y. Zhang, B. Wang, Y. Sui, X. Li, X. Xie, G. Yu, Z. Jin, X. Liu, and Y. Zhang, "The distribution of wrinkles and their effects on the oxidation resistance of chemical vapor deposition graphene," *Carbon*, vol. 70, pp. 81–86, 2014.

[103] M. O'Reilly, X. Jiang, J. Beechinor, S. Lynch, C. NíDheasuna, J. Patterson, and G. Crean, "Investigation of the oxidation behaviour of thin film and bulk copper," *Applied Surface Science*, vol. 91, no. 1, pp. 152 – 156, 1995. [Online]. Available: http://www.sciencedirect.com/science/article/pii/0169433295001115

[104] T. L. Barr, "An esca study of the termination of the passivation of elemental metals," *The Journal of Physical Chemistry*, vol. 82, no. 16, pp. 1801–1810, 1978. [Online]. Available: http://dx.doi.org/10.1021/j100505a006

[105] N.-W. Pu, G.-N. Shi, Y.-M. Liu, X. Sun, J.-K. Chang, C.-L. Sun, M.-D. Ger, C.-Y. Chen, P.-C. Wang, Y.-Y. Peng, C.-H. Wu, and S. Lawes, "Graphene grown on stainless steel as a high-performance and ecofriendly anti-corrosion coating for polymer electrolyte membrane fuel cell bipolar plates," *Journal of Power Sources*, vol. 282, no. 0, pp. 248 – 256, 2015. [Online]. Available: http://www.sciencedirect.com/science/article/pii/S0378775315002785

[106] H. Bruus, *Theoretical Microfluidics*, 1st ed. New York,: Oxford University Press, 2007.

[107] J. O. Bockris and E. C. Potter, "The mechanism of hydrogen evolution at nickel cathodes in aqueous solutions," *The Journal of Chemical Physics*, vol. 20, no. 4, pp. 614–628, 1952. [Online]. Available: http://scitation.aip.org/content/aip/journal/jcp/20/4/10.1063/1.1700503

[108] F. Yu, A. C. Stoot, P. Boggild, and L. Camilli, "Failure of multi-layer graphene coatings in acidic media," *RSC Adv.*, vol. 6, pp. 21 497–21 502, 2016. [Online]. Available: http://dx.doi.org/10.1039/C6RA01556E

[109] K. Lee, S. Lee, D.-Y. Khang, and T. Lee, "Wrinkling evolution of a growing bubble: the wonders of petal-like patterns in amorphous silicon membranes," *Soft Matter*, vol. 6, pp. 3249–3256, 2010. [Online]. Available: http://dx.doi.org/10.1039/C003293J

[110] N. Agmon, "The grotthuss mechanism," *Chemical Physics Letters*, vol. 244, no. 5, pp. 456 – 462, 1995. [Online]. Available: http://www.sciencedirect.com/science/article/pii/000926149500905J

[111] B. Beverskog and I. Puigdomenech, "Revised pourbaix diagrams for nickel at 25-300 °c," *Corrosion Science*, vol. 39, no. 5, pp. 969 – 980, 1997. [Online]. Available: http://www.sciencedirect.com/science/article/pii/S0010938X97000024

[112] R. W. Revie and H. H. Uhlig, *Corrosion and corrosion control*, 4th ed. John Wiley & Sons, 2008.

[113] Y. Zhou, W. Chen, P. Cui, J. Zeng, Z. Lin, E. Kaxiras, and Z. Zhang, "Enhancing the hydrogen activation reactivity of nonprecious metal substrates via confined catalysis underneath graphene," *Nano Letters*, vol. 0, no. 0, p. null, 2016, pMID: 27588556. [Online]. Available: http://dx.doi.org/10.1021/acs.nanolett.6b02052

[114] F. Yu, L. Camilli, P. Bøggild, P. Whelan, T. Booth, and A. Stoot, "Graphene polymer hybrid coatings with a layered structure," European Patent EP16 176 135, 2016.

List of Figures

Appendix A

Publication 1

Journal of Power Sources 293 (2015) 846–851

Contents lists available at ScienceDirect

Journal of Power Sources

journal homepage: www.elsevier.com/locate/jpowsour

Multilayer graphene for long-term corrosion protection of stainless steel bipolar plates for polymer electrolyte membrane fuel cell

Adam C. Stoot [a], Luca Camilli [a], Susie-Ann Spiegelhauer [b], Feng Yu [a], Peter Bøggild [a, *]

[a] Technical University of Denmark, Department of Micro- and Nanotechnology, Kgs. Lyngby, DK-2800, Denmark
[b] Accoat, SP-Group A/S, Kvistgård, DK-3490, Denmark

HIGHLIGHTS

- Nickel-coating on stainless steel enhances its short term anti-corrosion properties.
- Multi-layer graphene film on steel enhances long-term corrosion resistance.
- The effect of nickel in corrosion resistance of graphene/nickel/steel is important.
- Accelerated reaction kinetics are used to simulate effect of longer exposures.

GRAPHICAL ABSTRACT

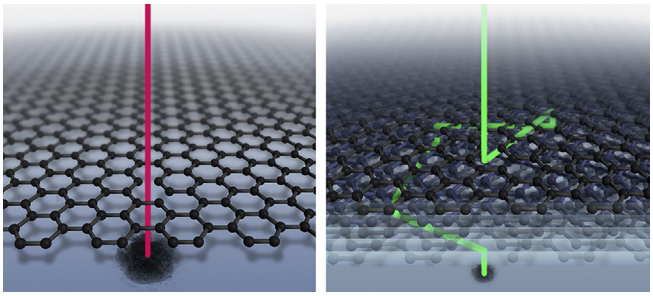

ARTICLE INFO

Article history:
Received 24 March 2015
Received in revised form
15 May 2015
Accepted 2 June 2015
Available online 12 June 2015

Keywords:
Graphene coating
Wet corrosion
Chemical vapour deposition
Raman spectroscopy
Stainless steel
Metal bipolar plate

ABSTRACT

Motivated by similar investigations recently published (Pu et al., 2015), we report a comparative corrosion study of three sets of samples relevant as bipolar plates for polymer electrolyte fuel cells: stainless steel, stainless steel with a nickel seed layer (Ni/SS) and stainless steel with Ni seed layer coated by a multi-layered graphene thin film (G/Ni/SS). The graphene film, synthesized by chemical vapour deposition (CVD), has a moderate amount of defects according to Raman spectroscopy. Short/medium-term corrosion test shows no significant advantage of using G/Ni/SS rather than Ni/SS, both samples exhibiting a similar trend, thus questioning the short-term positive effect of graphene coatings. However, partial immersion in boiling seawater for three weeks reveals a clear superiority of the graphene coating with respect to steel just protected by Ni. After the test, the graphene film is still intact with unchanged defect density. Our results show that even non-perfect multilayer graphene films can considerably increase the lifetime of future-generation bipolar plates for fuel cells.

1. Introduction

After the seminal works by Novoselov and Geim [1], the superior material properties of graphene has fuelled an intense search for practical applications of this planar honeycomb structure of carbon atoms. Graphene and related materials (*i.e.*, other two-dimensional crystals) are expected to have a major impact in several technological fields in the near future [2]. While graphene is chemically inert and impermeable to even hydrogen [3], the effectiveness of graphene as a protective coating is still subject to debate and controversy. While several studies have reported pronounced short- and medium-term protection performance of graphene coatings [4–6], Schriver et al. pointed out that graphene may in fact eventually accelerate corrosion and oxidation of metals over longer periods of time [7].

Very recently, Pu et al. proposed the use of graphene on stainless steel as a high-performance anti-corrosion coating for polymer

* Corresponding author.
E-mail address: peter.boggild@nanotech.dtu.dk (P. Bøggild).

http://dx.doi.org/10.1016/j.jpowsour.2015.06.009
0378-7753/

electrolyte membrane fuel cells bipolar plates [8]. As the growth of large-scale high-quality graphene directly on stainless steel (SS) has not yet been shown to be possible, the authors suggest using a nickel (Ni) seed layer on top of SS (Ni/SS) in order to catalyse the graphene growth. The authors then compare the anti-corrosion performance of three sets of specimens: (i) bare SS, (ii) graphene-coated SS and (iii) graphene-coated Ni/SS (G/Ni/SS). After repeating a potentiodynamic polarization test twenty times for each set of samples they conclude that while the corrosion rate of bare SS and graphene-coated SS increases by almost 50 and 15 times, respectively, the corrosion rate of G/Ni/SS remains almost constant. Since in the case of graphene-coated SS specimen the graphene coverage is non-uniform and incomplete, while for the G/Ni/SS the coverage is close to 100%, the conclusion is that the complete surface coverage of the graphene coating prevents wet corrosion of SS. However, the effect of the Ni seed layer on SS has been overlooked, although Nickel based coatings and alloys have already been proposed as corrosion-resistive bipolar plates in fuel cells [9,10]. Here, we report that both the Ni/SS and the G/Ni/SS exhibit a similar behaviour when subjected to twenty polarization scans under same experimental conditions (2-h test), and thus that a graphene coating does not give a significant contribution to the short-term corrosion resistance of steel. In the long term, however, there is indeed a positive effect of graphene; after 504 h of exposure to boiling seawater (Atlas cell test, see Experimental section for details), there is indeed a clear difference in SS protected by Ni with or without graphene.

2. Experimental

2.1. Fabrication of samples

2 inch diameter, 3 mm thick 304 stainless steel samples were glass blasted and sonicated for 20 min in Triton X before being pre-coated with a 150 μm nickel seed layer using a Technotrans electroplating system without any additives/brighteners.

The chemical vapour deposition (CVD) system used for graphene growth is based on a graphitic block heated by halogen light bulbs and a PID-temperature control. Before insertion into the CVD-chamber, the samples were sonicated in isopropanol and then rinsed in deionized water. As for the growth process, firstly the samples were kept at 850 °C in hydrogen atmosphere for 10 min after which a mixture of hydrogen (24 sccm) and acetylene (12 sccm) was injected for the graphene growth. The samples were cooled down at a fixed rate of 0.5 °C/s in low vacuum (base pressure around 10^{-1} mbar).

2.2. Electrochemical tests

The electrochemical tests were done using a platinum counter electrode, an Ag/AgCl reference electrode and a Quick WE working electrode holder [11] along with the Gamry Reference 3000 potentiostat. The scan rate was 5 mV/s, and 3.5 wt% NaCl solution was the chosen electrolyte. Twenty polarisation scans were performed on each sample and the open circuit potential was monitored to ensure stabilisation between each scan.

2.3. Atlas cell tests

The simulated seawater tests were also done in 3.5 wt% NaCl solution. These long term tests were done at Accoat A/S using an Atlas glass cell. It consists of a glass canister with a hole in both ends allowing two samples to be tested simultaneously (see Supplementary Materials). The samples are only partially immersed in the corrosive solution, thus testing both liquid- and vapour phase-induced corrosion. Heating the solution to the boiling point has two effects; reaction kinetics is accelerated and large temperature gradients arise over the samples with their backside being exposed to room temperature. This furthermore tests the tendency of the coating to delaminate due to condensation and bubble formation at the coating/sample-interface in case of a semi-permeable coating or poor adhesion.

It is worth noting that the corrosive environment at an elevated temperature of the Atlas test presents a scenario similar to a fuel cell in operation, including the temperature gradients due to the surroundings being at a lower temperature.

2.4. Characterisation

The structure and composition of the samples were investigated with Scanning Electron Microscopy and Energy Dispersive Spectroscopy using FEI Quanta 200 FEG and FEI Inspect. Focused Ion Beam milling was done using FEI Helios dual beam focused ion beam microscope. Raman spectra were obtained using a Thermo Scientific DXR confocal Raman Microscope with a 455 nm laser, 2 mW power and a spot-size of approximately 1 μm.

3. Results and discussion

Fig. 1(a) shows an averaged Raman spectrum recorded on several locations of the G/Ni/SS sample. The ratio of the intensities of the 2D-peak (~2750 cm^{-1}) to the G-peak (~1590 cm^{-1}) is ~0.26 ± 0.01, indicating the multi-layered character of the graphene film. The thickness was 25 nm–40 nm measured by SEM of Focused Ion Beam milled sections (see supplementary materials). The D-band, located at ~1370 cm^{-1}, indicates the presence of defects and structural imperfections in the graphene lattice, which could be related to the small size of polycrystalline graphene domains [12]. Additionally, the Raman map displayed in Fig. 1(b) shows the full coverage and high homogeneity of the multilayer graphene coating over a millimetre-sized area of the sample, confirming the well-known high catalytic activity of Ni towards the synthesis of graphene [13].

In Fig. 2(a) we report the results of a single polarization scan acquired for three sets of samples: (i) bare SS, (ii) Ni/SS and (iii) G/Ni/SS. For comparison, we report on the same graph the data for a G/Ni/SS sample taken from Ref. [8]. Firstly, observing the anodic part of the polarization curve for SS (black curve), it is possible to observe the passivation layer formation (red arrow) and its subsequent break-down (blue arrow). Such a passivating film reduces the conductivity of the surface due to the oxide phase, and thus results in being detrimental in view of applications as a bipolar plate for polymer electrolyte membrane fuel cell. Secondly, we can see that the G/Ni/SS sample of Ref. [8] (brown curve) is performing better than our G/Ni/SS sample (blue curve), with a lower corrosion rate indicated by the curve being located at a lower current density range. We explain the difference with respect to our data as due to the larger defect density in our graphene film compared with the one reported by Pu et al. [8], which can be seen by direct comparison of the Raman spectrum in Fig. 1(a) of this work and the one displayed in Fig. 1(a) of Ref. [8]. In fact, it is well established that ions (such as Cl^- ions), water and oxygen may diffuse through defects of graphene, like grain boundaries and cracks, until reaching the metal surface underneath the coating and beginning its corrosion [14]. Lastly, we want to point out that our Ni/SS sample (green curve) is showing similar performance to the G/Ni/SS sample in Ref. [8] and, therefore, better performance than our G/Ni/SS specimen. This finding is actually not surprising, due to the intrinsic strong corrosion resistance of nickel and nickel-based alloys [15,16].

In order to (i) investigate the medium-term behaviour of the

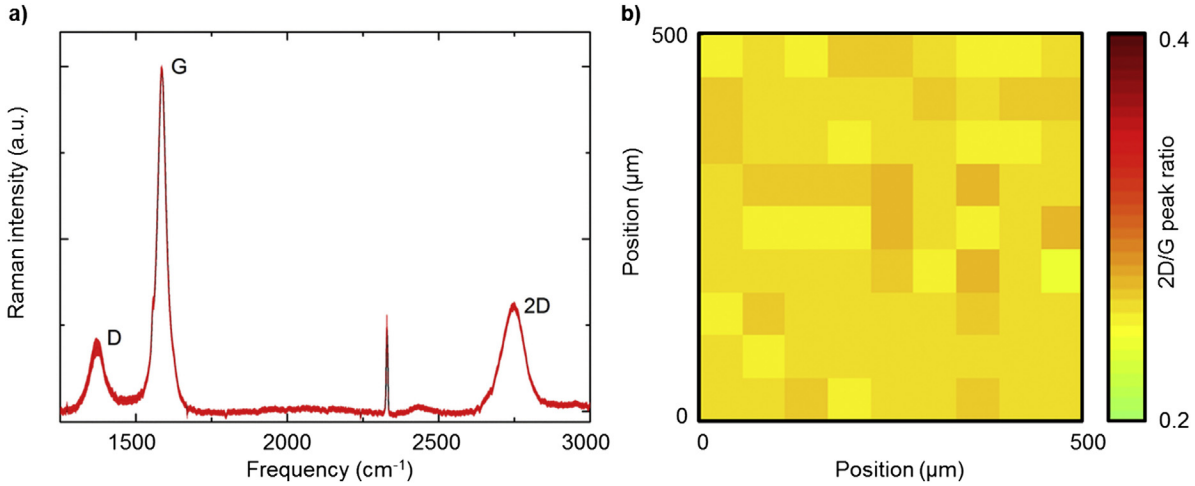

Fig. 1. a) Average Raman spectrum of the G/Ni/SS sample extracted from 100 spots over a millimetre sized area. The width of the graph represents the standard deviation. The sharp peak located at ~2350 cm^{-1} is related to N_2 b) Raman map highlighting the full coverage and high homogeneity of the graphene film.

samples under study and (ii) directly compare our data with that one reported in Ref. [8], we repeated the polarization curves twenty times and plotted our measurements along with the ones for G/Ni/SS of Ref. [8]. As illustrated in Fig. 2(b), the SS sample turned out to be highly degraded after twenty polarization scans, with the corrosion potential being significantly shifted at a lower value (−168 mV) with respect to the one after a single scan (−2 mV). This is ascribed to the breaking down of the metal oxide film passivating the surface of the SS, which is now "less noble" and thus more prone to be corroded [17]. The passivating oxide film breakdown can be seen on the first polarisation scan at an over potential of around 320 mV.

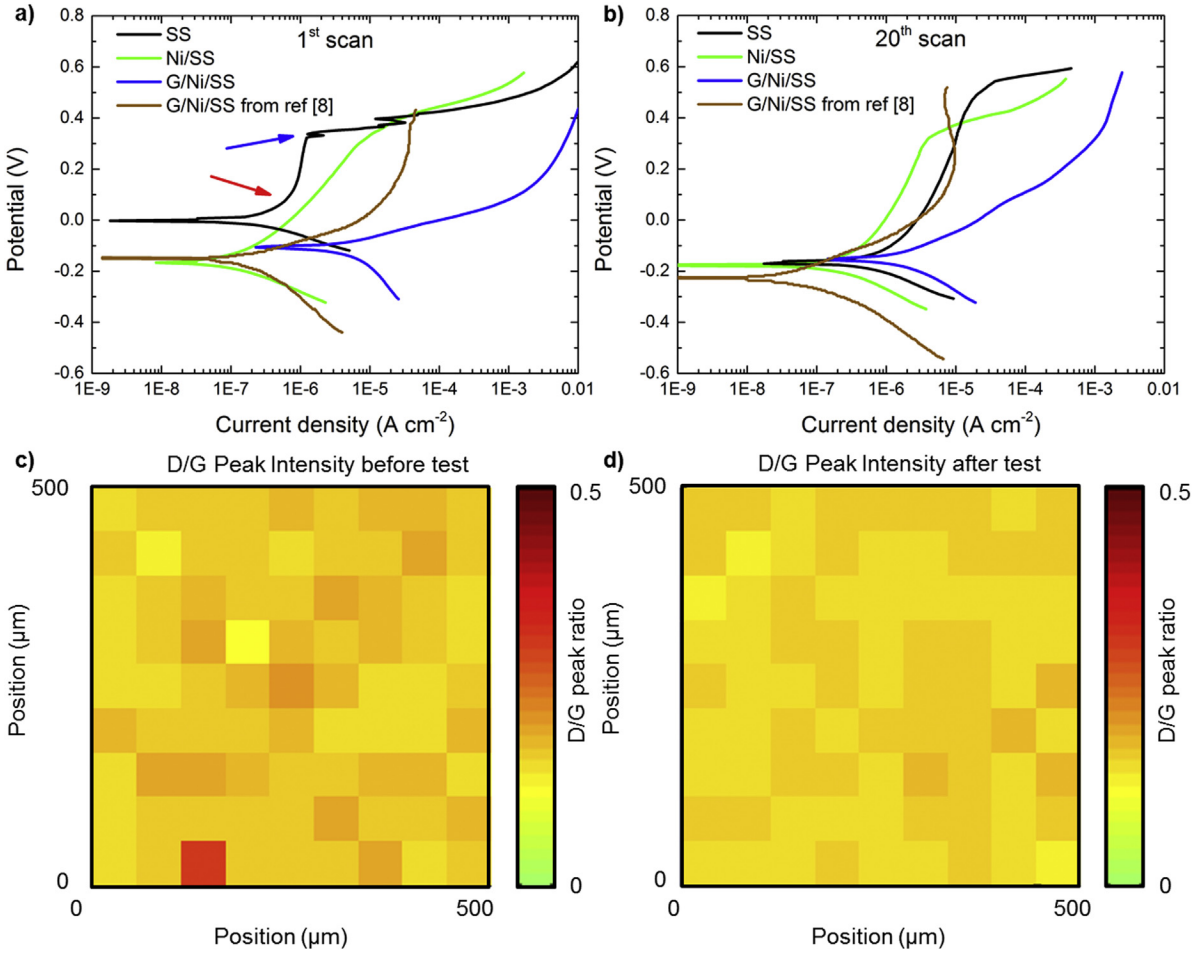

Fig. 2. Potentiodynamic study of SS (black curve), Ni/SS (green curve), G/Ni/SS (blue curve) and a G/Ni/SS from Ref. 7 (brown curve) after (a) one and (b) twenty polarisation scans. (c) and (d): Raman maps of the G/Ni/SS before and after the potendiodynamic study, respectively. The I(D)/I(G) peak which represents the defect density is almost unchanged. (For interpretation of the references to colour in this figure legend, the reader is referred to the web version of this article.)

Both the Ni/SS (green curve) measured by us and the G/Ni/SS (brown curve) from Ref. [8] exhibit strong corrosion resistance, low corrosion current and a trend to keep a constant line shape over 20 polarization scans (see Supplementary Materials). As a matter of fact, the corrosion potential of the Ni/SS is slightly higher than the one of the G/Ni/SS of Ref. [8]. As for our G/Ni/SS sample, the polarisation curve is still located at a higher current density compared to that of the two just-mentioned samples, however, it shows a trend to maintain the performance after twenty polarization scans, in contrast with bare SS (black curve) and similar to our Ni/SS and G/Ni/SS reported in Ref. [8]. It is worth noting that the presence of the graphene coating after the potentiodynamic analysis is confirmed by the Raman maps acquired on the G/Ni/SS before and after testing (Fig. 2(c) and (d), respectively). The D-to G-peak intensity ratio, I(D)/I(G), representing the density of lattice defects [18], is 0.16 ± 0.01 which is within the measurement uncertainty when compared to the 0.17 ± 0.02 obtained before the polarization tests.

Based on these data it is not possible to determine whether the corrosion resistance within the tested timeframe is due to the graphene coating, to the Ni seed layer or both in combination, as all are improving the anti-corrosion performance of steel.

In order to evaluate whether a graphene coating can lead to an actual improvement of SS's corrosion resistance, we apply a much longer test, the Atlas-cell test [19]. The samples are subjected to a harsh wet corrosive environment at an elevated temperature which accelerates the reaction kinetics and also represents a simulation of an environment relevant for polymer fuel cells [20]. The elevated working temperatures and the likelihood of NaCl contamination from *e.g.* ocean mist provide highly corrosive conditions for the cathode. The samples are half immersed in boiling simulated seawater for 504 h, with a large temperature gradient arising owing to their backside being exposed to room temperature.

Fig. 3 displays two samples, Ni/SS and G/Ni/SS before (Fig. 3(a) and (b), respectively) and after the Atlas-cell test (Fig. 3(c) and (d)). The Ni surface without graphene coating exhibits clear signs of corrosion including both Ni(II)oxide (green) as well as other nickel oxides in higher oxidation states (black), which are visible to the naked eye (Fig. 3(a) and c) [21]. The position of the water–vapour interface can easily be observed on the sample. While both the liquid-exposed and gas-exposed sides of the sample appear to be damaged, the latter appears to have suffered the most damage. This may be due to a higher oxygen concentration in the vapour phase than in the liquid phase, which bears resemblance with the working environment of bipolar plate inside a fuel cell where both the oxygen concentration and the temperature are high.

On the contrary, the surface of the graphene-covered sample does not show any sign of degradation when comparing visual appearance of the sample before (Fig. 3(b)) and after (Fig. 3(d)) testing. This is also confirmed by energy dispersive x-ray spectroscopy (EDS) of the samples after testing (see Supplementary Materials), where an oxygen peak is absent for G/Ni/SS, while present in the uncoated nickel reference.

After the Atlas-cell test we investigated the graphene coating, to verify whether it has been damaged or even removed by the

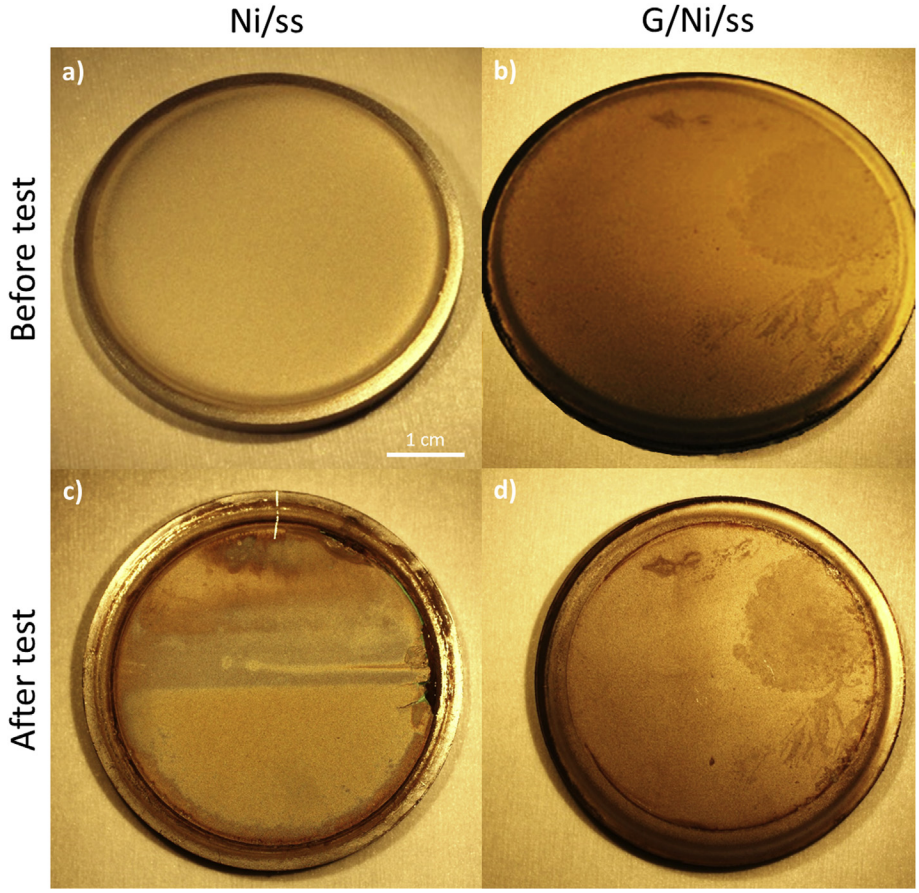

Fig. 3. Optical images of samples before and after test in boiling simulated seawater (i.e., Atlas cell test). a) and b) show Ni/SS and G/Ni/SS samples before testing, respectively. c) and d) display the samples in a) and b) after the test has been carried out, respectively. The graphene-uncoated sample is highly corroded, especially in the vapour side (highlighted by the scratch at the edge of the sample) due to the higher oxygen concentration than in the liquid phase. It is worth noting that the dark areas in the graphene-coated samples were present even before testing, and are the result of the annealing during CVD process.

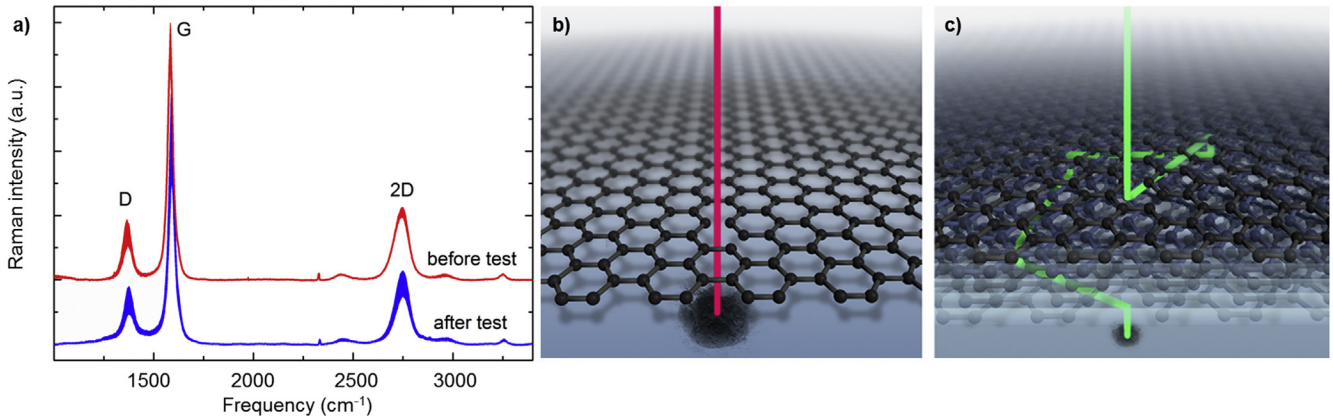

Fig. 4. a) Raman spectra of the graphene-coated sample before (red curve) and after (blue curve) testing in the boiling simulated seawater. The spectra are obtained away from the edge, averaging in different sample locations. The plotted data is the average value with standard deviation error bars being represented by the thickness of the lines. The I(D)/I(G) ratio before the test was 0.19 ± 0.07 while after the test 0.16 ± 0.04. b) and c): Schematic illustration of diffusion paths for single-layer (b) and multi-layer (c) graphene. In the case of a multi-layer film, the diffusion path for oxygen and water molecules is longer. (For interpretation of the references to colour in this figure legend, the reader is referred to the web version of this article.)

aggressive test. As illustrated in Fig. 4(a), comparison of the Raman spectra recorded before and after testing asserts that the graphene coating is still present and intact. Notably, the D-to G-peak intensity ratio, which was 0.19 ± 0.07 before test, is now 0.16 ± 0.04, and thus remains constant within the measurement uncertainty.

At first sight, the positive long-term action of graphene coating shown in this work might seem to be in disagreement with a recent study reported in Ref. [7]. However, it is worth noting that the scenarios are not immediately comparable. While Shiver et al. in Ref. [7] are reporting on the barrier properties of graphene in a dry oxidative environment, we are demonstrating the long-term protection in wet environment, where the reactions involved are different. In addition, while they are investigating the properties of a single-layer graphene coating, here we propose to use a multi-layer graphene film. This film is much thicker than single or few-layer graphene coatings previously reported in literature [22,23], but still extremely thin if compared to standard, industrially available composite coatings [24–26]. This greatly minimises the influence on mechanical tolerances of coated items. Despite the presence of defects, in case of a multi-layered graphene coating, oxygen and water molecules must traverse a complex combination of multiple intercalative paths between the layers, as well as penetrate to deeper layers through lattice imperfections in order to eventually reach the metal surface (Fig. 4(c)). Although producing a realistic simulation of such a system is very challenging, it is safe to assume that the diffusion time of corroding agents will scale with number of layers.

4. Conclusions

In summary, we have compared the corrosion resistance of three bipolar plates similar to those used for polymer fuel cells: (i) an SS substrate, (ii) an SS substrate with a Ni seed layer atop and (iii) an SS substrate with a Ni seed layer atop coated with graphene. We have shown that in the short-/medium-term, the performance of the latter two samples is in fact comparable and the stainless steel substrate is protected when subjected to electrochemical tests in corrosive electrolytes. From this alone, it is unclear whether the presence of the graphene film on top of the Ni seed layer is playing a role in the corrosion protection of steel as concluded by Pu et al. [8]. However, using a longer test in a very harsh environment (*i.e.*, the Atlas-cell test), it is evident that the graphene film is performing much better than just a Ni seed layer toward the protection of steel. This test has a 250 times longer duration than the potentiodynamic analysis reported in Fig. 2(c) and ref. [8] and features (i) accelerated reaction kinetics due to the high temperature as well as (ii) high temperature gradients, which increase the tendency of coatings to delaminate due to condensation and bubble formation at the coating/sample-interface, in case of poor adhesion, permeability or pinholes/cracks [19]. In addition, owing to the remarkable electrical properties of graphene [2], these results could boost the exploitation of graphene in fuel cell application.

Acknowledgement

We would like to thank A. Holm, Grundfos A/S for supplying the 2″ steel discs used for creating the samples. We would also like to thank N. Bild for help with figure 4 b) and c).

This project was supported by The Strategic Danish Research collaboration (DSF) with the DA-GATE project (12-131827) and through the High Technology Foundation (HTF) with the NIAGRA project (058-2012-4).

Appendix A. Supplementary data

Supplementary data related to this article can be found at http://dx.doi.org/10.1016/j.jpowsour.2015.06.009.

References

[1] K.S. Novoselov, A.K. Geim, S.V. Morozov, D. Jiang, Y. Zhang, S.V. Dubonos, I.V. Grigorieva, A.A. Firsov, Electric field effect in atomically thin carbon films, Science 306 (2004) 666–669.

[2] A.C. Ferrari, F. Bonaccorso, V. Falko, K.S. Novoselov, S. Roche, P. Boggild, S. Borini, F.H.L. Koppens, V. Palermo, N. Pugno, J.A. Garrido, R. Sordan, A. Bianco, L. Ballerini, M. Prato, E. Lidorikis, J. Kivioja, C. Marinelli, T. Ryhanen, A. Morpurgo, J.N. Coleman, V. Nicolosi, L. Colombo, A. Fert, M. Garcia-Hernandez, A. Bachtold, G.F. Schneider, F. Guinea, C. Dekker, M. Barbone, Z. Sun, C. Galiotis, A.N. Grigorenko, G. Konstantatos, A. Kis, M. Katsnelson, L. Vandersypen, A. Loiseau, V. Morandi, D. Neumaier, E. Treossi, V. Pellegrini, M. Polini, A. Tredicucci, G.M. Williams, B. Hee Hong, J.-H. Ahn, J. Min Kim, H. Zirath, B.J. van Wees, H. van der Zant, L. Occhipinti, A. Di Matteo, I.A. Kinloch, T. Seyller, E. Quesnel, X. Feng, K. Teo, N. Rupesinghe, P. Hakonen, S.R.T. Neil, Q. Tannock, T. Lofwander, J. Kinaret, Science and technology roadmap for graphene, related two-dimensional crystals, and hybrid systems, Nanoscale 7 (2015) 4598–4810.

[3] J.S. Bunch, S.S. Verbridge, J.S. Alden, A.M. van der Zande, J.M. Parpia, H.G. Craighead, P.L. McEuen, Impermeable atomic membranes, Nano Lett. 8 (8) (2008) 2458–2462.

[4] D. Prasai, J.C. Tuberquia, R.R. Harl, G.K. Jennings, K.I. Bolotin, Graphene: corrosion-inhibiting coating, ACS Nano 6 (2) (2012) 1102–1108.

[5] M. Topsakal, H. Şahin, S. Ciraci, Graphene coatings: an efficient protection from oxidation, Phys. Rev. B 85 (15) (2012) 155445.
[6] S. Chen, L. Brown, M. Levendorf, W. Cai, S.-Y. Ju, J. Edgeworth, X. Li, C.W. Magnuson, A. Velamakanni, R.D. Piner, J. Kang, J. Park, R.S. Ruoff, Oxidation resistance of graphene-coated Cu and Cu/Ni alloy, ACS Nano 5 (2) (2011) 1321–1327.
[7] M. Schriver, W. Regan, W.J. Gannett, A.M. Zaniewski, M.F. Crommie, A. Zettl, Graphene as a long-term metal oxidation barrier: worse than nothing, ACS Nano 7 (7) (2013) 5763–5768.
[8] N.-W. Pu, G.-N. Shi, Y.-M. Liu, X. Sun, J.-K. Chang, C.-L. Sun, M.-D. Ger, C.-Y. Chen, P.-C. Wang, Y.-Y. Peng, C.-H. Wu, S. Lawes, Graphene grown on stainless steel as a high-performance and ecofriendly anti-corrosion coating for polymer electrolyte membrane fuel cell bipolar plates, J. Power Sources 282 (0) (2015) 248–256.
[9] A. Hermann, T. Chaudhuri, P. Spagnol, Bipolar plates for PEM fuel cells: a review, Int. J. Hydrogen Energy 30 (12) (2005) 1297–1302.
[10] H. Tawfik, Y. Hung, D. Mahajan, Metal bipolar plates for PEM fuel cell – a review, J. Power Sources 163 (2) (2007) 755–767.
[11] A. C. Stoot, R. Birney and T. J. Booth, "Working electrode holder and electrochemical cell". Patent EP14178928, 2014.
[12] A.C. Ferrari, J.C. Meyer, V. Scardaci, C. Casiraghi, M. Lazzeri, F. Mauri, S. Piscanec, D. Jiang, K.S. Novoselov, S. Roth, A.K. Geim, Raman spectrum of graphene and graphene layers, Phys. Rev. Lett. 97 (Oct 2006) 187401.
[13] K.S. Kim, Y. Zhao, H. Jang, S.Y. Lee, J.M. Kim, K.S. Kim, J.-H. Ahn, P. Kim, J.-Y. Choi, B.H. Hong, Large-scale pattern growth of graphene films for stretchable transparent electrodes, Nature 457 (7230) (2009) 706–710.
[14] Y.-P. Hsieh, M. Hofmann, K.-W. Chang, J.G. Jhu, Y.-Y. Li, K.Y. Chen, C.C. Yang, W.-S. Chang, L.-C. Chen, Complete corrosion inhibition through graphene defect passivation, ACS Nano 8 (1) (2014) 443–448.
[15] R.A. Antunes, M.C.L. Oliveira, G. Ett, V. Ett, Corrosion of metal bipolar plates for PEM fuel cells: a review, Int. J. Hydrogen Energy 35 (8) (2010) 3632–3647.
[16] J. Sudagar, J. Lian, W. Sha, Electroless nickel, alloy, composite and nano coatings – a critical review, J. Alloys Compd. 571 (0) (2013) 183–204.
[17] L.L. Shreir, G.T. Burstein, Shreir's Corrosion, Elsevier, Cambridge, U.K, 2010.
[18] M.S. Dresselhaus, A. Jorio, M. Hofmann, G. Dresselhaus, R. Saito, Perspectives on carbon nanotubes and graphene Raman spectroscopy, Nano Lett. 10 (3) (2010) 751–758.
[19] Standard Test Method for Chemical Resistance of Protective Linings, ASTM, West Conshohocken, PA, 2012.
[20] W. Vielstich, Handbook of Fuel Cells: Fundamentals Technology and Applications, Wiley, 2009.
[21] N. Greenwood, A. Earnshaw, Chemistry of the Elements, the University of Michigan, Pergamon Press, 1984.
[22] L. Nilsson, M. Andersen, R. Balog, E. Lægsgaard, P. Hofmann, F. Besenbacher, B. Hammer, I. Stensgaard, L. Hornekær, Graphene coatings: probing the limits of the one atom thick protection layer, ACS nano 6 (11) (2012) 10258–10266.
[23] Y. Zhao, Y. Xie, Y.Y. Hui, L. Tang, W. Jie, Y. Jiang, L. Xu, S.P. Lau, Y. Chai, Highly impermeable and transparent graphene as an ultra-thin protection barrier for Ag thin films, J. Mater. Chem. C 1 (32) (2013) 4956–4961.
[24] K. Holmberg, H. Ronkainen, A. Matthews, Tribology of thin coatings, Ceram. Int. 26 (7) (2000) 787–795.
[25] J. Valli, A Review of Adhesion test methods for thin hard coatings, J. Vac. Sci. Technol. 4 (1986) 3007–3014.
[26] R.K.S. Raman, P.C. Banerjee, D.E. Lobo, H. Gullapalli, M. Sumandasa, A. Kumar, L. Choudhary, R. Tkacz, P.M. Ajayan, M. Majumder, Protecting copper from electrochemical degradation by graphene coating, Carbon 50 (11) (2012) 4040–4045.

Appendix B

Publication 2

RSC Advances

PAPER

Cite this: *RSC Adv.*, 2016, **6**, 21497

Failure of multi-layer graphene coatings in acidic media†

F. Yu, A. C. Stoot, P. Bøggild and L. Camilli*

Received 18th January 2016
Accepted 15th February 2016

DOI: 10.1039/c6ra01556e

www.rsc.org/advances

Being impermeable to all gases, graphene has been proposed as an effective ultrathin barrier film and protective coating. However, here it is shown how the gastight property of graphene-based coatings may indirectly lead to their catastrophic failure under certain conditions. When nickel coated with thick, high-quality chemical vapor deposited multilayered graphene is exposed to acidic solutions, a dramatic evolution of gas is observed at the coating–substrate interface. The gas bubbles grow and merge, eventually rupturing and delaminating the coating. This behavior, attributed to cathodic hydrogen evolution, can also occur spontaneously on a range of other technologically important metals and alloys based on iron, zinc, aluminum and manganese; this makes these findings relevant for practical applications of graphene-based coatings.

Introduction

Corrosion, the gradual degradation of metals and alloys by interaction with the environment, is a problem of enormous significance. Costs due to corrosion represent 3–4% of the worldwide BNP.[1] Corrosion and oxidation cause waste of valuable resources, loss or contamination of product, reduction in efficiency and costly maintenance across many industries. Moreover, failure of critical metal parts is not just expensive, but potentially dangerous. Passivating and protective coatings comprise a widely applied approach to improve the surface properties of substrates and to protect materials from environmental degradation. To this aim, efficiently separating the substrate from the external environment is one of the most critical functions of a protective coating.

The hexagonal lattice of defect-free monolayer graphene has been proved both theoretically and experimentally to be impermeable to all liquids and gases including the smallest molecules, hydrogen and helium.[2–4] This outstanding feature has led to an enormous interest in employing graphene as an anticorrosion coating for metals and alloys.[5–7] Nevertheless, chemical vapour deposited (CVD) monolayer graphene generally exhibits defects through which molecules and radical species can diffuse, thus locally initiating metal corrosion.[8–10] In addition, it has been reported that once these local corrosion processes begin to take place underneath a monolayer graphene cover, they are actually even accelerated by the presence of graphene itself.[11] In this context, using a film made of several layers instead of a monolayer is one logical approach to improve performance of graphene-based protective coatings.[12–14] In this work, however, we report a so far unnoticed issue related to coatings with low permeability and high structural integrity. Indeed, when nickel coated with a thick, high-quality multilayered graphene is immersed in an acidic solution, the cathodic reaction spontaneously yields hydrogen at the nickel surface. The formed gas is not able to escape the high quality regions of the graphene film and therefore remains trapped and eventually forms bubbles, which can even lead to the delamination of the whole coating.

Technical University of Denmark, Department of Micro- and Nanotechnology, Kgs. Lyngby, DK-2800, Denmark. E-mail: lcam@nanotech.dtu.dk

† Electronic supplementary information (ESI) available: Polarization curves, electrochemical impedance spectroscopy, further Raman characterizations of the coating and the video of the real-time microscope experiments. See DOI: 10.1039/c6ra01556e

Experimental

Growth, transfer and characterization of MLG

Nickel foil (part no. 12722 from Alfa Aesar) was acetone ultrasonicated before graphene growth. Atmospheric pressure CVD growth was conducted with an AS-ONE CVD system from Annealsys. After loading the samples into the growth chamber, the chamber was evacuated with a rotary pump and then flushed with Ar three times before finally filling it up to atmospheric pressure. Next, the samples were heated at 950 °C for 15 min under the co-flow of 120 sccm and 100 sccm of Ar and H_2, respectively. The growth process was then carried out for 5 min at 950 °C with 2 sccm C_2H_2 and 100 sccm H_2. Lastly, the chamber was cooled down with a rate of 20 °C s^{-1} after the pressure was pumped down below 5 mbar.

Transfer of graphene coating onto glass slide or ~88 nm SiO_2 wafer was carried out *via* chemical etching of nickel in 5% HCl and 30% H_2O_2 mixed solution for 24 hours.

Optical images were taken with a Nikon Eclipse L200N optical microscope, while Raman spectra were collected by

a Thermo Fisher Scientific DXR Raman microscope (excitation wavelength 455 nm). Quanta 200 FEG environmental scanning electron microscope (SEM) and FEI Titan T20 G2 transmission electron microscope (TEM) were employed for the electron microscopy characterizations.

Electrochemical measurements

Polarization curves and electrochemical impedance spectroscopy (EIS) measurements were carried out with a three-electrode cell, using a AgCl/Ag reference electrode, a Pt foil as a counter electrode and a working electrode of tested samples, with a solution of 0.5 M HCl (aq) being the electrolyte. All measurements were repeated on three samples in a Faraday cage using a Gamry Reference 3000 potentiostat. Polarization curves were obtained after one hour of immersion by sweeping the potential from −300 mV to 300 mV *vs.* the open circuit potential (OCP) with a scan rate of 0.5 mV s^{-1}. EIS spectra were collected by applying a ±10 mV sinusoidal perturbation (*vs.* OCP) on tested samples at a frequency range from 100 000 Hz to 0.01 Hz with 10 points per decade.

Real-time microscopy experiments of hydrogen formation below the MLG coating

The *real-time* microscopy experiments were performed with a Nikon Eclipse L200N optical microscope and a Helios Nano Lab electron microscope. In both cases, the samples were exposed to 0.5 M HCl (aq) solution. The reader can refer to the next paragraph for more details of the performed *real-time* experiments.

Results and discussion

Fig. 1a reports an example of the bare nickel foil and the nickel foil coated with a CVD grown multilayered graphene (MLG) film, which have been the subject of this study. The MLG film is hydrophobic with a measured static water contact angle of 102.0° ± 0.4°, and floats as a monolithic piece on water after nickel being chemically etched (Fig. 1b), even though it is more than twice as dense as water. Raman spectroscopy provides information about the stacking order of the MLG[15] film and the density of defects.[16] For our samples, we find both AB-stacked and turbostratic regions (blue and red curve in Fig. 1c, respectively), with a higher prevalence of the former case, as expected for CVD graphene.[17] Regarding defect density, the small D-peak to G-peak ratio (0.040 ± 0.010) is the hallmark of the high quality film in terms of structural defects. X-ray diffraction analysis reveals an average interlayer distance of ~3.3 Å (See ESI†). The cross-sectional transmission electron micrograph (TEM) displayed in Fig. 1d gives insight into the total thickness of the MLG film (around 100 nm) and highlights the constant interlayer distance of the film, as shown by the Fourier transform displayed in the inset.

Nickel and its alloys are usually corrosion resistant in neutral, alkaline and diluted acidic media, while they deteriorate in aerated aggressive acidic environment. Hence, to investigate the corrosion performance of MLG coatings on nickel, we

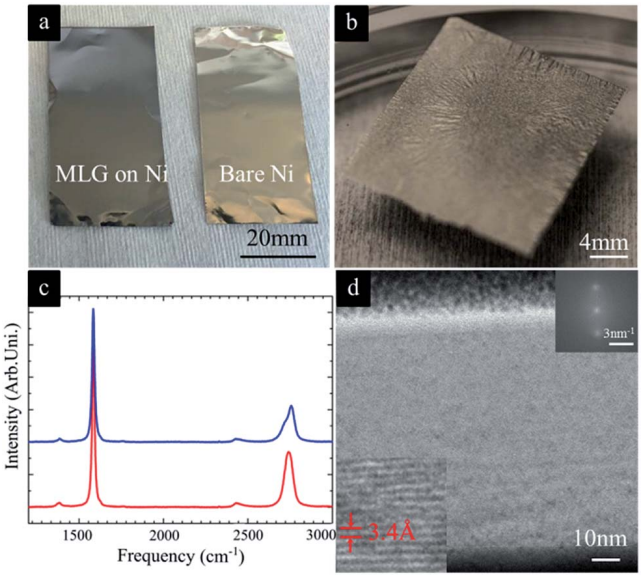

Fig. 1 (a) Multilayer graphene-coated (on the left) and bare (on the right) nickel foils. (b) Snapshot of the graphitic membrane floating on water after nickel substrate being chemically etched. (c) Two typical Raman spectra of the graphitic film showing the coexistence of regions with AB-stacking (top, blue curve) and turbostratic stacking (bottom, red curve). (d) Cross-section transmission electron microscope micrograph of the graphitic film on Ni foil. Insets: Fourier transform (top right corner) and high-resolution image (bottom left corner) both illustrating the high graphitization degree of the MLG film.

employ standard potentiodynamic polarization technique in 0.5 M HCl solution (pH = 0.3). With this method, by sweeping potential from negative to positive values with respect to the open circuit potential, the sample is electrochemically polarized, which allows us to obtain information about thermodynamics (*i.e.*, corrosion potential) and kinetics (*i.e.*, corrosion current density and corrosion rate) of the corrosion process.[18] Here, we estimate that the corrosion rate for the MLG-coated nickel is less than half that of the bare nickel specimen (see ESI† for more details). This trend is also confirmed by electrochemical impedance spectroscopy analysis (see ESI†) and is in agreement with previous studies on coatings based on few-layer graphene on nickel.[19] During the test, as expected, we could notice formation of hydrogen bubbles on the surface of both samples at the cathodic branch of the polarization curves (Fig. 2a), according to the reduction reaction:

$$2H_3O^+(aq) + 2e^- \rightarrow H_2(g) + 2H_2O(aq) \quad (1)$$

We further investigated the specimen surface by means of scanning electron microscopy (SEM). In Fig. 2b we report an example of an area where the MLG coating was locally delaminated. The approximately circular shape of the hole in the coating suggests that it has been caused upon rupture of a hydrogen bubble. However, the outward direction of the remaining MLG flakes at the surface near the edges of the hole suggests that the bubble was not located on the surface of the

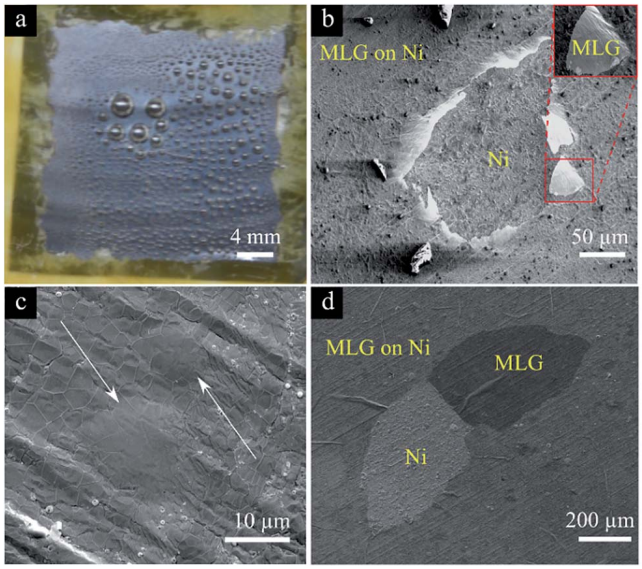

Fig. 2 (a) Snapshot of the MLG-coated nickel sample while being tested by potentiodynamic scanning at negative applied voltage (cathodic branch). Hydrogen bubbles can be observed on the surface of the sample. (b) SEM micrograph of the MLG-coated nickel foil after potentiodynamic scanning. At the center of the picture, the coating has been delaminated probably by a bursting hydrogen bubble; broken edges of the coating are now pointing outwards, suggesting that the burst bubble was located at the coating/substrate interface (inset). (c) SEM image of two bubbles – highlighted by the white arrows – found under the coating after applying constant negative potential (−0.6 V *vs.* Ag/AgCl) for 3 min to the MLG-coated nickel foil in 0.5 M HCl solution. (d) A portion of the MLG coating has been delaminated after 30 min of constant exposure to a potential of −0.6 V in 0.5 M HCl solution and still lies on the sample surface.

coating, but rather at the interface between it and the nickel substrate.

The formation of hydrogen bubbles at the interface between coating and substrate in aggressive acid environment is a known phenomenon in corrosion science.[20,21] Also, it is worth reminding that, though under different conditions, the evolution of hydrogen bubbles at the interface between graphene and metal substrate during the cathodic reaction is a method largely used for graphene transfer.[22]

To investigate whether the hydrogen bubbles are being generated both at the surface of the MLG film and underneath, we applied a fixed negative potential (−0.6 V *vs.* Ag/AgCl) to the coated nickel sample in 0.5 M HCl solution for only a short period of time (3 min). In this way, the bubbles can be observed at the interface before they become large enough to burst. As soon as the potential was applied, numerous hydrogen bubbles appeared at the surface of the coating. After this test, the sample was rinsed with water and gently blow-dried with nitrogen. Under the optical microscope, a few nearly circular protrusions of approximately 20 μm in diameter were found at seemingly un-correlated locations under the graphitic film. To prove that these protrusions are actually blisters, *i.e.* trapped gas underneath the graphene film and not particles or contaminants present on the surface, we characterized these structures by scanning electron microscopy. Fig. 2c displays two such protrusions that indeed seem to be blisters of the coating. Notably, the characteristic graphene wrinkles[23] at the base of the blisters gradually unfold near the center of the blister, as would be expected. To demonstrate that these blisters can become large enough to burst and locally delaminate the coating, we apply a fixed negative potential (−0.6 V *vs.* Ag/AgCl) to the coated nickel sample in 0.5 M HCl solution for 30 min. As displayed in Fig. 2d, SEM analysis shows that in many places, the coating is no longer covering the metal substrate, similar to what was found after the potentiodynamic scan experiment, which is another indication that the film has now ruptured and delaminated. Raman spectroscopy was also used to prove that no graphene is present in the delaminated areas (see ESI†).

Raman spectroscopy is also known to provide information regarding mechanical stress in the graphene lattice. A significant blue-shift of all the peaks in the spectrum has been indeed reported for the case of micro-balloons made of single and bi-layer graphene on a oxidized silicon substrate.[24] However, within our samples, we do not observe any remarkable shift of the peaks in the Raman spectra either recorded at the center of the blister, at its base, or away from the blister on a flat graphene region (see ESI†). This can be understood looking at Fig. 2c, where the wrinkles seem to unfold at the center of the blister, thereby relieving any stress caused by the trapped hydrogen. The wrinkles are naturally formed upon cooling after the growth process as a consequence of the different thermal expansion coefficients of graphene and nickel;[23] likewise the unfolding of wrinkles is a way to release the mechanical stress caused by the formation of the blisters.

To gain more insights into the formation of the hydrogen bubbles below the MLG film, we set up two experiments for real-time monitoring of the process. The first experiment consists of placing a droplet of 0.5 M HCl solution in the center of the MLG-coated Ni foil under an optical microscope. Already after 5 min, few blisters can be seen randomly distributed over the imaged area, initially with diameters ranging from 10 μm to 20 μm (Fig. 3a). These blisters grow over time due to a build-up of hydrogen at the interface between nickel and the coating until they eventually start to merge. This behavior continues as long as the HCl droplet is present on top of the MLG film. After two hours the blisters can be larger than 100 μm and locally lift up the coating (Fig. 3a). It is worth noticing that the time scale for hydrogen bubble formation actually varies depending on the sample under study. Interestingly, once the acid droplet is removed, the region of the sample under the droplet does not seem to be visibly corroded, *i.e.* there is no noticeable change in color or appearance. On the other hand, the region of the sample surrounding the droplet, which is thus not in immediate contact with the acid, exhibits remarkable signs of degradation (see Fig. 3b and c, respectively). If the acid is distributed all over the sample area, the blisters eventually cause delamination of the whole coating (see ESI†).

In the second experiment, SEM is used in order to study the hydrogen bubble formation in real-time with higher spatial resolution. A droplet of 0.5 M HCl solution is placed in the center of the MLG-coated nickel foil, and gently removed with a tissue.

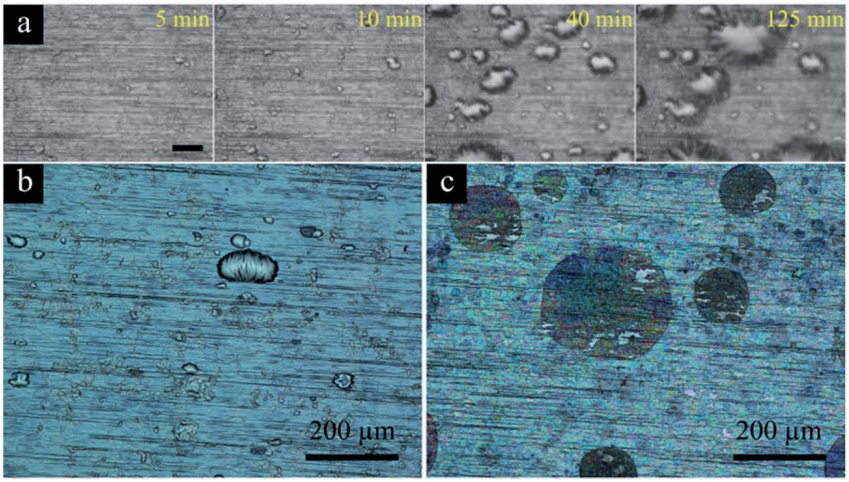

Fig. 3 (a) Sequence of optical microscope images taken from a MLG-coated nickel foil with a droplet of 0.5 M HCl solution on top. The pictures are recorded through the acid droplet – hence the low quality of the images. The scale bar is 100 μm. (b and c) Optical images of an area under the acid droplet (c) and away from it (c). The sample represented in (a) is different from the one reported in (b) and (c).

The sample is mounted inside the scanning electron microscope without prior rinsing or blow-drying. When the electron beam is focused on a flat region of the sample, a dramatic hydrogen evolution takes place below the MLG film (Fig. 4).

At first, a single micrometer-size blister is observed, then, other smaller blisters are formed all over the scanned area (Fig. 4b and c, respectively). At lower magnification, it is possible to see that the blister-like protrusions are mainly found in the area that was initially irradiated by the scanning electron beam (see ESI†). This might be explained by a monolayer of the acidic solution still being adsorbed on the surface[25] as well as within defects and crevices of the MLG film after the sample has being placed inside the microscope and evacuated. Then, the local heating and the creation of defects[26] induced by the electron beam trigger and accelerate the diffusion of water through the MLG coating thus giving rise to the hydrogen bubble formation. This experiment points out that (i) the fact that such gas evolution only occurs with samples that have been exposed to HCl solution rules out that this phenomenon is caused by the presence of residual gas trapped either between graphene and nickel or into the nickel itself during the CVD process; and (ii) the trapping of gas at the graphene–metal interface in vacuum conditions inside the SEM chamber indicates that the overall quality and integrity of the film is high, as also corroborated by Raman spectroscopy investigation (see Fig. 1c).

To explain why hydrogen is formed at the interface, we suggest that, even if few, local defects and inhomogeneities are intrinsically present in the coating. Notably, such inhomogeneities are areas with higher defect density, grain boundaries,[27,28] and sometimes also fewer layers (see ESI†). These areas may originate from local impurities on the nickel surface, temperature gradients during the synthesis process or different catalytic activity of the nickel grains, as already reported in the literature for CVD grown multilayer graphene.[29] In this scenario, as the coating is placed in contact with the acidic solution, water fills these defects and inhomogeneities thus forming a bridge which allows protons to shuttle from outside the coating to the nickel surface, through the hydrogen-bonding network (Fig. 5), similar to the case of proton transport through the channel of carbon nanotubes.[30,31] As water reaches the nickel, the cathodic reaction locally takes place. In fact, as described by the potential-pH diagram of nickel/water system, also known as Pourbaix diagram,[32] the evolution of hydrogen at the nickel–water interface is spontaneous at the low pH level used in this study. As the MLG coating on nickel shifts the open circuit potential of nickel by only −25 mV (see ESI†), the hydrogen evolution process for the MLG-coated nickel is still spontaneous, in accordance with our observations. Once hydrogen is formed at the coating-metal interface, we can assume it diffuses on the nickel surface, as observed in similar systems,[33] and

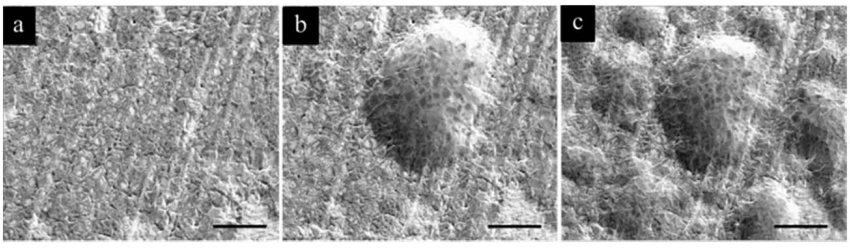

Fig. 4 Consecutive SEM micrographs recorded on a MLG-coated nickel foil after a droplet of 0.5 M HCl has been placed on top and subsequently removed. The formation of hydrogen blisters over time is reported. The scale bar is 20 μm.

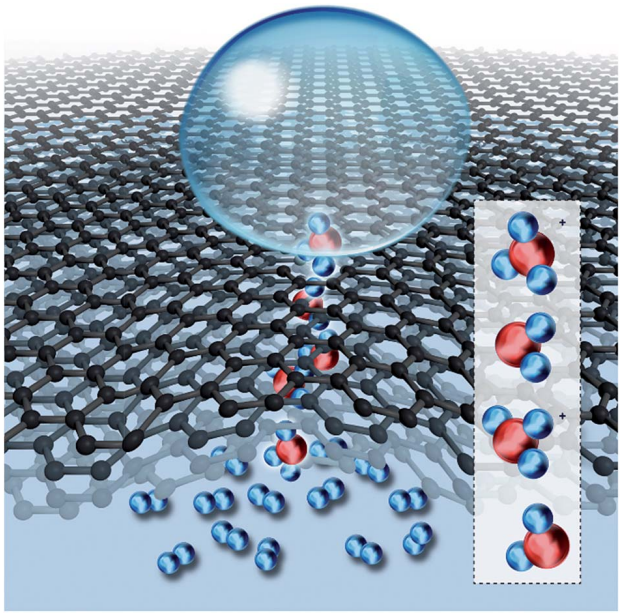

Fig. 5 Drawing of the proposed mechanism for hydrogen formation under a droplet of 0.5 M HCl solution. Once the solution reaches the nickel surface through defective areas in the coating, protons – which are carried by water molecules *via* the Grotthuss mechanism, jumping from a molecule to the next one (inset) – are spontaneously reduced to hydrogen. The red balls represent oxygen atoms, while the blue balls stand for hydrogen atoms.

merge, thus giving rise to the observed blisters. Since the majority of the coating is made of regions with very small apparent density of defects, a build-up of hydrogen occurs under the MLG film, produces bubbles that grow and merge, and eventually delaminate the coating. The formed hydrogen is not likely to pass through the coating *via* local defects and inhomogeneities, since these are clogged by water molecules, as previously suggested for helium-leak-tight coatings made of graphene oxide.[34] The fact that the formation of hydrogen bubbles takes place on a different time scale depending on the sample under study could be explained by varying density of inhomogeneous areas within the coating, which is easily accountable by variations of the nickel foil substrates or inevitable differences in the exact growth conditions commonly experienced for CVD graphene growth. Here, it is worth pointing out that proton transport through a defect-free single layer of graphene has already been observed, but not through a bilayer.[35] In this study we report on the performance of a coating comprised of hundreds of graphene layers, and therefore cannot immediately adopt the explanation proposed by Hu and co-workers,[35] where a tunnel mechanism was invoked.

The dramatic degradation of the sample in the regions surrounding the acid droplets can be ascribed to the formation of a galvanic cell between nickel and graphene. Every electrochemical reaction consists of a cathodic and an anodic part. In the case of the acid droplet deposited on the middle of the MLG-coated sample, the cathodic reaction (*i.e.*, reduction of protons to hydrogen) occurs under the droplet due to the abundance of

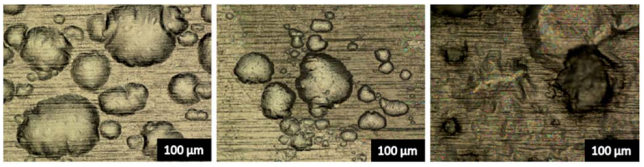

Fig. 6 Optical micrograph of three MLG-coated nickel foils exposed for 240 min to 0.5 M HCl (left picture), 0.5 M H_2SO_4 (center picture) and 0.5 M HNO_3 (right picture). In all cases, the MLG coating has been lifted in several areas due to evolution of hydrogen at the nickel-coating interface.

protons, while the anodic one (*i.e.*, oxidation of the nickel) takes place away from the droplet. While reducing protons to hydrogen, electrons are being continuously depleted in the region under the droplets. In this picture, electrons will move from the region surrounding the droplet, to the region below the droplet in compensation. Here, as already reported in the case of single layer graphene grown on copper foil,[11] the electrons may migrate through the graphene film due to its high conductivity, rather than through the passivated metal surface, thus giving rise to formation of a galvanic cell which spreads the oxidation of nickel to all regions in contact with graphene.

Ultimately, in order to verify that the formation of hydrogen beneath a graphene coating is a reaction occurring spontaneously in the system nickel/water at low pH values, regardless of the anions that are present in solution, we repeat the experiment of the droplet placed at the center of the coated substrate using different acids. At this aim, a MLG-coated nickel foil is cut into three pieces. The first piece is tested with HCl, the second one with H_2SO_4 whereas the third one with HNO_3, all solutions being at the same concentration (namely 0.5 M). As displayed in Fig. 6, after 240 min of exposure, the coating results in being lifted up in several areas by hydrogen in all the three cases, regardless of the acids that was used.

Conclusions

Our observations show that protective coatings based on CVD MLG might fail in certain chemical environments. Even for MLG consisting of hundreds of layers, with nominally very few defects, the few but inevitable inhomogeneities provide sufficient pathways for acid to reach the Ni surface, where hydrogen is spontaneously formed. We suggest that the very integrity and quality of the MLG coating prevents excess gas to escape at a rate that matches the rate of which it is formed, which thus leads to hydrogen build-up and eventually catastrophic delamination to the coating. This implies that coatings based on graphene and other two-dimensional materials, which are considered attractive for corrosion protection due to their impermeability, may fail for the same reason. Notably, the vulnerability to gas evolution below the coating may become increasingly severe as the thickness, quality and homogeneity of the coating is improved, as this will prevent gas from escaping in a non-destructive manner. Our findings may be relevant for

other electrochemically active metals and alloys made for instance of iron, zinc, manganese and aluminium.

On the other hand, however, it is also worth pointing out that (i) the possibility of spontaneously producing and effectively trapping hydrogen (or other gases) calls for further investigations of such MLG film in fields such as gas storage and production; and (ii) the capability of such membranes of being selectively permeable to water might be of great interest for particular environmental applications.[36]

Acknowledgements

The authors are grateful to Dr Rahul Raveendran Nair and Jijo Abraham for providing the XRD data and for the useful discussions. The authors also thank Dr David Mackenzie for help with the analysis of Raman data. This project was supported by The Strategic Danish Research collaboration (DSF) with the DA-GATE project (12-131827) and through the high technology foundation (HTF) with the NIAGRA project (058-2012-4). L. C. thanks funding support from The Danish Council for Independent Research | Technology and Production Sciences (FTP) through the Mobilex grant 'Atomically thin coatings'.

Notes and references

1 A. El-Meligi, *Recent Pat. Corros. Sci.*, 2010, **2**, 22–33.
2 J. S. Bunch, S. S. Verbridge, J. S. Alden, A. M. van der Zande, J. M. Parpia, H. G. Craighead and P. L. McEuen, *Nano Lett.*, 2008, **8**, 2458–2462.
3 O. Leenaerts, B. Partoens and F. M. Peeters, *Appl. Phys. Lett.*, 2008, **93**, 193107.
4 M. Miao, M. B. Nardelli, Q. Wang and Y. Liu, *Phys. Chem. Chem. Phys.*, 2013, **15**, 16132–16137.
5 S. Chen, L. Brown, M. Levendorf, W. Cai, S.-Y. Ju, J. Edgeworth, X. Li, C. W. Magnuson, A. Velamakanni and R. D. Piner, *ACS Nano*, 2011, **5**, 1321–1327.
6 D. Prasai, J. C. Tuberquia, R. R. Harl, G. K. Jennings and K. I. Bolotin, *ACS Nano*, 2012, **6**, 1102–1108.
7 N. T. Kirkland, T. Schiller, N. Medhekar and N. Birbilis, *Corros. Sci.*, 2012, **56**, 1–4.
8 D. L. Duong, G. H. Han, S. M. Lee, F. Gunes, E. S. Kim, S. T. Kim, H. Kim, Q. H. Ta, K. P. So, S. J. Yoon, S. J. Chae, Y. W. Jo, M. H. Park, S. H. Chae, S. C. Lim, J. Y. Choi and Y. H. Lee, *Nature*, 2012, **490**, 235–239.
9 I. Wlasny, P. Dabrowski, M. Rogala, P. J. Kowalczyk, I. Pasternak, W. Strupinski, J. M. Baranowski and Z. Klusek, *Appl. Phys. Lett.*, 2013, **102**, 111601.
10 Y.-P. Hsieh, M. Hofmann, K.-W. Chang, J. G. Jhu, Y.-Y. Li, K. Y. Chen, C. C. Yang, W.-S. Chang and L.-C. Chen, *ACS Nano*, 2013, **8**, 443–448.
11 M. Schriver, W. Regan, W. J. Gannett, A. M. Zaniewski, M. F. Crommie and A. Zettl, *ACS Nano*, 2013, **7**, 5763–5768.
12 N.-W. Pu, G.-N. Shi, Y.-M. Liu, X. Sun, J.-K. Chang, C.-L. Sun, M.-D. Ger, C.-Y. Chen, P.-C. Wang, Y.-Y. Peng, C.-H. Wu and S. Lawes, *J. Power Sources*, 2015, **282**, 248–256.
13 A. C. Stoot, L. Camilli, S.-A. Spiegelhauer, F. Yu and P. Bøggild, *J. Power Sources*, 2015, **293**, 846–851.
14 Y. Su, V. G. Kravets, S. L. Wong, J. Waters, A. K. Geim and R. R. Nair, *Nat. Commun.*, 2014, **5**, 4843.
15 R. Rao, R. Podila, R. Tsuchikawa, J. Katoch, D. Tishler, A. M. Rao and M. Ishigami, *ACS Nano*, 2011, **5**, 1594–1599.
16 A. Eckmann, A. Felten, A. Mishchenko, L. Britnell, R. Krupke, K. S. Novoselov and C. Casiraghi, *Nano Lett.*, 2012, **12**, 3925–3930.
17 A. W. Tsen, L. Brown, R. W. Havener and J. Park, *Acc. Chem. Res.*, 2013, **46**, 2286–2296.
18 C. Lefrou, R. P. Nogueira, F. Huet and H. Takenouti, in *Shreir's Corrosion*, Elsevier, Oxford, 2010, pp. 13–51.
19 X. H. Ye, F. Yu, M. Curioni, Z. Lin, H. J. Zhang, H. W. Zhu, Z. Liu and M. L. Zhong, *RSC Adv.*, 2015, **5**, 35384–35390.
20 M. L. White, H. Vedage, R. D. Granata and H. Leidheiser Jr, *Ind. Eng. Chem. Res.*, 1986, **25**, 129–132.
21 H. Leidheiser Jr and M. W. Kendig, *Ind. Eng. Chem. Res.*, 1978, **17**, 54–55.
22 L. Gao, W. Ren, H. Xu, L. Jin, Z. Wang, T. Ma, L.-P. Ma, Z. Zhang, Q. Fu and L.-M. Peng, *Nat. Commun.*, 2012, **3**, 699.
23 S. J. Chae, F. Güneş, K. K. Kim, E. S. Kim, G. H. Han, S. M. Kim, H.-J. Shin, S.-M. Yoon, J.-Y. Choi, M. H. Park, C. W. Yang, D. Pribat and Y. H. Lee, *Adv. Mater.*, 2009, **21**, 2328–2333.
24 J. Zabel, R. R. Nair, A. Ott, T. Georgiou, A. K. Geim, K. S. Novoselov and C. Casiraghi, *Nano Lett.*, 2012, **12**, 617–621.
25 D. Chakarov, L. Österlund and B. Kasemo, *Vacuum*, 1995, **46**, 1109–1112.
26 J. Jones, P. Ecton, Y. Mo and J. Perez, *Appl. Phys. Lett.*, 2009, **95**, 246101.
27 S. C. O'Hern, C. A. Stewart, M. S. Boutilier, J.-C. Idrobo, S. Bhaviripudi, S. K. Das, J. Kong, T. Laoui, M. Atieh and R. Karnik, *ACS Nano*, 2012, **6**, 10130–10138.
28 M. S. Boutilier, C. Sun, S. C. O'Hern, H. Au, N. G. Hadjiconstantinou and R. Karnik, *ACS Nano*, 2014, **8**, 841–849.
29 A. Reina, X. Jia, J. Ho, D. Nezich, H. Son, V. Bulovic, M. S. Dresselhaus and J. Kong, *Nano Lett.*, 2009, **9**, 30–35.
30 C. Dellago, M. M. Naor and G. Hummer, *Phys. Rev. Lett.*, 2003, **90**, 105902.
31 D. J. Mann and M. D. Halls, *Phys. Rev. Lett.*, 2003, **90**, 195503.
32 M. Pourbaix and R. W. Staehle, in *Lectures on Electrochemical Corrosion*, Springer, 1973, pp. 83–183.
33 E. Stolyarova, D. Stolyarov, K. Bolotin, S. Ryu, L. Liu, K. Rim, M. Klima, M. Hybertsen, I. Pogorelsky and I. Pavlishin, *Nano Lett.*, 2008, **9**, 332–337.
34 R. Nair, H. Wu, P. Jayaram, I. Grigorieva and A. Geim, *Science*, 2012, **335**, 442–444.
35 S. Hu, M. Lozada-Hidalgo, F. C. Wang, A. Mishchenko, F. Schedin, R. R. Nair, E. W. Hill, D. W. Boukhvalov, M. I. Katsnelson, R. A. Dryfe, I. V. Grigorieva, H. A. Wu and A. K. Geim, *Nature*, 2014, **516**, 227–230.
36 F. Perreault, A. Fonseca de Faria and M. Elimelech, *Chem. Soc. Rev.*, 2015, **44**, 5861–5896.

Appendix C

Publication 6

(12) INTERNATIONAL APPLICATION PUBLISHED UNDER THE PATENT COOPERATION TREATY (PCT)

(19) World Intellectual Property Organization
International Bureau

(43) International Publication Date
4 February 2016 (04.02.2016)

WIPO | PCT

(10) International Publication Number
WO 2016/016214 A1

(51) International Patent Classification:
G01N 27/28 (2006.01) *G01N 17/02* (2006.01)

(21) International Application Number:
PCT/EP2015/067215

(22) International Filing Date:
28 July 2015 (28.07.2015)

(25) Filing Language: English

(26) Publication Language: English

(30) Priority Data:
14178928.9 29 July 2014 (29.07.2014) EP

(71) Applicant: **DANMARKS TEKNISKE UNIVERSITET** [DK/DK]; Anker Engelundsvej 1, Bygning 101 A, 2800 Kgs. Lyngby (DK).

(72) Inventors: **STOOT, Adam C**; Eddagården 3, 3. th, 2200 København N (DK). **BIRNEY, Ross**; 3 Locher Crescent, Houston, Renfrewshire PA6 7NW (GB). **BOOTH, Timothy John**; Grønnevej 55, 3. th., 2830 Virum (DK).

(74) Agent: **HØIBERG A/S**; St. Kongensgade 59 A, 1264 Copenhagen K (DK).

(81) Designated States *(unless otherwise indicated, for every kind of national protection available)*: AE, AG, AL, AM, AO, AT, AU, AZ, BA, BB, BG, BH, BN, BR, BW, BY, BZ, CA, CH, CL, CN, CO, CR, CU, CZ, DE, DK, DM, DO, DZ, EC, EE, EG, ES, FI, GB, GD, GE, GH, GM, GT, HN, HR, HU, ID, IL, IN, IR, IS, JP, KE, KG, KN, KP, KR, KZ, LA, LC, LK, LR, LS, LU, LY, MA, MD, ME, MG, MK, MN, MW, MX, MY, MZ, NA, NG, NI, NO, NZ, OM, PA, PE, PG, PH, PL, PT, QA, RO, RS, RU, RW, SA, SC, SD, SE, SG, SK, SL, SM, ST, SV, SY, TH, TJ, TM, TN, TR, TT, TZ, UA, UG, US, UZ, VC, VN, ZA, ZM, ZW.

(84) Designated States *(unless otherwise indicated, for every kind of regional protection available)*: ARIPO (BW, GH, GM, KE, LR, LS, MW, MZ, NA, RW, SD, SL, ST, SZ, TZ, UG, ZM, ZW), Eurasian (AM, AZ, BY, KG, KZ, RU, TJ, TM), European (AL, AT, BE, BG, CH, CY, CZ, DE, DK, EE, ES, FI, FR, GB, GR, HR, HU, IE, IS, IT, LT, LU, LV, MC, MK, MT, NL, NO, PL, PT, RO, RS, SE, SI, SK, SM, TR), OAPI (BF, BJ, CF, CG, CI, CM, GA, GN, GQ, GW, KM, ML, MR, NE, SN, TD, TG).

Declarations under Rule 4.17:

— *of inventorship (Rule 4.17(iv))*

Published:

— *with international search report (Art. 21(3))*

— *before the expiration of the time limit for amending the claims and to be republished in the event of receipt of amendments (Rule 48.2(h))*

WO 2016/016214 A1

(54) Title: WORKING ELECTRODE HOLDER AND ELECTROCHEMICAL CELL

(57) Abstract: The present disclosure relates to a holder for a test object, more specifically to a holder for measuring electrochemical properties of the test object. One embodiment relates to a working electrode holder for measuring electrochemical properties of a front surface of a test object in a liquid, comprising: a housing comprising a bottom surface and a sidewall, the sidewall defining a first opening such that the test object can be placed inside the housing via the first opening and such that the front surface is facing the inner bottom surface; one or more electrically conductive pin(s) fixed to the bottom surface inside the housing such that the front surface of the test object is able to be placed on the pin(s), thereby providing an electrically contacted front surface, such that the electrically contacted front surface is able to operate as the working electrode; a second opening located in the bottom surface and configured for passage of said liquid, such that liquid is able to pass onto the electrically contacted front surface. The holder may be used in an electrochemical cell.

Working electrode holder and electrochemical cell

Field of invention

The present disclosure relates to a holder for a test object, more specifically to a holder for measuring electrochemical properties of the test object. The holder may be used in an electrochemical cell.

Background of invention

Electrochemical experiments are generally conducted using a two- or three-electrode setup. Such setups comprise a working electrode, which is the test object or material under investigation; a counter electrode, made of an inert material, which needs to be stable and unreactive under the conditions used within the electrochemical cell (hence, platinum or graphite are often used); and, optionally, a reference electrode, which takes no part in the electrochemical reaction(s) under investigation and provides a stable and known reference potential. All the electrodes are placed in electrical contact with the electrolyte of an electrochemical cell, i.e. the electrodes are in a container with a liquid electrolyte. The potentials and resulting electrical currents of the reactions of interest are measured with respect to this reference potential (voltammetry).

The three electrodes are connected to a potentiostat, which is an electronic instrument that controls the voltage difference between the working electrode and reference electrode. Many potentiostats are capable of other measurements as well, in which they might control and/or measure the current over time between the counter and working electrodes whilst controlling and/or measuring the voltage with respect to the reference (chronoamperometry, chronopotentiometry).

To be able to accurately measure the electrochemical properties of a test object, the area exposed to the chosen electrolyte must be known, as the surface current density is more important than the absolute value of the current. The test object should also be contacted to the potentiostat in such a way that any electrically conductive or chemically reactive parts beyond the working electrode surface (such as wiring, soldering and crocodile clips) do not come into contact with the electrolyte and affect the measurements via corrosion, reaction with the electrolyte or short circuit, and interfere with the measurement.

Measuring the electrochemical properties of a test object, including measuring corrosion, is typically done in a cell, which often takes the form of an open-ended vessel or tube, with one end of the cell accommodating an O-ring. The test object can then be placed in mechanical contact with the O-ring, typically with the front side facing the O-ring, and screws or clamps can be tightened to hold the test object in contact with the O-ring. The backside of the test object can then be connected to a potentiostat using e.g. soldering or crocodile clips. After fixing the test object in place, the test object forms a liquid tight seal at one end of the cell, which can then be filled with electrolyte. The two remaining electrodes are immersed in the electrolyte and experiments can thereby be conducted. An open ended tube, wherein a test object is placed such that the back surface of the test object is connected using alligator clips, is disclosed in the instruction manual for the Model K0070 Corrosion Cell System from Princeton Applied Research.

There are many problems in measuring electrochemical properties of a test object according to above described devices and method. First of all, the insertion and fixation of the test object is difficult. Secondly, the establishment of electrical contact to the test object is provided by means of a rather complicated procedure. Thirdly, the electrical connection contacts the back side of the test object, such that it may be difficult to work with coated materials and other test objects that may contain an insulating layer or coating. Examples of electrical contact established to a backside of a test-object and where liquid is in contact with the front side only, are disclosed in WO 2014/008942 and GB 2 168 161. Finally, in most electrochemical cells it is necessary to empty the electrolyte from the cell when exchanging the test sample, because the sample is an integrated part of the cell. GB 2 168 161 is an example of this. This increases the likelihood of introducing contamination or other inconsistencies when emptying and replacing the electrolyte for further or repeated experiments.

Summary of invention

It is desirable to have a system whereby the test object functioning as the working electrode is easily interchangeable, in order to make multiple measurements and measurement of different materials under the same conditions simpler and to remove the need to form a permanent or semi-permanent connection to the material using solder, conductive paints, or epoxy, etc. For some applications it is also desirable to have an electrical connection to the front side of the test object. This makes it possible to work with coated materials and materials with heterogeneous electrical

characteristics through their thickness – such samples may contain a highly insulating layer or coating which would interfere with or prevent accurate measurement.

In order to solve the above described problems and provide a solution for the desired needs, the present disclosure provides a working electrode holder for measuring electrochemical properties of a front surface of a test object in a liquid, comprising: a housing comprising a bottom surface and a sidewall, the sidewall defining a first opening such that the test object can be placed inside the housing via the first opening and such that the front surface is facing the inner bottom surface; one or more electrically conductive pin(s) fixed to the bottom surface inside the housing such that the front surface of the test object is able to be placed on the pin(s), thereby providing an electrically contacted front surface, such that the electrically contacted front surface is able to operate as the working electrode; a second opening located in the bottom surface and configured for passage of said liquid, such that liquid is able to pass onto the electrically contacted front surface.

The working electrode holder according to the present disclosure may be inserted into an existing electrochemical vessel-which may simply consist of electrolyte in a beaker. The working electrode holder may contain the test object, but only a known area of the front side of the test object may be exposed to the electrolyte. The test object itself may be inserted into the working electrode holder according to the present disclosure while the electrochemical cell or beaker has already been prepared and filled with an electrolyte. The insertion of the test object into the working electrode holder according to the present disclosure is very simple; the test object may simply be put inside the working electrode holder by hand. By having the one or more electrically conductive pin(s) fixed to the bottom surface inside the housing such that the front surface of the test object is able to be placed on the pin(s), thereby providing an electrically contacted front surface, such that the electrically contacted front surface is able to operate as the working electrode, there is provided means for efficiently providing a working electrode. In other words, electrical contact can be established quickly to the front surface, and especially without soldering or attaching alligator clips.

The working electrode holder according to the present disclosure is intended to be used in electrochemical cells, in particular for corrosion experiments. Accordingly, the holder according to the present disclosure is intended to be placed inside an electrochemical cell or a beaker containing a liquid.

The working electrode holder according to the present disclosure, may contact the front side of the test object, i.e. the surface of the test object configured as working electrode may be the front side of the test object, making it possible to work with coated materials and other test object that may contain an insulating layer or coating.

An effect of the having the test object in the working electrode holder according to the present disclosure is that it makes it possible to keep the electrolyte in the cell and reuse it for further or repeat experiments.

An effect of having the pin(s) fixed to the bottom surface inside the housing is that the front surface of the test object is able to be positioned in contact with the one or more pin(s) such that an electrically conductive surface of the test object is facing the bottom surface of the housing. In this way, there may be established a good electrical contact in an efficient manner between the pin(s) and electrically conductive surface. Good mechanical contact to the sample may facilitate good electrical contact. The placement of the test object is as previously described via the first opening, and may allow for a placement and removal of the test object. Further, the test object may be easily and/or quickly placed into and/or removed from the holder. Another effect is that the liquid may be able to pass directly toward the electrically conductive surface of a test object facing the bottom surface of the housing, in particular because the second opening is placed at the bottom surface of the housing.

The pin(s) may be any suitable pin(s) that are electrically conductive, such as spring loaded pins.

The present disclosure is further related to an electrochemical cell for measuring electrochemical properties of a test object, comprising: a container containing a liquid; an electrode; and a working electrode holder as described in said liquid and with said test object in said holder.

Description of drawings

Fig. 1 shows an embodiment of the working electrode holder according to the present disclosure from a perspective.

Fig. 2 shows an embodiment of the housing according to the present disclosure from below.

Fig. 3 shows an embodiment of the housing according to the present disclosure from above.

Fig. 4 shows an embodiment of the housing according to the present disclosure from the side.

Fig. 5 shows an embodiment of the housing according to the present disclosure from a perspective.

Fig. 6 shows an embodiment of the housing according to the present disclosure from a perspective.

Fig. 7 shows an embodiment of the attachment means according to the present disclosure from the side.

Fig. 8 shows an embodiment of the attachment means according to the present disclosure from an end.

Fig. 9 shows an embodiment of the attachment means according to the present disclosure from a perspective.

Fig. 10 shows an embodiment of the holding means according to the present disclosure from the side.

Fig. 11 shows an embodiment of the holding means according to the present disclosure from the top.

Fig. 12 shows an embodiment of the holding means according to the present disclosure from a perspective.

Fig. 13 shows an embodiment of a spacer according to the present disclosure.

Detailed description

Housing and holding means

In one embodiment of the present disclosure, the housing is configured for containing said test object comprising a circular surface with a diameter of at least 2.5 cm, 5 cm, 7.5 cm, 10 cm, 12.5 cm or at least 15 cm in a plane parallel to the bottom surface inside the housing. In such configuration, the housing may be configured for containing a wafer with the standard measures such as 1”, 2”, 3”, 4”, 5” or 6”. However, in some embodiments, the housing is configured for containing said test object comprising a circular surface with a diameter of less than 2.5 cm.

In another embodiment of the present disclosure, the height of said side wall is at least 5mm, 10mm, 15mm, 20mm, 25mm, 30mm, 35mm, 40mm, 45mm, or at least 50mm.

In a preferred embodiment of the present disclosure, the housing is configured for providing electrical wiring to said pins. Accordingly, there may be one or more hole(s) going through the housing, such as through the sidewall or through the bottom surface. By having wiring to the pins, electrical connection is made to the front surface of the test object once the test object is placed inside the holder according to the present disclosure. In this sense, the electrical connection is automatically established and the user is not required to make the connection to the test object, for example by soldering a wire to the test object. Accordingly, the placement of the test object is easy and fast.

The housing may be any suitable shape, for example it may be shaped for a specific test object. Preferably, the cross section of the housing may be circular, square, rectangular or triangular.

Furthermore, the housing may be configured for receiving holding means for holding the test object in place between the pin(s) and said holding means. In a preferred embodiment, the holding means is a lid. The lid may be any suitable lid, for example it may be screwed or press fit into the first opening, thereby pressing the test object towards the pin(s). An effect of having holding means as described is that the holding means due to its pressure on the test object facilitate a good mechanical and electrical contact between the test object and the pin(s). Even further, the holding means may be configured to fit into said first opening, such that said liquid can only passage through the second opening. In this way, the second opening may face an electrically conducting surface of the test object, such that liquid may be directed directly onto the electrically conducting surface. All electrical contacts may be connected by placing the holding means in the first opening, for example, by screwing a lid, such that this is done using a single and simple movement. The holding means may facilitate that sealing and fixation of the test object is done easily as well.

In a preferred embodiment of the present disclosure, the housing and/or holding means are made of electrically insulating materials. In this regard, the working electrode holder according to the present disclosure may be completely free of metallic parts that can corrode (except the wires), and thus the working electrode holder according to the present disclosure is optimal for an environment comprising a liquid. Accordingly, the present disclosure is optimized for being used for corrosive test where the holder and the test object is placed in the liquid.

Additionally, the holding means may comprise an O-ring. Also, the bottom inner surface, such as the inner surface of the bottom, may comprise an O-ring.

Pins

In a preferred embodiment of the present disclosure, the pins are three pins placed equidistant from each other. More preferably, the pins are three pins placed equidistant from said second opening. The purpose of the pins may be to establish good electrical contact.

Spacer

In one embodiment of the present disclosure, there is a spacer that comprises one or more plate(s), to be placed between the test object and a lid to be inserted in the first opening.

In a preferred embodiment, the spacer is a facilitating that the test object is pushed further towards the pins such that a better contact is established.

Alternatively, the spacer may be integrated into a lid, e.g. as a part that can be adjusted with a screw-mechanism.

Test object

In one embodiment of the present disclosure, the test object is a composite of layers. All of the layers need not to be electrically conductive, and thus the test object may be a non-conducing test object, i.e. the test object may not be electrically conductive through all layers. An effect of the present disclosure is that the working electrode holder works with such non-conductive test objects. The test object may be a wafer or a wafer sample, in particular a multilayer wafer or wafer sample. The test object may comprise a circular surface with a diameter of at least a 1”, 2”, 3”, 4”, 5” or at least 6”. However, in some embodiments, the test object may comprise a circular surface with a diameter of less than 1”.

Attachment means

In a preferred embodiment of the present disclosure, the housing further comprises attachment means for attaching said working electrode holder to an attachment holder. In this way, it may be possible to place the working electrode holder inside an

electrochemical cell or beaker such that the attachment holder holds the working electrode holder at a given position inside the electrochemical cell or beaker.

In a more preferred embodiment of the present disclosure, the attachment means is a rod attached to said sidewall, such that said attachment means extends from an outer surface of said sidewall. The attachment means may be configured for providing electrical wiring to said pins, for example there may be a hole going through the attachment means, such as through a rod. The wiring may then be further connected to a device able to measure the electrochemical properties of the test object in electrical contact with the pins.

Further electrodes

In order to measure the electrochemical properties of the test object, a counter electrode is placed somewhere in the liquid. In one embodiment of the present disclosure, the housing or holding means or attachment means comprises one counter electrode.

Additionally, it may be required that there is a reference electrode in the liquid in order to measure the electrochemical properties of the test object. In another embodiment of the present disclosure, the housing or holding means or attachment means comprises one reference electrode.

Openings

Preferably, the second opening is positioned such that liquid can passage into a test area of said test object. For example, the second opening may be in the centre of said bottom surface. Alternatively, the second opening may be at an off-centre position. There may be one or more second openings. Accordingly, there may both be an opening at the centre of the bottom surface and/or at an off-centre, such as of the bottom surface and/or of the sidewall and/or of the lid. In some embodiments, there may be second openings, i.e. additional openings, the additional openings may be at the sidewall, at the holding means, or at the lid.

In one embodiment of the present disclosure, the second opening has an area of such as less than 10 cm^2, such as less than 9 cm^2, such as less than 8 cm^2, such as less than 7 cm^2, such as less than 6 cm^2, such as less than 5 cm^2, such as less than 4 cm^2, such as less than 3 cm^2, such as less than 1 cm^2, such as less than 1 cm^2. In some

embodiments, the second opening has an area of such as more than 10 cm^2, such as more than 20 cm^2, such as more than 30 cm^2, such as more than 40 cm^2, or such as more than 50 cm^2

Electrochemical cell

The electrochemical cell according to the present disclosure may comprise one or more of the described feature(s). The electrode may be a counter electrode and or a reference electrode attached to said working electrode holder. The counter electrode is essential for having an electrochemical cell according to the present disclosure, but as just described, the counter electrode may not need to be in the container but may be a part of the holder according to the present disclosure. Such configuration may simplify an electrochemical cell by collecting all the electric wires in one place, namely on the holder.

Examples

Fig. 1 shows an embodiment of the working electrode holder according to the present disclosure from a perspective. **Figure 1** shows a working electrode holder for measuring electrochemical properties of a test object in a liquid, comprising: a housing **1** comprising a bottom surface **2** and a sidewall **3**; one or more electrically conductive pin(s) **4** positioned on a bottom surface **5** inside the housing **1**; a second opening **6** configured for passage of said liquid; and a first opening **7** configured for receiving said test object such that a surface of the said object configured as working electrode can be placed in contact with said pin(s) **4** and liquid. The housing is configured for receiving holding means **8** for holding said test object in place between said pins and said holding means. In this case, the housing is with threading, and the holding means **8** is a lid, configured to fit into the housing. In order to tighten the lid, there is a groove on the lid. Further, the holding means **8** is configured to fit into said first opening **7**, such that said liquid can only passage through said second opening **6**. In this example, the housing is configured for containing the test object comprising a circular surface with a diameter of at least 2.5 cm in order hold a standardized1-inch test object in a plane parallel to said bottom surface **5** inside the housing. Accordingly, the cross section of said housing is circular. The second opening is in said bottom surface, specifically at the in the centre, positioned such that said liquid can passage into a test area of said test object. The housing further comprises attachment means **9** for attaching said working electrode holder to an attachment holder. The housing is configured for providing electrical wiring to said pins, and therefore there is a hole **10**

going through the sidewall **3**. The pins are three pins **4** placed equidistant from each other and also placed equidistant from said second opening **6**. The attachment means **9** is a rod attached to said sidewall **3**, such that said attachment means **9** extends from an outer surface of said sidewall **3**. The attachment means **9** is configured for providing electrical wiring to said pins **4**, and therefore there is a hole **11** going through the rod. The bottom inner surface **5** comprises an O-ring **12** to seal the second opening **6** with a test object, when a test object is placed on the O-ring. Wiring is able to be connected to the pins and into the hole **11** through the rod.

Fig. 2 shows an embodiment of the housing according to the present disclosure from below. **Figure 2** shows a housing **1** comprising a bottom surface **2** and a sidewall **3**; and a second opening **6** configured for passage of said liquid.

Fig. 3 shows an embodiment of the housing according to the present disclosure from above. **Figure 3** shows a housing **1** comprising a bottom surface **2** and a sidewall **3**; one or more electrically conductive pin(s) **4** positioned on a bottom surface **5** inside the housing **1**; a second opening **6** configured for passage of said liquid; and a first opening **7** configured for receiving said test object such that a front surface of the said object configured as working electrode can be placed in contact with said pin(s) and liquid. The bottom inner surface **5** comprises an O-ring **12** to seal the second opening **6** with a test object, when a test object is placed on the O-ring.

Fig. 4 shows an embodiment of the housing according to the present disclosure from the side. **Figure 4** shows a housing **1** comprising a bottom surface **2** and a sidewall **3**. The housing is configured for providing electrical wiring to said pins, and therefore there is a hole **10** going through the sidewall **3**.

Fig. 5 shows an embodiment of the housing according to the present disclosure from a perspective. **Figure 5** shows a housing **1** comprising a bottom surface **2** and a sidewall **3**; and a second opening **6** configured for passage of said liquid. The housing is configured for providing electrical wiring to said pins, and therefore there is a hole **10** going through the sidewall **3**.

Fig. 6 shows an embodiment of the housing according to the present disclosure from a perspective. **Figure 6** shows a housing **1** comprising a sidewall **3**; and a first opening **7** configured for receiving said test object such that a front surface of the object

configured as working electrode can be placed in contact with said pin(s) and liquid. The housing is configured for providing electrical wiring to said pins, and therefore there is a hole **10** going through the sidewall **3**.

Fig. 7 shows an embodiment of the attachment means **9** according to the present disclosure from the side. The attachment means **9** is a rod.

Fig. 8 shows an embodiment of the attachment means **9** according to the present disclosure from an end. The attachment means **9** is a rod. The attachment means **9** is configured for providing electrical wiring to said pins, and therefore there is a hole **11** going through the rod.

Fig. 9 shows an embodiment of the attachment means **9** according to the present disclosure from a perspective. The attachment means **9** is a rod. The attachment means **9** is configured for providing electrical wiring to said pins, and therefore there is a hole **11** going through the rod.

Fig. 10 shows an embodiment of the holding means according to the present disclosure from the side. The holding means **8** is for holding said test object in place between said pins and said holding means. The holding means **8** is a lid, configured to fit into the housing. There may be threading on the lid but this is not shown. In order to tighten the lid, there is a groove on the lid. Furthermore, the holding means may comprise one or more O-ring(s) but this is not shown.

Fig. 11 shows an embodiment of the holding means according to the present disclosure from the top. The holding means **8** is for holding said test object in place between said pins and said holding means. There may be threading on the lid but this is not shown. The holding means **8** is a lid, configured to fit into the housing. In order to tighten the lid, there is a groove on the lid. Furthermore, the holding means may comprise one or more O-ring(s) but this is not shown.

Fig. 12 shows an embodiment of the holding means according to the present disclosure from a perspective. The holding means **8** is for holding said test object in place between said pins and said holding means. There may be threading on the lid but this is not shown. The holding means **8** is a lid, configured to fit into the housing. In

order to tighten the lid, there is a groove on the lid. Furthermore, the holding means may comprise one or more O-ring(s) but this is not shown.

Fig. 13 shows an embodiment of the spacer according to the present disclosure. In this case, the spacer is placed inside the housing, for example such that a test object can be placed below the spacer, whereby the lid is able to press more on the test object, in comparison to if the spacer was not present.

Claims

1. A working electrode holder for measuring electrochemical properties of a front surface of a test object in a liquid, comprising:
   - a housing comprising a bottom surface and a sidewall, the sidewall defining a first opening such that the test object can be placed inside the housing via the first opening and such that the front surface is facing the inner bottom surface;
   - one or more electrically conductive pin(s) fixed to the bottom surface inside the housing such that the front surface of the test object is able to be placed on the pin(s), thereby providing an electrically contacted front surface, such that the electrically contacted front surface is able to operate as the working electrode; and
   - a second opening located in the bottom surface and configured for passage of said liquid, such that liquid is able to pass onto the electrically contacted front surface.

2. The working electrode holder according to claim 1, wherein said housing is configured for containing said test object comprising a circular surface with a diameter of at least 2.5cm, 5 cm, 7.5 cm, 10 cm, 12.5 cm or at least 15 cm in a plane parallel to said bottom surface inside the housing.

3. The working electrode holder according to any of the preceding claims, wherein said housing is configured for providing electrical wiring to said pins.

4. The working electrode holder according to any of the preceding claims, wherein said housing is configured for receiving holding means for holding said test object in place between said pins and said holding means.

5. The working electrode holder according to any of the preceding claims, wherein the cross section of said housing is circular, square, rectangular or triangular.

6. The working electrode holder according to any of the preceding claims, wherein said holding means is a lid.

7. The working electrode holder according to any of the preceding claims, wherein said housing and/or holding means are made of electrically insulating materials.

8. The working electrode holder according to any of the preceding claims, wherein said holding means comprises one or more O-ring(s).

9. The working electrode holder according to any of the preceding claims, wherein said holding means is configured to fit into the first opening, such that said liquid can only pass through the second opening.

10. The working electrode holder according to any of the preceding claims, wherein the height of said sidewall is at least 5mm, 10mm, 15mm, 20mm, 25mm, 30mm, 35mm, 40mm, 45mm, or at least 50mm.

11. The working electrode holder according to any of the preceding claims, wherein said pins are three pins placed equidistant from each other.

12. The working electrode holder according to any of the preceding claims, wherein said pins are three pins placed equidistant from said second opening.

13. The working electrode holder according to any of the preceding claims, wherein said test object is a composite of layers.

14. The working electrode holder, according to any of the preceding claims, wherein said housing further comprises attachment means for attaching said working electrode holder to an attachment holder.

15. The working electrode holder according to any of the preceding claims 14, wherein said attachment means is a rod attached to said sidewall, such that said attachment means extends from an outer surface of said sidewall.

16. The working electrode holder according to any of the preceding claims 14-15, wherein said attachment means is configured for providing electrical wiring to said pins.

17. The working electrode holder according to any of the preceding claims, wherein said housing or holding means or attachment means comprises one counter electrode.

18. The working electrode holder according to any of the preceding claims, wherein said housing or holding means or attachment means comprises one reference electrode.

19. The working electrode holder according to any of the preceding claims, wherein the second opening is positioned such that liquid can pass into a test area of the front surface of the test object.

20. The working electrode holder according to any of the preceding claims, wherein the second opening is in the centre of said bottom surface.

21. The working electrode holder according to any of the preceding claims, wherein the second opening is at an off-centre position.

22. The working electrode holder according to any of the preceding claims, wherein the second opening has an area of less than 10 cm^2, more preferably less than 8 cm^2, even more preferably less than 6 cm^2, yet more preferably less than 4 cm^2, most preferably less than 2 cm^2.

23. The working electrode holder according to any of the preceding claims, wherein the bottom surface inside the housing comprises an O-ring.

24. An electrochemical cell for measuring electrochemical properties of a test object, comprising
- a container containing a liquid, an electrode; and
- a working electrode holder according to any of the preceding claims in said liquid and with said test object in said holder.

25. The electrochemical cell according to claim 24, wherein said electrode is a counter electrode and/or a reference electrode attached to said working electrode holder.

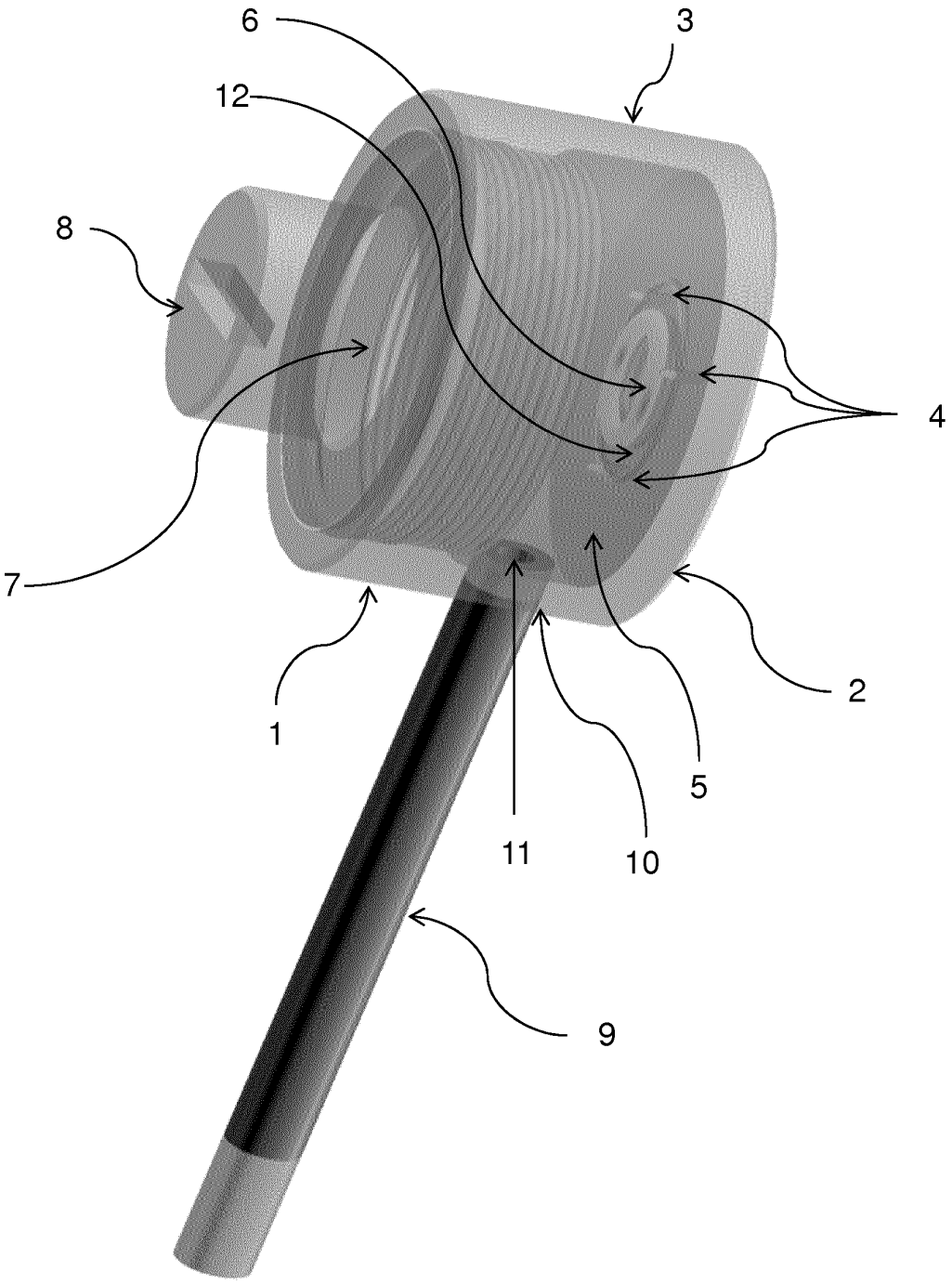

Fig. 1

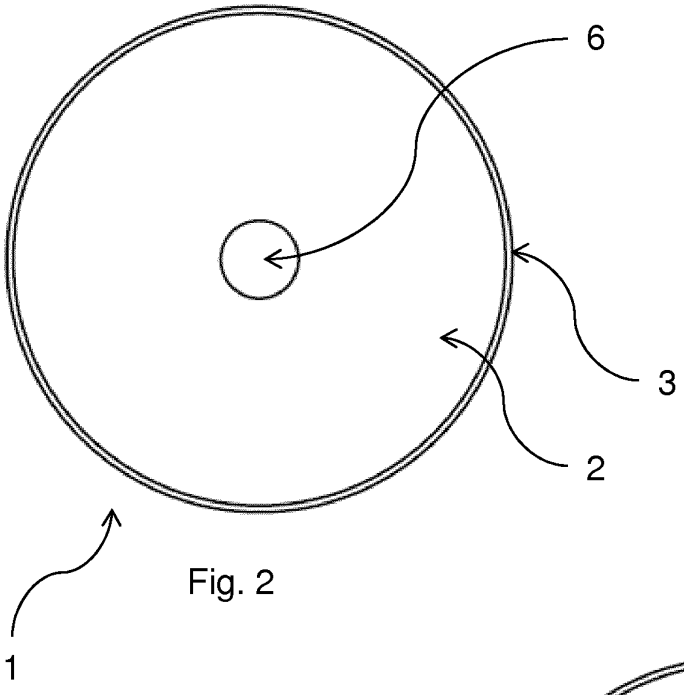

Fig. 2

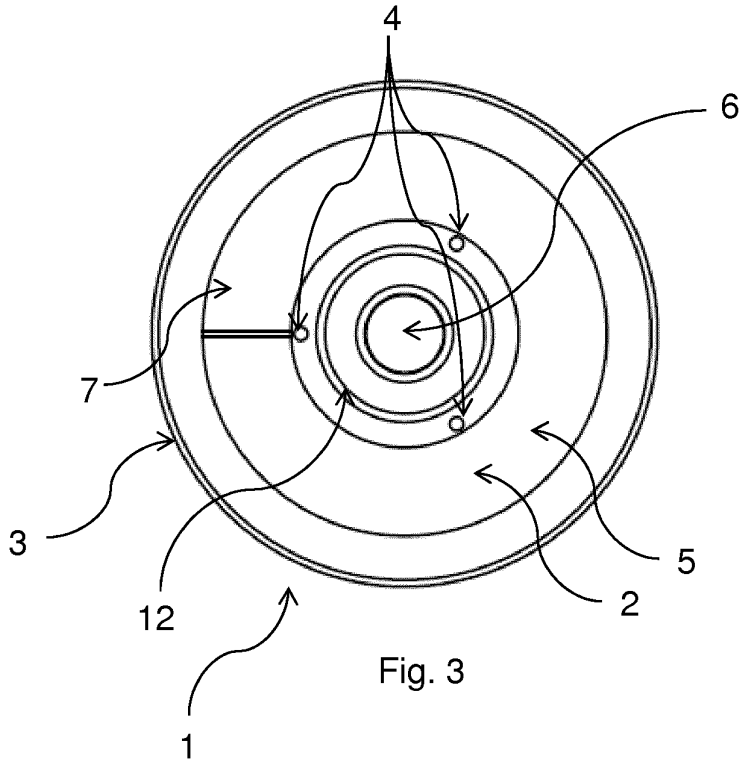

Fig. 3

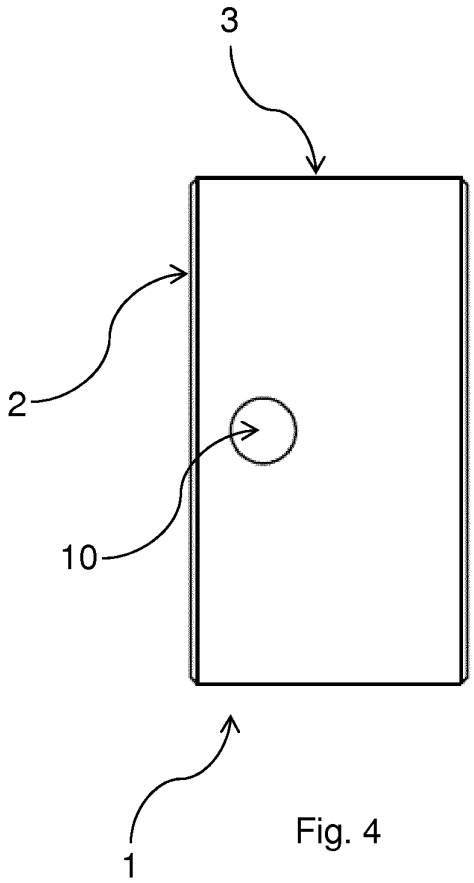

Fig. 4

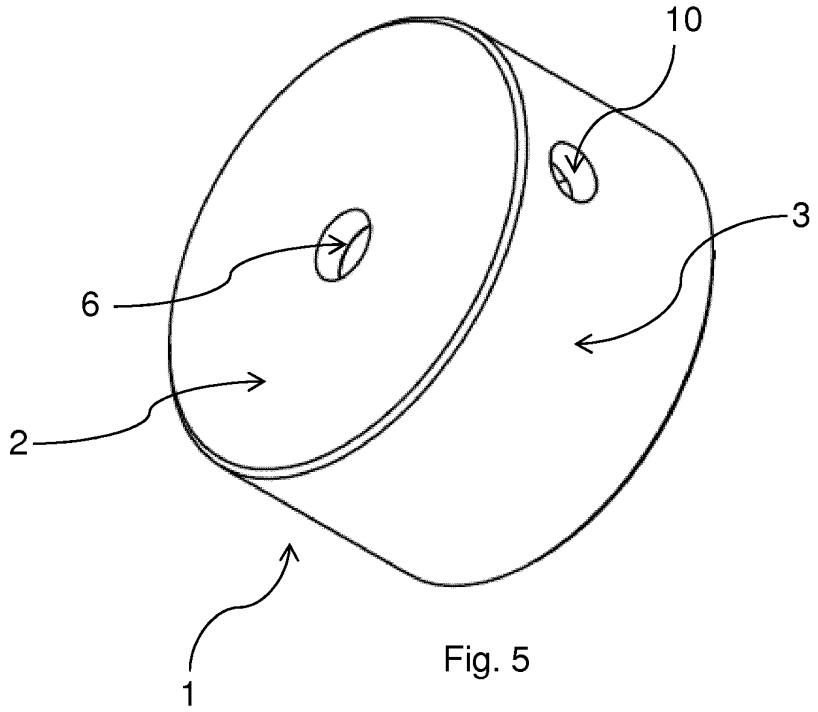

Fig. 5

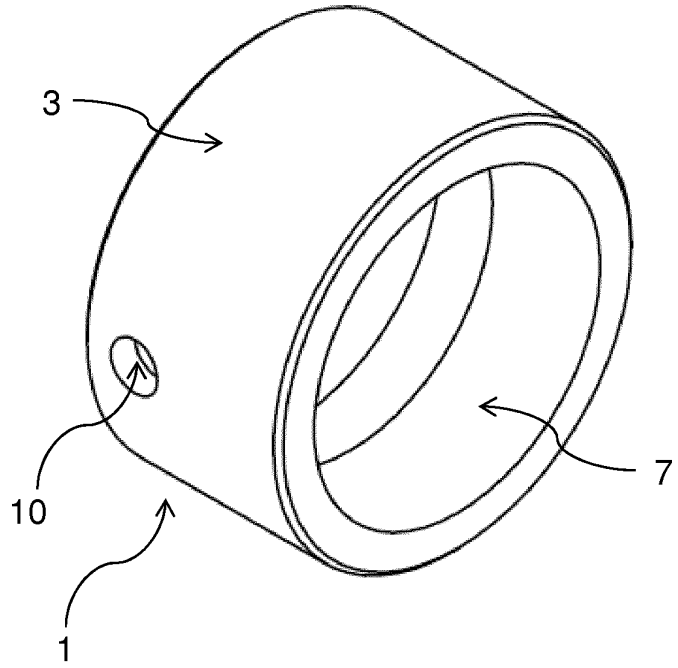

Fig. 6

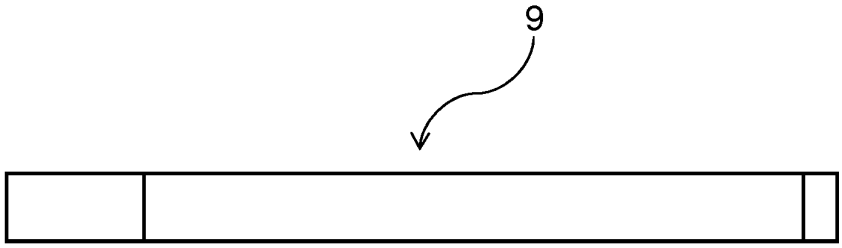

Fig. 7

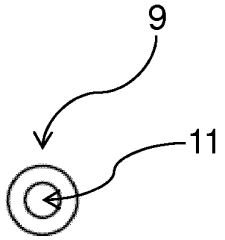

Fig. 8

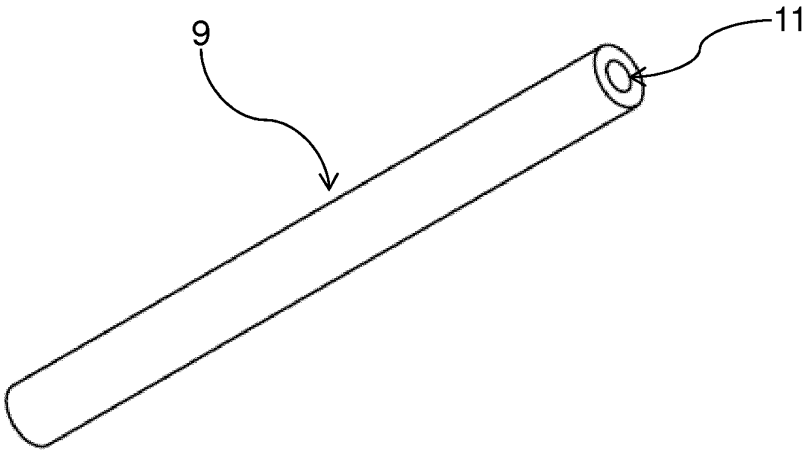

Fig. 9

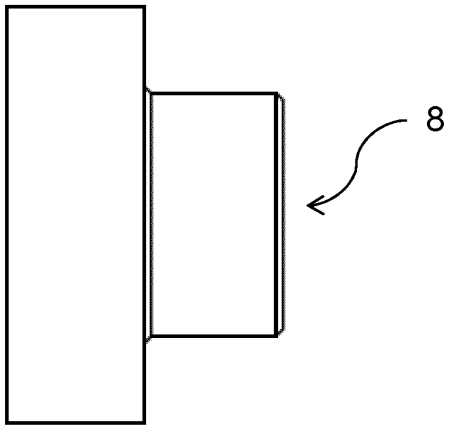

Fig. 10

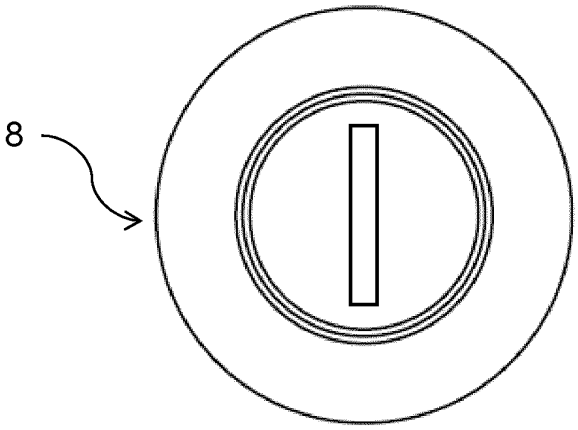

Fig. 11

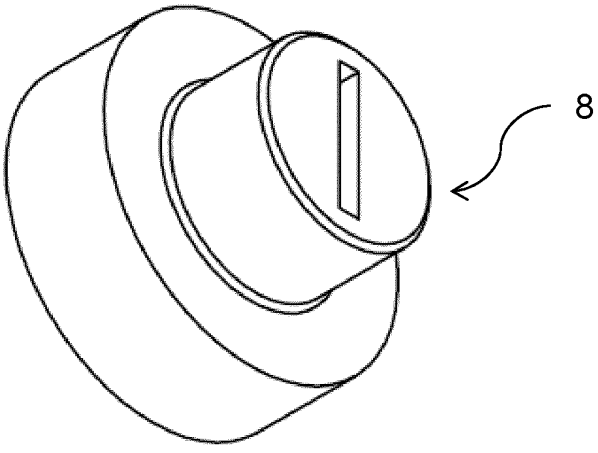

Fig. 12

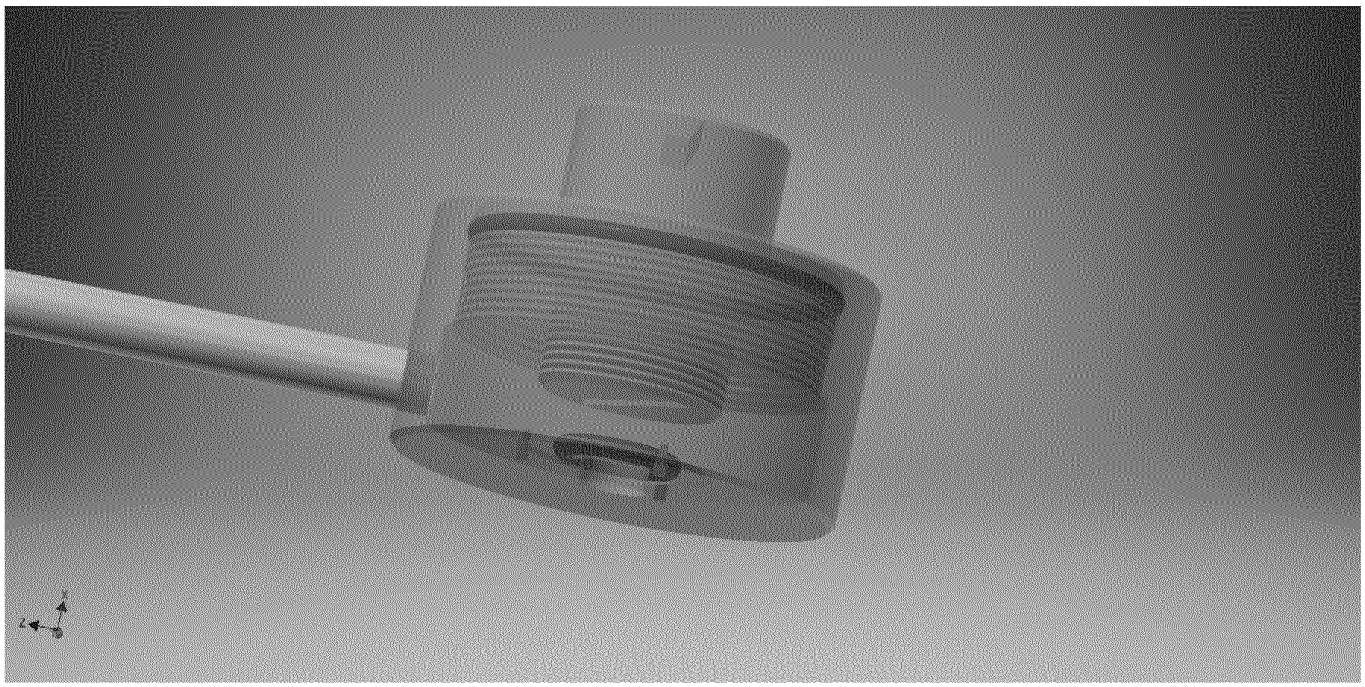

Fig. 13

INTERNATIONAL SEARCH REPORT

International application No
PCT/EP2015/067215

A. CLASSIFICATION OF SUBJECT MATTER
INV. G01N27/28 G01N17/02
ADD.

According to International Patent Classification (IPC) or to both national classification and IPC

B. FIELDS SEARCHED

Minimum documentation searched (classification system followed by classification symbols)
G01N

Documentation searched other than minimum documentation to the extent that such documents are included in the fields searched

Electronic data base consulted during the international search (name of data base and, where practicable, search terms used)
EPO-Internal, WPI Data

C. DOCUMENTS CONSIDERED TO BE RELEVANT

Category*	Citation of document, with indication, where appropriate, of the relevant passages	Relevant to claim No.
A	WO 2014/008942 A1 (LONZA AG [CH]) 16 January 2014 (2014-01-16) figures 1-3 page 1, line 5 - line 25 page 10, line 5 - line 6 page 11, line 15 - line 29 page 13, line 4 page 14, line 2 - line 33 -----	1-25
A	GB 2 168 161 A (GRUZINSK POLT INST) 11 June 1986 (1986-06-11) figures 1,2 page 2, left-hand column, line 40 - right-hand column, line 121 ----- -/--	1-25

[X] Further documents are listed in the continuation of Box C.

[X] See patent family annex.

* Special categories of cited documents :

"A" document defining the general state of the art which is not considered to be of particular relevance

"E" earlier application or patent but published on or after the international filing date

"L" document which may throw doubts on priority claim(s) or which is cited to establish the publication date of another citation or other special reason (as specified)

"O" document referring to an oral disclosure, use, exhibition or other means

"P" document published prior to the international filing date but later than the priority date claimed

"T" later document published after the international filing date or priority date and not in conflict with the application but cited to understand the principle or theory underlying the invention

"X" document of particular relevance; the claimed invention cannot be considered novel or cannot be considered to involve an inventive step when the document is taken alone

"Y" document of particular relevance; the claimed invention cannot be considered to involve an inventive step when the document is combined with one or more other such documents, such combination being obvious to a person skilled in the art

"&" document member of the same patent family

Date of the actual completion of the international search	Date of mailing of the international search report
11 November 2015	26/11/2015

Name and mailing address of the ISA/	Authorized officer
European Patent Office, P.B. 5818 Patentlaan 2 NL - 2280 HV Rijswijk Tel. (+31-70) 340-2040, Fax: (+31-70) 340-3016	Gangl, Martin

1

Form PCT/ISA/210 (second sheet) (April 2005)

C(Continuation). DOCUMENTS CONSIDERED TO BE RELEVANT

Category*	Citation of document, with indication, where appropriate, of the relevant passages	Relevant to claim No.
A	"Model K0047 Corrosion Cell System - Instruction Manual", , 1 January 2005 (2005-01-01), pages 1-11, XP055161514, Retrieved from the Internet: URL:http://www.princetonappliedresearch.com/download/K0047-Corrosion-Cell-Kit-CN.pdf [retrieved on 2015-01-12] page 1 - page 4; figures 1-3	1-25
A	CN 103 293 093 A (UNIV HARBIN ENG) 11 September 2013 (2013-09-11) abstract; figures 1,2 paragraphs [0025], [0026]	1-25

1

INTERNATIONAL SEARCH REPORT

Information on patent family members

International application No
PCT/EP2015/067215

Patent document cited in search report	Publication date	Patent family member(s)	Publication date
WO 2014008942 A1	16-01-2014	NONE	
GB 2168161 A	11-06-1986	BG 46704 A1	15-02-1990
		DD 272020 A3	27-09-1989
		DE 3535519 A1	19-06-1986
		GB 2168161 A	11-06-1986
		JP S61181952 A	14-08-1986
		SU 1404901 A1	23-06-1988
		US 4695360 A	22-09-1987
CN 103293093 A	11-09-2013	NONE	

Appendix D

Gamry Flat Specimen Holder

Redefining Electrochemical Measurement

Flat Specimen Holder

Holder Description

The Flat Specimen Holder (part number 990-00403) has been designed to hold flat, circular or square samples for use in the Multiport Corrosion Cell. This optional holder is designed to handle circular samples from 25 to 30 mm in diameter or square samples with sides length up to 23 mm. The actual exposed electrode face is 10 mm in diameter with an area of 0.785 cm^2. Samples can be up to 7 mm thick.

Made from tough, durable PEEK, the holder can withstand temperatures up to 80 C. Contact is made on the front of the sample through the use of Pogo pins.

Flat Specimen Holder in the Multiport Corrosion Cell.

*Patent Pending - WO 2016/016214 A1.

734 Louis Drive Warminster, PA 18974 +215-682-9330 sales@gamry.com www.gamry.com

Published by:
DTU Nanotech
Department of Micro- and Nanotechnology
Technical University of Denmark
Ørsteds Plads, building 345C
DK-2800 Kgs. Lyngby